Università Politecnica delle Marche
Scuola di Dottorato di Ricerca in Scienze dell'Ingegneria
Curriculum in Ingegneria Industriale

Soft sensing in the process industry

Ph.D. Dissertation of:

Edoardo Copertaro

Advisor:

Prof. Gian Marco Revel

Curriculum supervisor:

Prof. Nicola Paone

XIV edition - new series

Abstract

Present contribution discusses the application of soft sensing in the process industry, as an indirect monitoring technique for the on-line assessment of non-accessible process variables. A relevant application case is presented which involves clinker sintering, a low-efficient, high-energy intensive process with strong environmental impact: the soft-sensing approach is firstly tested in the conventional thermal system, then it is addressed an innovative heating module based on the application of high-power, mono-modal microwaves to the material under processing.

The work is focused over the development of physical models for the indirect evaluation of the critical process variables. The integration of the computation routines with the data provided by the sensors of the monitoring architectures is also addressed, as well as possible optimization strategies for improving the reliability of the tools.

A stochastic method based on an adaptive Monte Carlo procedure is implemented, for assessing the propagation of the input uncertainties through the mathematical model of the soft sensor. An innovative numerical framework provides a lower-bound estimation of the uncertainty introduced by the model itself. Successively, the overall uncertainty of the soft sensor is calculated as the composition of the different contributes.

The soft sensors are tested in the real-time monitoring of thermal and chemical variables of the processes considered. The indirect estimations of the target variables are compared with direct measurements, showing deviations in the order of 1%. Computation routines ensure fast executions, thus improving the exploitability of the tools. Results confirm the good performances of the soft sensors in the on-line monitoring of non-accessible variables. The intrinsic robustness makes them a potential back-up of direct sensors, ready to intervene when a breakdown of the hardware counterpart occurs, and before this affects the process.

Contents

List of Figures

List of Tables

Introduction

In the process industry disposing of accurate measurements of critical variables at the appropriate sampling frequency is fundamental in order to take proper control actions. On this regard, hardware devices may not satisfy fundamental requirements, mainly in terms of reliability and performances. In either case on-line control and optimization schemes cannot be implemented.

Recently, new indirect measurement approaches based on soft sensing have gained relevance in the field of process monitoring, whereas technical or economic aspects make hardware devices unsuitable. In this sense, disposing of theoretical models based on the phenomenological knowledge of the process and/or on regression analyses of the historical data, allows the full exploitation of a large number of values measured continuously as they may represent input signals for the soft sensor. At the same time, soft sensing opens the way to a wide range of applications, among which on-line monitoring, process fault detection, identification of broken sensors and back up of the hardware equipment.

Present contribution discusses the general application of soft sensing in the process industry. An application case is presented, regarding the clinker production process. Indeed, this process is deeply affected by a dramatic lack of direct measurements on critical variables, as a consequence of technical difficulties (aggressive environment, physical inaccessibility, moving parts, etc.). Lack of measurements prevents the achievement of a full understanding of the process thus resulting in non-optimized operation. Soft sensing could represent a valuable tool for filling this gap of knowledge and producing new efficiency-oriented control strategies, which is an actual issue for whole the global cement industry.

The manuscript is organized as follows:

I.   Section 1 introduces the topic of soft sensing. In subsection 1.1 a literature survey is reported, concerning the application of indirect measurement techniques to the monitoring of industrial processes: the development approach of a soft sensor is discussed; potentialities and weaknesses are identified; further, a wide range of applications is reported. Subsection 1.2 describes the concept of soft sensor, and provides deep focus on both its metrological and theoretical aspects. Subsection 1.3 points out the differences between a soft sensor and the hardware counterpart; it deals with the distinction between the theoretical model supporting a soft sensor and the transduction function of a measurement device. Subsection 1.4 is concerned over possible methods for esteeming the uncertainty of a soft sensor, which is a topic not faced yet.

II.   Section 2 introduces the clinker production process. Particular focus is dedicated to the kiln system, a high-energy intensive, low-efficient sintering stage with strong environmental impact. Subsection 2.1 deals with the conventional thermal process, whilst subsection 2.2 is focused over an innovative heating cavity developed in the EU FP7 project DAPhNE (grant agreement n° 314636), which is based on microwaves application.

III.   In section 3 soft sensing is applied to the conventional heating stage. The indirect estimation of critical process variables, otherwise not directly accessible, is found

to be in good agreement with real data; besides, it represent valuable information to be used in the development of new optimization-oriented control strategies.

IV. In section 4 the accuracy of the soft sensor is esteemed by studying the propagation of the input uncertainties through the mathematical model; further, an innovative modellistic framework is used for quantifying the approximation introduced by the simplifying assumptions of the theoretical part.

V. In section 5 an analogous monitoring approach is proposed for the new DAPhNE module. The possibility for intervening in the design of the whole monitoring architecture has been fully exploited for integrating the new tool with the rest of the hardware devices.

Section 1 – Soft sensing

1.1 – Literature survey

In the last two decades, soft sensors have established themselves as a valid alternative to traditional approaches for monitoring critical process variables, whereas technical or economic aspects make direct measurements unfeasible. According to Kadlec [1], "industrial processing plants are usually heavily instrumented with a large number of sensors. The primary purpose of the sensors is to deliver data for process monitoring and control. But approximately two decades ago researchers started to make use of the large amounts of data being measured and stored in the process industry, by building predictive models based on this data. In the context of process industry, these predictive models are called "*soft sensors*". This term is a combination of the words "*software*", because the models are usually computer programs, and "*sensors*", because the models are delivering similar information as their hardware counterparts".

According to Mohler [2], "control systems and optimization procedures require regular and reliable measurements at the appropriate frequency […]. The quality measure may only be available as a laboratory analysis or very infrequent on-line measurement". Lack of appropriate on-line instrumentation and unreliability of on-line instruments are mentioned as possible causes which may prevent the achievement of good measurements. In either case on-line control or optimization schemes cannot be implemented. As stated in [2], "the application of soft sensors for estimating hard-to-measure process values is extremely interesting in the process industry, where there are usually a large number of values measured continuously and they may serve as input signals for the soft sensor. They can work in parallel with real sensors, allowing fault detection schemes devote to the sensor's status analysis to be implemented. Also, they can take the place of sensors which have been taken off for maintenance, to keep control loops working properly and to guarantee product specification without undertaking conservative production policies, which are usually too expensive". In its literature survey, Kadlec [1] identifies a broad range of tasks were a soft sensor could be effectively exploited. In this sense, "the original and still most dominant application area of soft sensors is the prediction of process variables which can be determined either at low sampling rates or through off-line analysis only. Because these variables are often related to the process output quality, they are very important for the process control and management. For these reasons it is of great interest to deliver additional information about these variables at higher sampling rate and/or at lower financial burden, which is exactly the role of the soft sensors […]. Other important application field of soft sensors is fault detection […]"; on this regard "once a fault sensor is detected and identified, it can be either reconstructed or the hardware sensor can be replaced by another soft sensor, which is trained to act as a back-up soft sensor of the hardware measuring device. If the back-up sensor proves to be an adequate replacement of the physical sensor, this idea can be driven even further and the soft sensor can replace the measuring device also in normal working conditions. The software tool can be easier maintained and is not subject to mechanical failures and therefore such a substitution can provide a financial advantage for the process owner".

Kadlec [1] distinguishes two types of soft sensors, "namely "*model-driven*" and "*data-driven*" soft sensors. Firsts are also called white-box models because they have full phenomenological knowledge about the process background. In contrast to this purely data-driven models are called black-box techniques because the model itself has no knowledge about the process and is based on empirical observations of the process […]. Model-driven soft sensors are primarily developed for the purpose of planning and development of the process plants. These soft sensors are based on equations describing the chemical and physical principles underlying the process. A typical example is using mass-preservation principles, exothermal equation, energy balances, reaction kinetics in the form of reaction rate equations for this purpose. The drawback of this type of soft sensors is that their development requires a lot of process expert knowledge. This knowledge is not always available […]. Another problem is that the models often describe a simplified theoretical background of the process rather then the real-life conditions of the process which is influenced by many factors out of the scope of the model-driven soft sensor. Additionally, the model-driven soft sensors usually focus on the description of the optimal steady-state of the process and are thus not suitable for the description of any transient states […]". On the other hand, "data-driven models are based on the data measured within the processing plants […]. The most popular modelling techniques applied to data-driven soft sensors are the Principal Component Analysis, Partial Least Squares, Artificial Neural Networks, Neuro-Fuzzy Systems and Support Vector Machines".

1.1.1 – Data-driven soft sensors

Linear Regression models have been applied in a wide range of cases: here they provide a straightforward modeling of the target values, which are expressed as linear combinations of the input variables. Casali et al. [3] propose an ARMAX-type stepwise regression model for modeling the particle size in a grinding plant. Park [4] applies a Locally Weighted Regression together with non-linearity handling pre-processing of the input data; the model is applied to two industrial cases (toluene composition in a splitter column and diesel temperature estimation in a crude oil column).

Artificial Neural Networks (ANNs) are widely exploited in the field of machine learning. In the context of soft sensors development, Qin [5] applies Multilayer Perceptron (MLP) to the description of a batch refinery process. Radhakrishnan [6] provides an extensive discussion of application aspects of MLP to steel industry data modelling, for prediction of hot metal quality. MLP is applied in [7] and [8], respectively for esteeming sugar quality and predicting butane and stabilized gasoline concentrations of a distillation column. In [9] MLP is applied to the detection of typical faults in a fluid catalytic cracking reactor. In [10] an approach for soft sensor development based on MLP is applied to an industrial drier process. In [11] the performances of two ANN variants, namely the MLP and the Radical Basis Function Network (RBFN), are compared to a Support Vector Regression model, in the context of fed-batch bioreactors. A RBFN-based soft sensor is tested in [12], for modeling a membrane separation process. Recurrent Neural Network (RNN) is applied in [13], [14] and [15], respectively for predicting the degree-of-cure in an epoxy/graphite fiber composites production process, the biomass concentration in bioprocesses and the melt-flow length for

4

filling of molds in a injection molding process. Application of RNN in a dynamic environment is reported in [16].

A further method commonly applied to soft sensing is Principal Component Analysis (PCA)/Partial Least Squares (PLS)-based regression. In [17] a PCA-based preprocessing of input data removes co-linearity and allows the possibility of reconstructing sensor fault. The soft sensor is tested in the monitoring of air emission. A recursive version of the PLS algorithm (namely Exponentially Weighted PLS) is applied in [18] to the simulation of a continuous stirred tank reactor and a industrial flotation circuit. An application of PLS to the prediction of the octane number in a refinery process is discussed in [19]. Zamprogna et al. [20] are dealing with application aspects of the PCA and PLS to the modelling of batch processes. A PCA-based soft sensor for predicting concentrations of free lime and NO_X in a cement kiln is presented in [21]. In [22], [23], [24] and [25] PCA and PLS-based techniques are tested in the monitoring of batch and semi-batch processes. Li et al. [26] deal with the application of the PCA and related methods to the monitoring of a rapid thermal annealing process. A multi-step Fisher Discriminant Analysis-based approach for detecting process fault is reported in [27]. In [28] a complex soft sensor for the detection and isolation of process faults is devised which is based on PCA, RBFN and Self Organizing Map. Applications of PCA in sensor fault detection and reconstruction are reported in [29], [30], [31] and [32].

Support Vector Machines (SVM) are emerging in the field of machine learning. Yan et al. [33] apply SVR to the estimation of the freezing point of light diesel oil in a fluid catalytic cracking unit. A further application of SVM for developing soft sensors dedicated to the monitoring of industrial processes is discussed in [34].

Another very popular and successful family of approaches applied to soft sensing are neuro-fuzzy models (ANFIS) which combine the advantages of ANNs and Fuzzy Inference Systems (FIS). In [35] Merikoski implements a soft sensor based on an ANFIS model for predicting rubber viscosity. Another ANFIS-based soft sensor is presented in [36]: here data is preprocessed using PCA transformation which helps dealing with co-linearity and at the same time limits the size of the input space; the soft sensor is applied to the prediction of polymeric-coated substrate anchorage which is an important quality measure of the process product. In [37] and [38] the performances of a neuro-fuzzy soft sensor are tested, respectively, in the prediction of the freezing point of light diesel fuel in a fluid catalytic cracking unit and in the control of a penicillin production batch process. In [39] an extended Takagi-Sugeno model is tested in the prediction of the quality of crude oil distillation in a refinery process.

1.1.2 – Model-driven soft sensors

Model-driven soft sensors are widely spread in the context of process fault detection. According to [40], "fault detection problems require two steps. The first step generates inconsistencies between the actual and expected behavior. Such inconsistencies, also called "*residuals*", are artificial signals reflecting the potential faults of the system. The second step chooses a decision rule for diagnosis. The check for inconsistency needs some form of redundancy. There are two types of redundancies, hardware redundancy and analytical redundancy. The former requires redundant sensors […]. However, its applicability is limited

5

due to the extra cost and additional space required. On the other hand, analytical redundancy is achieved from the functional dependence among the process variables and is usually provided by a set of algebraic or temporal relationships among the states, inputs and the outputs of the system". These relationships are obtained based on a physical understanding of the process. In a chemical engineering process, mass, energy and momentum balances as well as constitutive relationships (such as equations of state) are used in the development of model equations. Comprehensive discussions on both artificial redundancy and discrimination methods applied to fault detection can be found in [41][42][43][44][45].

In the context of process monitoring, hybrid models are significantly widespread: in these models the greater accuracy of a data-driven soft sensor can be effectively exploited in conjunction with the typical robustness of a model-driven one. In [46] an MLP is compared to model-driven approaches based on an adaptive observer technique and Kalman filter, on a test case involving the estimation of fermentation batch processes; whilst complexity of the development and the amount of a priori knowledge are recognized as limiting factors of the model-based approach, on the other hand the applicability of the MLP is limited due to the changing dynamics of the particular batch runs. In [47] a test case involving a biochemical batch process is used for comparing a model-driven soft sensor with either an MLP or an RBFN. Meleiro et al. [48] are presenting a grey-box soft sensor which delivers necessary information for self-tuning an adaptive controller of a fermentation process. The soft sensor is an MLP which is trained using simulated data based on a phenomenological model.

1.2 – The concept of soft sensing

Next part of this contribution will be focused on model-driven soft sensors; these will be simply addressed as soft sensors.

A soft sensor is the synthesis of two different parts, which are complementary, namely: a) the metrological one, which includes the direct monitoring of accessible variables by using dedicated hardware sensors; b) the theoretical one, which consists of a deterministic model providing a correlation between the target variable and the measurements available at plant level. This model will be addressed as "*correlating model*".

When developing a soft sensor these two parts should be considered as strictly correlated, even if they may seem separate each from other. in fact, the more the measurements are "close" to the target variable, the easier it will be developing an accurate correlating model. The simple case reported in Figure 1 can be considered an example of a soft sensor development. Here the target variable is the temperature T_1 of the bottom surface s_1: if the only measurements available consist of T_3 and Q_3, respectively the temperature and the heat flux through the top surface s_3, then the model should account for the heat conduction through t_1 and t_3 and the convective and radiative heat exchanges through t_2; on the other hand, if direct measurements T_2 and Q_2 (respectively the temperature and the heat flux through the surface s_2) are made available, then only the heat conduction through t_1 should be considered. As pointed out in the previous example, direct measurements could be effectively exploited for providing boundaries to the correlating model, thus reducing its complexity and at the same time increasing the accuracy. Anyhow it should be considered that an excessively-pushed metrological part may compromise the potential benefits of soft sensing, in terms of cost and reliability.

If a soft sensor is intended to provide an alternative to the counterpart hardware sensors, its capability of self-interfacing to the rest of the monitoring architecture should be assessed. This aspect is particularly critical when the soft sensor is specifically developed for overcoming the bottleneck represented by a long response time of the hardware equipment (e.g. a chemistry analyzer). The response time of a soft sensor is determined by the model, in particular its computation routine. In this sense extremely complex and omni-comprehensive models may be effective in providing reliable and detailed outputs, but they are generally relegated to the role of stand alone tools. On the other hand, disposing of simplified but still accurate models opens the way to a wide range of on-line applications.
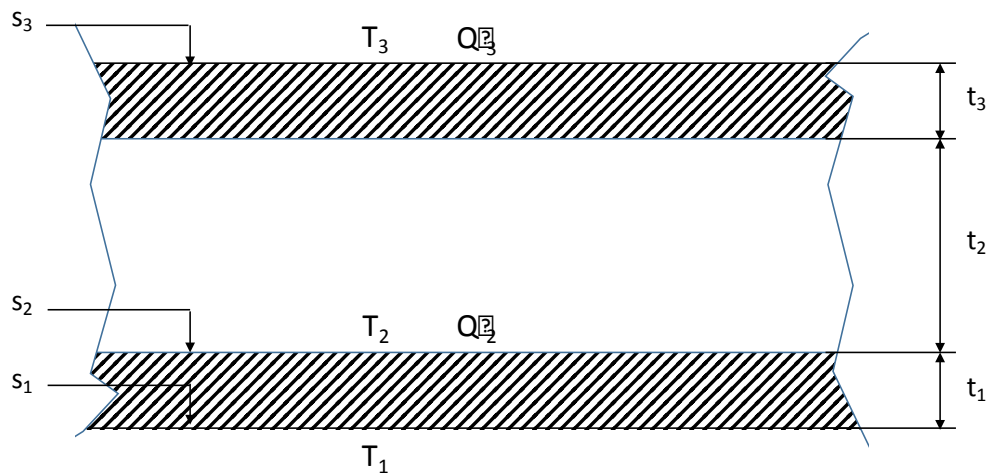
Figure 1. The concept of soft sensing.

1.3 – Soft sensors vs. hardware sensors

Even if the difference between soft and hardware sensors may seem evident, actually it is less obvious then it could be imagined. This is due the frequent difficulty of providing a clear and objective distinction between the transduction function of a sensor and the correlating model used in soft sensing. Indeed, in both cases we are dealing with functions which are responsible for converting inputs into output data.

Currently, a generally accepted definition which objectifies the difference does not exist. It might be thought the specific feature of a transduction function is that it is based on a physical law. As a few examples: eq. 1 reports the Seeback effect, which is used in thermocouples, and relates the output voltage V to the difference of temperature of the hot junction respect to the cold one (S denotes the calibration factor); eq. 2 shows the Stefan-Boltzmann law for infrared measurement devices, where the radiation intensity P is expressed as a function of the temperature T (A, σ and ε denote respectively the area of the surface, the Stefan-Boltzmann constant and the emissivity); the transduction function of a heat flux meter is reported in eq. 3, where the output voltage V is related to the het flux Q through an intrinsic feature of the instrument K_{sesn}.

$$V = S \cdot \nabla T \tag{1}$$

$$P = A \cdot \varepsilon \cdot \sigma \cdot T^4 \tag{2}$$

$$V = Q \cdot K_{sens} \tag{3}$$

This definition stands when the correlating model is a data-driven one; but it fails when referring to deterministic models, which are based on physical laws themselves. On this regard, we can refer to the example reported in Figure 1: here the correlating function expressing T_1 as a function of T_2 and Q_2 is the one reported in eq. 4.

$$T_1 = T_2 + Q_2 \cdot \frac{t_1}{K_{wall}} \tag{4}$$

The expression represents a physical law, besides it requires the calibration of the K_{wall} parameter, same as it happens with the K_{sens} parameter for the heat flux meter. Differences between a correlating model and a transduction function are pointed out hereafter:

I. In the transduction function the output is directly related to the input. This may be untrue in the case of a correlating model, whose output could be a physical quantity that is completely different respect to the inputs. As an example, in [49] it is developed a soft sensor for predicting the fuel consumption and the exhaust emissions of a diesel engine, using real time values of: intake manifold air temperature; intake manifold boost pressure; fuel rack position; engine coolant temperature; exhaust gas temperature; engine speed; fuel rail temperature and pressure.

II. The transduction function acts upstream the digitalization. The correlating function gets digital inputs, and elaborates them on the basis of calculation routines which are external to the instrument.

III. A correlating model may receive more inputs and elaborates them into one or more outputs. A transduction function converts one input into one output.

IV. A correlating function may not be based on a physical law, instead it could be developed on the basis of fuzzy or regression approaches, artificial neural networks, etc.

The previous points should clarify the difference between a transduction function and a correlating model. Nevertheless, it may be useful to consider the correlating function as an integrating part of the transduction chain. So it is possible to easily extend some relevant features of a measurement device also to soft sensors. In section 1.4. some considerations will be pointed out regarding the uncertainty of a soft sensor.

1.4. – Estimation of the uncertainty of a soft sensor

Estimation of the uncertainty of a soft sensor is a topic which has not been faced yet. Nevertheless, when soft sensing is applied to the monitoring of process variables, a quantification of the accuracy is fundamental. In the next part of this section a method for assessing the uncertainty of a soft sensor is discussed.

The method considers the correlating model as an integrating part of the transduction chain, thus it influences the overall uncertainty of the soft sensor. For sake of clarity, it can be considered the example depicted in Figure 2. Here the correlating model receives n measurements $i_1 \dots i_n$ in input, which are characterized by the respective uncertainties $u_{i1} \dots u_{in}$; at the same way the model accounts for m parameters $p_1 \dots p_m$, characterized by the uncertainties $u_{p1} \dots u_{pm}$, respectively; Y denotes the output of the model and it is affected by the uncertainty u_y, which is the sum of two contributes:

1. Propagation of the input uncertainties $u_{i1} \dots u_{in}$ and $u_{p1} \dots u_{pm}$ through the correlating model. This contribution is discussed in subsection 1.4.1.
2. The uncertainty introduced by the simplifying assumptions of the mathematical model. Subsection 1.4.2. deals with this part.

These two contributes can be combined, in order to obtain the overall uncertainty of the soft sensor.
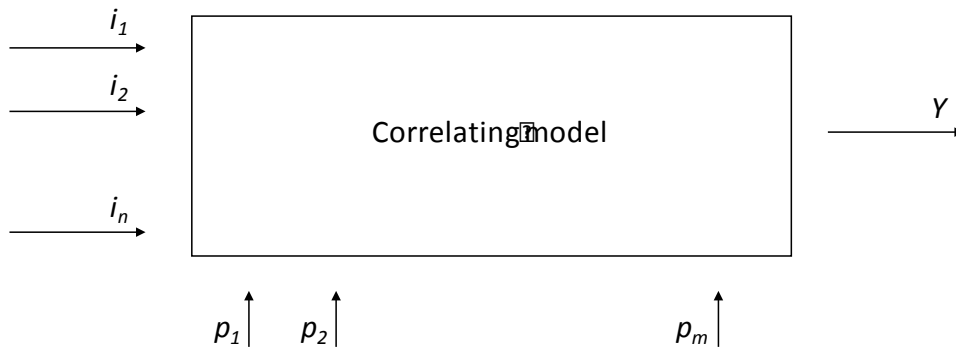
Figure 2. Input uncertainties of the correlating model.

1.4.1 – Propagation of input uncertainties through the correlating model

Propagation of the uncertainties through the mathematical model can be esteemed according to the recommendations of the Guide to the expression of uncertainty in measurement (GUM) [53]. In particular, the Supplement 1 to the GUM "is concerned with the propagation of probability distributions through a mathematical model of measurement as basis for the evaluation of uncertainty of measurement, and its implementation by a Monte Carlo method […]. The described Monte Carlo method is a practical alternative to the GUM uncertainty framework. It has value when: a) linearization of the model provides an inadequate representation; b) the probability density function (PDF) for the output quantity and the

9

associated standard uncertainty provided by the GUM uncertainty framework might be unreliable […]. This Supplement provides a general numerical approach, consistent with the broad principles of the GUM for carrying out the calculations required as part of an evaluation of measurement uncertainty. The approach applies to arbitrary models having a single output quantity where the input quantities are characterized by any specified PDFs […]. This Supplement can be used to provide the PDF for the output quantity from which a) an estimate of the output quantity, b) the standard uncertainty associated with the estimate, c) a coverage interval for that quantity, corresponding to a specified coverage probability can be obtained". Guidelines for the implementation of an adaptive Monte Carlo procedure are provided, "which involves carrying out an increasing number of Monte Carlo trials until the various results of interest have stabilized in a statistical sense. A numerical result is deemed to have stabilized if twice the standard deviation associated with it is less than the numerical tolerance associated with the standard uncertainty". The adaptive Monte Carlo procedure is reported in Appendix A.1.

1.4.2 – Uncertainty introduced by the correlating model

Soft sensors are generally based on simplified models. Typically, these are lumped element models which are able to provide a quite accurate representation of the system, but at the same time ensure short computation times. An estimation of the uncertainty introduced by the different simplifying assumptions is fundamental for quantifying the overall accuracy of the soft sensor.

In a lumped element model, variables that are spatially distributed are approximated using discrete elements. In the example of Figure 3a an envelope A contains two different phases B and C, whereof B is heated by an electric resistance R providing the total heating power Q_R. The system can be well described by using three lumped elements, connected each other by thermal resistances (see Figure 3b). It is evident that in the lumped model the spatial variance of T is completely lost, thus it introduces an uncertainty of representation. The lower-bound of this uncertainty can be esteemed via an off-line comparison with a spatially-distributed model, to be used as reference (the method does not account for the uncertainty of the reference model).

a)

b)
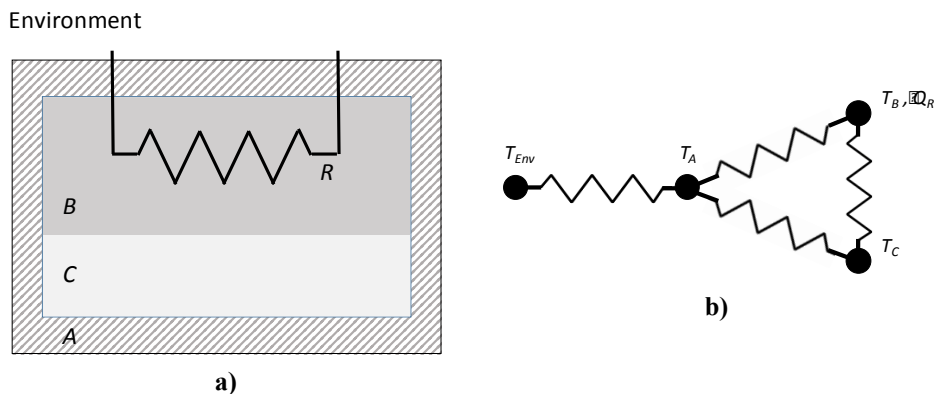
Figure 3. Distributed vs. lumped element model.

10

Section 2 – Clinker production process

Cement constitutes basic material for building and civil engineering applications. Portland is the most common type of cement, and it is obtained by grinding a mixture of gypsum and clinker. Clinker is composed by lumps or nodules, usually 3-25 mm in diameter, 3.1 g/cm^3 mass density, produced by sintering limestone and clay during the cement kiln stage. The composition of the final clinker is the product of several chemical reactions involving the starting materials (raw meal), and occurring in a wide range of temperatures. Main reactions involved in clinker sintering are reported hereafter. Table 1 indicates the typical composition of final clinker, data from [54].

$$2CaO + SiO_2 \rightarrow C2S \text{ (Belite)} \tag{5}$$

$$3CaO + Al_2O_3 \rightarrow C3A \text{ (Aluminate)} \tag{6}$$

$$4CaO + Al_2O_3 + Fe_2O_3 \rightarrow C4AF$$
(Ferrite) $$\tag{7}$$

$$CaO + C2S \rightarrow C3S \text{ (Alite)} \tag{8}$$

In order to regulate the hydration process, a quantity (typically 5 %) of calcium sulfate (usually gypsum or anhydrite) is added to clinker, and the mixture is finely ground to form the final cement powder. This is achieved in a cement mill. The grinding process is controlled to obtain a powder with a broad particle size range, in which typically 15 % by mass consists of particles below 5 μm diameter, and 5 % of particles above 45 μm. Portland cement cab be marketed as pure, otherwise it can be mixed with other constituents expected by technical standards. Mixing is performed during cement milling, adding the other constituents to clinker and gypsum.

Phase	Mass fraction (%)
C3S	58.6 ± 4.0
C2S	23.3 ± 2.8
C4AF	14.1 ± 1.4
C3A	2.3 ± 2.1

Table 1. Chemical composition of clinker.

Global production of Portland cement is continuously increasing, despite a general slowing of the advanced economies: forecasts by the Portland Cement Association for US cement consumption [55] indicate expectations for a 7.5 % growth in 2015, and 7.9 % in 2016.

Clinker pyro-process is a high-energy intensive and low-efficient process, with a strong environmental impact. Constantly increasing fuels prices, besides always more demanding environmental regulations, are therefore pushing world cement producers to improve their processes and to continuously verify that these processes are run under optimized conditions [56][57][58][59][60][61]. Continuous improvement of the technology installed is a mandatory issue in order to keep economical competitiveness and enhance the process efficiency: in this context, the EU FP7 project DAPhNE (grant agreement n° 314636) brings together three manufacturing sectors including the clinker production, with common problems in relation to the energy consumption of their firing stages, seeking common solutions via the implementation of high-temperature microwave technologies based on self-adaptive control and innovative monitoring systems.

Section 2.1. introduces the conventional thermal process for clinker production; section 2.2. deals with the new microwave process.

2.1 – Conventional thermal process

EU cement production is distributed into 320 plants of which about 70 are grinding plants (i.e. no equipped with kilns). Only very few kilns have a capacity of less than 500 tones per day. Typical size of a modern installation is about 3000 tones per day.

Clinker manufacturing process progressively switched from "*wet*" systems (the leading technology in the 70's) to "*dry*" ones with the intermediate steps of the "*semi-wet*" and "*semi-dry*" processes. The main advantage of a modern dry process over a traditional wet system is the far lower fuel consumption, which is a consequence of the higher efficiency of the dry kiln.

The physical nature of the available raw materials influences the choice of the technological process, but today wet process is preferable only under very specific raw materials and process conditions. As a matter of fact, about 78 % of the current EU's cement production is from dry-process systems. Thus, the next discussion is focused on a typical dry process, whose operations are described hereafter.

2.1.1 - Quarrying

Raw materials are extracted from quarries which, in most cases, are located close to the cement plant. Raw materials for cement manufacture is a rock mixture which is about 80 % limestone (which is rich in $CaCO_3$) and 20 % clay minerals (a source of silica, alumina and Fe_2O_3).

Other raw materials may be used, such as shells or chalk, as a substitutes of limestone, and shale or slate, instead of clay minerals.

Corrective materials such as bauxite, iron ore or sand may be required to adapt the chemical composition to the requirements of the process and product specifications.

2.1.2 – Raw mixture preparation

Raw mixture preparation consists of a grinding operation, that is performed inside raw mills. Here the raw materials are fed together, then rocks are dried ground together until the desired particles size distribution is obtained (Table 2).

Lower size	0.1 μm
Mean size	8-12 μm
Higher size	200-250 μm

Table 2. Particles size distribution of raw meal.

Grinding is performed inside a raw mill, according to the following steps:
I.   Metering and proportion. The raw materials are dosed, in order to obtain the desired composition.
II.   Grinding and drying. Drying is performed using heat recovery from the exhaust gases provided by the kiln system.
III. Separation. Here large particles are removed by means of an air separator, so that they can be sent back to mill for further grinding.
After being ground, the raw meal is sent to the clinkering stage.

2.1.3 - Clinkering

As already mentioned, dry kilns are the most efficient, for this reason they have become the standard in cement production. This kind of kilns requires an ancillary equipment consisting of the following parts:
I.   Preheater. It was introduced in order to increase the efficiency of the kiln. The key component of the gas-suspension preheater is the cyclone. A cyclone is a conical vessel into which dust-bearing gas stream is passed tangentially, producing a vortex within the vessel. The gas exits the vessel through a co-axial "vortex-finder". The solids are thrown to the outside edge of the vessel by centrifugal action, and leave through a valve in the vertex of the cone. The number of cyclones stages used in practice varies from 1 to 6.
II.   Precalciner. It was developed in the 70's, and has subsequently become the equipment of choice for new large plants worldwide. The precalciner basically consists in a development of the suspension preheater: considering that the amount of fuel that can be burned in the kiln is directly related to the size of the kiln, if part of the fuel necessary to burn the raw mix is burned outside the kiln, the output could be increased by injecting extra fuel into the base of the preheater. So a precalciner consists of specially designed combustion chamber at the base of the preheater, into which pulverized coal is injected. The ultimate development is the "*air-separate*" precalciner, where the hot combustion air arrives directly from the cooler, bypassing the kiln. Typically, 60-75 % of the fuel is burned in the precalciner. In these systems, the feed entering the rotary kiln is 100 % calcined. The kiln has only to raise the feed to sintering temperature.

13

III.   Rotary kiln. After exiting the precalciner, the raw meal enters the cold end of the rotary kiln. Whilst moving towards the hot end, material gets heat by contact with both a hot gas phase and the rotating wall. Raw meal is sintered to clinker at temperatures between 1400 and 1450 °C. Chemical reactions involved are summarized hereafter:

- 900 to 1050 °C: CaO starts reacting with SiO_2 to form belite.
- 1300 to 1450 °C: partial (20-30 %) melting takes place, and belite reacts with calcium oxide to form alite. Alite is the characteristic constituent of Portland cement and it is thermodynamically unstable below 1250 °C, but can be preserved in a metastable state at room temperature by fast cooling. On slow cooling it tends to revert to belite.
- The partial melting causes the material to aggregate into lumps or nodules, typically of diameter 1-10 mm, which constitute the final clinker.

A typical modern installation is about 50 m long. Retention time of the material is around 20 minutes. The movement of the material towards the outlet is helped by the rotation and a slight inclination of the kiln. Filling level is maintained around 15 %. A multi-channel burner is located at the hot end of the kiln. Typical fuel is carbon; alternative fuels or mixes are also possible. Primary air is injected through the burner, with fuel particles in suspension. A second air flow coming from the heat recovery of the cooling stage, which is called secondary air, enters the kiln through the hot end; injection temperature is around 1000 °C, and helps the fuel to auto-ignite. Fuel combustion rises the temperature of the gas flow up to about 2000 °C. The gas flow moves countercurrent respect to the material bed. It exchanges heat with both the material and the wall, and finally is conveyed inside the precalciner. Typical temperature profiles for a short dry kiln are reported in Figure 4.

IV.   Cooler. The hot clinker falls into a cooler which recovers most of its heat, and cools the clinker to around 100-200 °C, at which temperature it can be conveniently conveyed to storage.

2.1.4 – Cement grinding

Ball mills are commonly used for grinding cement clinker. A ball mill basically consists of a large rotating drum containing grinding media, normally steel balls. As the drum rotates (around one revolution per second), the motion of balls crushes the clinker. The drum is generally divided into two or three chambers, with different size grinding media. As the clinker particles are ground down, smaller media are more efficient at reducing the particle size still further. Gypsum is ground together with the clinker in order to control the setting properties of the cement.
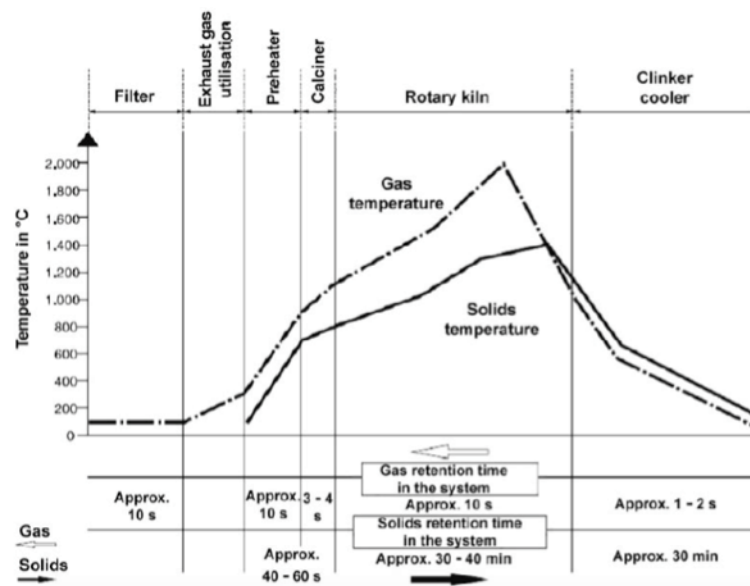
Figure 4. Temperature profiles in short-dry kilns [62].

2.2 – New microwave heating stage

In the new DAPhNE process the clinkering operation is performed inside a microwave applicator. The new technology has shown marked potentialities, both in terms of efficiency and reduction of polluting emissions. Also, the new heating stage allows for fast processing of the material, and may produce a relevant increase of the production capacity if scaled-up to industrial level.

The project has resulted in the implementation of a demonstrator with lab-scale capacity (10 kg/h). Here a high-power (10 kW), 910 MHz magnetron sends microwaves to a mono-modal resonant cavity, whose design is sketched in Figure 5. A ceramic tube is located inside the cavity. Its rotation, together with a slight inclination, allows the fed material moving from one end towards the other. When moving inside the tube, material absorbs microwaves. The rate of microwaves absorption is proportional to the loss factor of the material. Temperature dependency of the raw meal loss factor is reported in Figure 6. Several water circuits and a chiller avoid overheating of the instrumentation (magnetron, waveguide and cavity walls). A venting system removes the CO_2 produced by the $CaCO_3$ decomposition from the inside of the tube. This action is fundamental in order to avoid plasma formation, which would reduce the process efficiency. The new microwave heating stage is ideally located between the grinding and cooling operations. It replaces the whole kiln and provides heating of the raw meal from room temperature up to sintering.

As it can be noted, the loss factor increases with temperature. In particular, it shows an abrupt jump at 900 K. Therefore, the heating rate tends to increase when the temperature of the material goes up. This implies and intrinsic instability of the microwave process, and hot spots may appear suddenly if proper control actions are not undertaken.
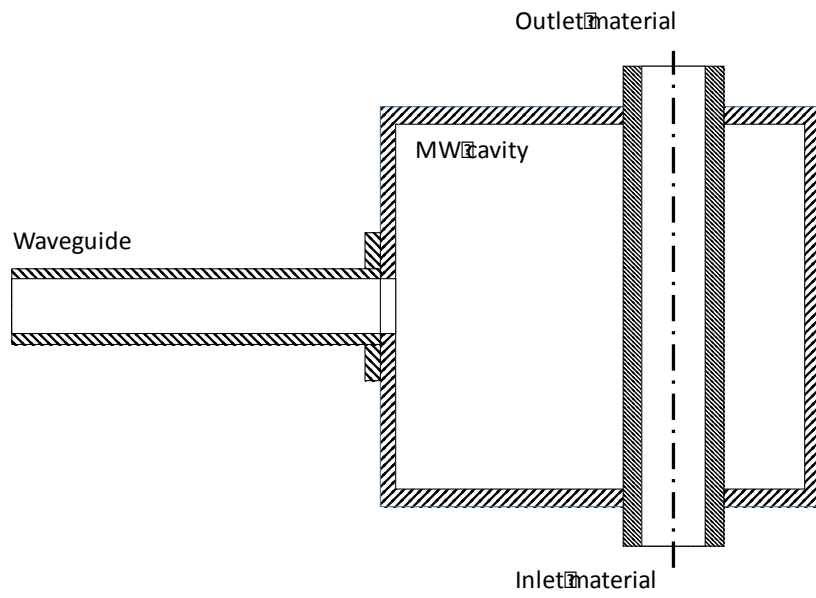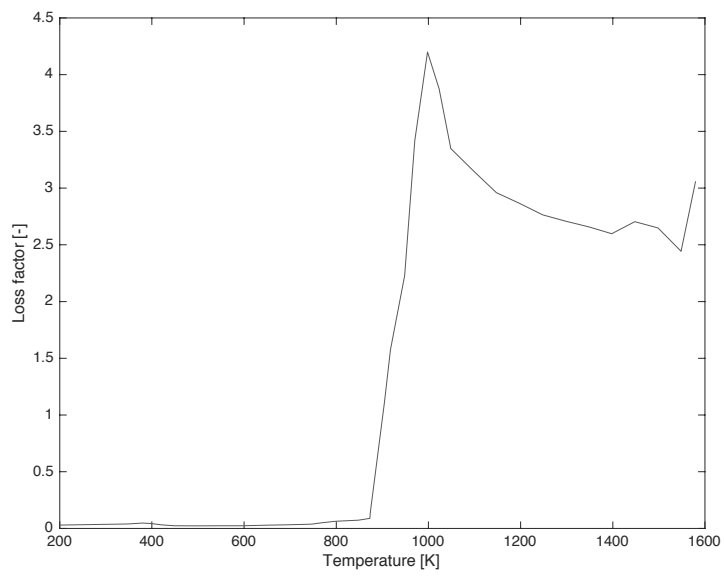
15

Figure 5. Microwave cavity.

Figure 6. Loss factor vs. temperature.

16

Section 3 – Soft sensing for conventional rotary kilns

Cement production is a high energy-intensive process, which is characterized by low efficiency and high environmental impact in terms of emissions. According to [63], "cement manufacturing is the third largest energy consuming and CO_2 emitting sector, with an estimated 1.9 Gt of CO_2 emissions from thermal energy consumption and production processes in 2006". Among the different stages constituting the cement production process, the one that impacts more heavily on both efficiency and emissions is clinker sintering, where the raw meal is heated from room temperature up to about 1450 °C. In [64] it is presented a energy audit on a 600 ton-clinker/day dry kiln: conclusions show that about 40 % of the total input energy is lost through hot flue gas (19.15 %), cooler stack (5.61 %) and kiln shell (15.11 % convection plus radiation).

World cement producers are currently facing constantly increasing fuels prices, besides always more demanding environmental regulations. Therefore, the improvement of process efficiency is a very actual topic for the cement industry. In this sense, multiple solutions have been proposed: they range from economies of scale, where size of the plant is increased in order to improve the competitiveness both in terms of costs and energy performances, to the continuous innovation of the technology installed. According to [63], "if Best Available Technologies can be adopted in all cement plants, global energy intensity can be reduced by 1.1 GJ/t-cement, from its current average value of 3.5 GJ/t-cement. This would result in CO_2 savings of around 119 Mt".

Technology innovation surely is essential for achieve better competitiveness. However, it is also complementary, and does not exclude, a continuous improvement of the knowledge related to the process. Indeed, efficiency-oriented operation strategies cannot disregard a complete and deep knowledge of the phenomena involved in the process itself. When referring to cement kilns for clinker sintering, it must be addressed a process that is highly complex for several reasons: a) it is characterized by multi-stage chemical reactions; b) there are radiative, convective and conductive heat exchanges, occurring in a wide range of temperatures; c) the process includes solid, liquid and gaseous phases, as well as powder phase. Moreover, there are several technical difficulties (moving parts, aggressive environment, etc.) that prevent to measure many process variables in a direct way. These whole aspects prevent an in-depth understanding of the process itself, so it has been usually approached as a black box, where process related control strategy mainly relies on the experience of the operator and/or on fuzzy approaches [65][66][67][68].

Within this context, the development of comprehensive and accurate numerical models that are able to describe all the thermo-chemical phenomena involved during clinker production is gaining importance. Kilns for clinker pyro-processing have been extensively studied. CFD turbulent models provide detailed representation of flame and aerodynamic phenomena inside the freeboard region [69][70][71][72][73][74][75][76][77]. Discrete Element Method models based on a Lagrangian approach are able to capture the behavior of a material bed being in powder state [78]. Boateng [79] proposed a quasi-3D model for the description of

thermal exchanges between the freeboard region and the material bed. Boateng's model, which was obtained by incorporating a 2D representation of the bed's transversal plane into a 1D plug flow model, was developed without accounting for chemical conversions of phase changes inside the material. A 1D model describing thermal exchanges and chemical conversion was developed by Spang [80]. Mujumdar [81] presented a model integrating two separate parts: a CFD approach was used for describing the freeboard region, whilst a 1D thermo-chemical model provided a representation of the solid material. Mastorakos [82] proposed an interesting approach, where an iterative procedure was exploited for achieving a comprehensive solution of the kiln's behavior. Predictions showed consistency with measurements in a full-scale plant, despite several simplifying assumptions were made.

Previous models, despite representing powerful tools for achieving deep knowledge of the process itself, may be considered as stand-alone tools with limited exploitation possibilities, because of extremely long computational times. On the other hand, the integration of theoretical tools to the monitoring and control architecture would result into obvious advantages: indeed, disposing of innovative soft sensors for esteeming critical and non-accessible process variables may lead to new optimization-oriented control approaches, where process efficiency is maximized in the respect of quality targets for the product.

Next part of this section describes an innovative monitoring approach for cement kilns based on soft sensing. The proposed soft sensor is based on a lumped element model (LEM) of the kiln. The model estimates the thermal and chemical variables from the operating set point of the kiln. The model is designed to provide predictions of a stationary behavior, and also forecasts of a transient response to one or more changes of the operation parameters. Computation times are extremely reduced. Therefore, the tool can be effectively exploited in on-line monitoring applications.

The LEM accounts for heat and mass balance equations, besides one equation describing fuel combustion. Critical parameters of the model have been adjusted using a multi-objective optimization strategy based on the application of a Genetic Algorithm (GA) inside the MATLAB® environment. The optimization has been conduced using predictions from a comprehensive CFD-FEA model as reference. The reference model has been developed using the COMSOL® Multiphysics framework, then validated by comparing its predictions with real data. After the optimization, the LEM has shown good accuracy. At the same time its computation requirements are compatible with real-time applications.

Next part of this section is organized as follows: a) subsection 3.1. describes the real kiln considered in the test case; b) subsection 3.2. introduces the CFD-FEA model; c) subsection 3.3. faces the development of the LEM and its optimization; d) subsection 3.4. is focused over the results.

3.1 – The real kiln

The kiln considered is a short dry one for clinker production (length 54 m, external radius 2.3 m, internal radius 2.1 m) installed in the production plant. The kiln can process up to 140 T/h (total mass flow) of material.

The material enters the kiln almost completely calcined at a temperature of 950 °C, then it is heated up to a maximum temperature of 1450 °C. This temperature is reached in the so-called sintering zone. Secondary air (i.e. air coming from the heat recovery circuit) enters the kiln

a rate of 80 m^3/s and at a temperature of 1300 °C. Primary air is injected at ambient temperature through a multi-channel burner, at a flow rate of 5700 m^3/h. Pulverized coal (7300 kg/h total mass flow) is transported in suspension with the primary air. The kiln is operated at a slight depression of -20 mmH$_2$O respect to the atmospheric pressure, thus forcing gas extraction and conveying towards the precalciner. The kiln is rotated at 3.5-4.2 rpm (rotational speed range) and it is titled at a 2 deg angle (relative angle between the kiln axis ant the horizontal plane). The filling level is 15 % and the retention time (i.e. the time spent by the material inside the kiln while moving towards the outlet) is 20 min.

Table 3 reports thermo-physical properties of both the fuel and the material bed. The chemical composition of the fresh raw meal (i.e. the raw meal at ambient temperature, before entering the precalciner) is reported in Table 4. All data mentioned have been collected from the real cement production plant. The following measurements have been also made available for assessing the correctness of the model developed: maximum, minimum and average temperature of the external shell of the kiln; maximum temperature of the material bed in the sintering zone; temperature of the material bed at the outlet of the kiln; flame temperature; average speed of the gas inside the kiln. These variables are reported in Table 5.

Thermal conduction material bed	1.4 W/m·K
Bulk density material bed	700 kg/m^3
Specific heat material bed	0.25 kCal/g·K
Bulk density fuel	1 T/m^3
Heat of combustion fuel	2.6e7 J/kg

Table 3. Thermo-physical properties of fuel and the material bed.

	Mass fraction (%)
SiO$_2$	14
Al$_2$O$_3$	2.68
Fe$_2$O$_3$	2
CaO	43
MgO	2.6
Loss on Ignition	34.5

Table 4. Chemical composition of fresh raw meal.

Maximum T external shell	329 °C
Minimum T external shell	194 °C
Average T external shell	271 °C
T material sintering	1450 °C
T material out	1300 – 1400 °C
T flame	1800 – 2100 °C
Average speed gas	12 – 17 m/s

Table 5. Measurements.

3.2 – CFD-FEA model

The kiln has been modelled using the COMSOL® Multiphysics framework, which allows to efficiently integrate the different physics involved in the clinker production process. Geometry of the kiln is shown in Figure 7.
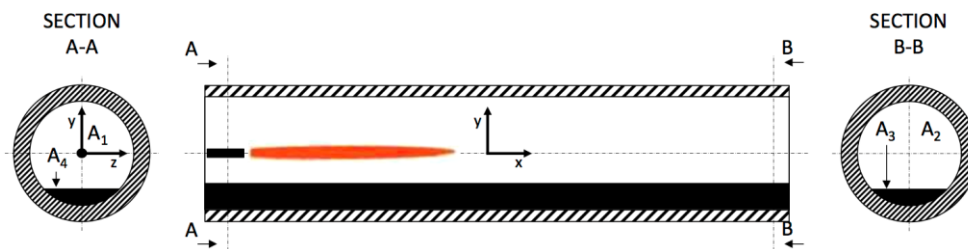

Figure 7. Geometry of the kiln.

Quadratic elements were used for a mapped wall mesh. Tetrahedral elements were used for meshing the material bed and the freeboard domain, with a progressive mesh refinement towards the area of the burner. The final mesh accounts five hundred thousand nodes. The accuracy of the model was verified by checking the convergence of the maximum temperature of the material (T_{max}) after progressive mesh refinements. Mesh elements on a vertical cross-section of the kiln are shown in Figure 8.

The final model was obtained by integrating the following analyses: a) a CFD analysis of the freeboard domain; b) transport and diffusion of pulverized fuel with the primary air; c) fuel oxidation; d) propagation of radiation inside the freeboard domain; e) conductive, convective and radiative heat exchanges between the freeboard region, the wall and the material bed; f) conductive heat transfer inside the wall and the material bed; g) chemical conversion of the material bed. Each analysis is discussed in detail in the following subsections. A full list of symbols is provided in Appendix A.2.
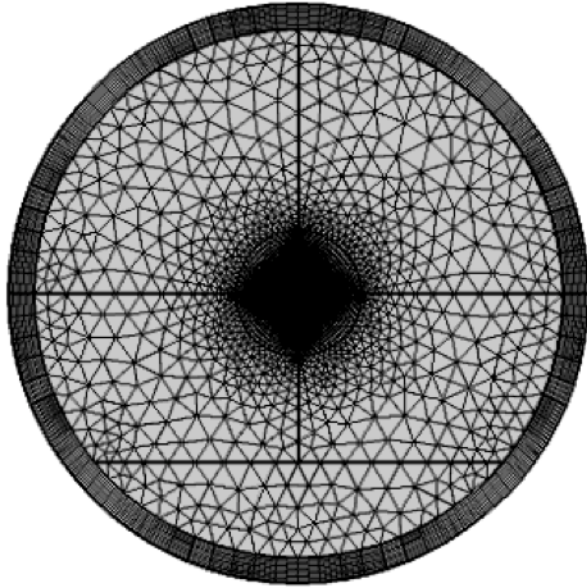
Figure 8. Mesh elements on a vertical cross-section.

3.2.1 – CFD analysis of the freeboard region

The freeboard region is described with a non-isothermal, $k - \varepsilon$ turbulent model. The energy equation accounts for a source term, Q_f, that represents the heat generated by the fuel oxidation. Equation 9 reports the analytical expression of Q_f:

$$Q_f = \Delta h_f \cdot R_f \cdot c_f \tag{9}$$

In eq. 9, Δh_f represents the enthalpy of the reaction, R_f the rate of the reaction, and c_f the mass concentration of fuel. The analytical expression of R_f is discussed in subsection 3.2.3.

The following boundary conditions are considered: a) a total mass flow of 80 m³/s of secondary air at a temperature of 1000 °C in the A_1 section (see Figure 7); b) an absolute pressure of 1.008e5 Pa in the A_2 section.

The burner is modelled with three channels. The external channel provides the axial air, and it is characterized by an axial tilt, with respect to the kiln rotation axis, of 5 deg. The intermediate channel is orthogonal to the axis of the kiln and provides the transport air, i.e. the air with fuel particles in suspension. The internal channel shows an axial tilt of -3 deg with respect to the axis of the kiln and it provides the swirl air. The primary air enters the three channels at ambient temperature and at a total flow rate of 5700 m³/h. The swirl air exhibits a tangential velocity component in the circumferential direction of 100 m/s, which corresponds to a 150 rpm rotational speed of the burner.

3.2.2 – Transport and diffusion of pulverized fuel with the primary air

Fuel transport is described by eq. 10:

$$\nabla \cdot \left(-D_f \cdot \nabla c_f \right) + u_g \cdot \nabla c_f = R_f \tag{10}$$

In eq. 10 c_f is the mass fraction of fuel, u_g is the velocity field of the freeboard domain, D_f is the diffusivity and R_f is the rate of the reaction.
Fuel enters the kiln at a flow rate of 7300 kg/h, through the inlet section of the carrier air. A zero x-gradient condition for c_f is imposed in the A_2 section.

3.2.3 – Fuel oxidation

The model representing fuel oxidation is the one proposed by Spang [80]. Here the rate of oxidation R_f' of a single particle is described by eq. 11:

$$R_f' = k_f \cdot d_O \cdot C_{O2} \tag{11}$$

Where C_{O2} is the O_2 concentration; d_O is the sub-fraction of CO_2 being effectively available at the surface of the particle; k_f is the rate constant, whose temperature dependency is expressed according to the Arrhenius formulation reported in eq. 12:

$$k_f = A_f \cdot exp\left(\frac{-E_f}{R_g \cdot T_g} \right) \tag{12}$$

In eq. 12, A_f is the pre-exponential factor, E_f the activation energy, R_g the gas constant and T_g the temperature field of the freeboard domain. The analytical expression of d_O is obtained from a 1D diffusion model and it is reported in eq. 13:

$$d_O = \frac{\frac{3D_O}{r_f^2 \cdot k_f}}{\frac{3D_O}{r_f^2 \cdot k_f} + 1} \tag{13}$$

In eq. 13, r_f is the radius of the particle and D_O the diffusion constant of oxygen. A more exhaustive discussion about the 1D diffusion model is reported in [80].
The total rate of reaction R_f is a function of R_f' and the fuel-to-air ratio α; its final expression is reported in eq. 14:

22

$$R_f = R_f' \cdot \alpha = R_f' \cdot \frac{F_f \cdot \rho_g \cdot M_C}{F_g \cdot \rho_f} \tag{14}$$

Where M_C is the molecular weight of fuel; F_f, ρ_f, F_g and ρ_g are the mass flow and the density of fuel and air, respectively.

3.2.4 – Propagation of radiation inside the freeboard region

The radiative intensity $I(\Omega,s)$ at position s and direction Ω is expressed by eq. 15:

$$\Omega \cdot \nabla I(\Omega, s) = k \cdot I_b(T_g, n) - \beta \cdot I(\Omega, s) + \frac{\sigma_s}{4\pi} \int_0^{4\pi} I(\Omega, s) \cdot \phi(\Omega', \Omega) \cdot \partial \Omega \tag{15}$$

Where k, β and σ_s are the absorption, extinction and scattering coefficients of the gas media, respectively. $I_b(T_g,n)$ is the blackbody radiation intensity, which is a function of both the temperature and the refractive index n of the medium.

3.2.5 – Radiative, convective and conductive heat exchanges between the freeboard gas, the material bed and the wall

The convective heat exchange coefficient is expressed by the Nusselt number Nu of the CFD domain (eq. 16):

$$Nu = \frac{h \cdot d}{k_g} \tag{16}$$

Where h is the convective thermal transmittance, d the characteristic length and k_g the thermal conductivity of the fluid. Nu is calculated from the Reynolds and Prandtl numbers of the CFD domain.
The net radiative heat exchange between the exposed surfaces of the internal wall and the material bed is also accounted.
The conductive heat exchange between the material bed and the wall is calculated assuming a 200 W/m^{2}K heat exchange coefficient, as indicated in [83][84].

3.2.6 – Heat conduction inside the wall and the material bed

The heat equation involving the wall and the material bed is reported in eq. 17:

$$\rho_{s,w} \cdot c_{s,w} \cdot \left(\frac{\partial T_{s,w}}{\partial t} + u_{s,w} \cdot \nabla T_{s,w} \right) = k_{s,w} \cdot \nabla^2 T_{s,w} + Q_s \tag{17}$$

In eq. 17, $\rho_{s,w}$, $c_{s,w}$, $k_{s,w}$ are the mass density, the specific heat and the thermal conductivity of the material bed and the wall, respectively; u is the velocity field. The wall domain rotates at 3.8 rpm, while the material bed undergoes a translational speed (along the kiln) of 45 mm/s. Such translational speed corresponds to a retention time of 20 minutes. The source term Q_s represents the heat absorbed or generated by the chemical conversions inside the material bed.

The thermo-physical properties characterizing the material bed are reported in Table 3. Wall properties are taken from a typical brick refractory.

A temperature of 950 °C is imposed in the A_3 section. A zero x-gradient condition for T_s is imposed in the A_4 section. The external shell of the kiln dissipates heat towards the environment (temperature of the environment is 20 °C). An emissivity value of 0.9 is assumed for the external surface of the kiln, whilst the convective heat exchange coefficient is set to 10 W/m²K.

3.2.7 – Chemical conversion of the material bed

Chemical conversion inside the material bed is calculated according to the set of eqs. 69 to 77, which are reported in Appendix A.2. The initial mass fractions for the chemical species are obtained from Table 4 by subtracting the Loss on Ignition to the total mass; the values thus estimated are reported in Table 6. Equations from 69 to 77 are solved through an external routine (developed in MATLAB®) coding the iterative procedure represented in Figure 9. Here an initial solution Sol_1 is obtained from COMSOL®, by assuming a zero heat source $Q_{s,0}$ inside the material bed; a MATLAB® solver for ordinary differential systems (ode23) provides the solution $Chem_1$ of eqs. from 69 to 77 assuming the temperature field $T_{s,1}$ from Sol_1; the heat source $Q_{s,1}$ is calculated according to eq. 78; Sol_2, assuming the heat source $Q_{s,1}$, is then estimated. All these steps are iterated until the relative variation of $Q_{s,i}$ with respect to $Q_{s,i-1}$ is lower then a predefined threshold (1e-3).
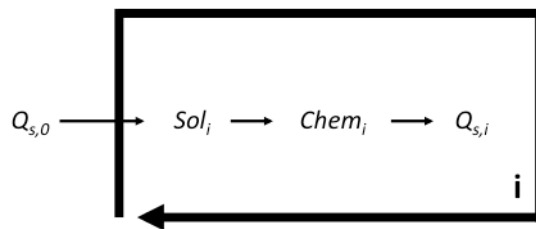

Figure 9. Iterative routine for calculating chemical conversion.

	Mass fraction (%)
SiO_2	21.37
Al_2O_3	4.09
Fe_2O_3	3.05
CaO	65.65
MgO	3.96

Table 6. Initial mass fractions.

3.3 – Lumped element model

Rotary kilns are heat exchangers, where the material bed moves counter-current to the gas of the freeboard region. A lumped element-based description of the whole system can be achieved by assuming four different nodes representing, respectively, the external wall, the internal wall, the freeboard gas and the material bed.

The heat balances for each node are reported in eqs. 18 to 31. In these equations Q_f represents the heat produced inside the gas from fuel combustion; the rate of combustion R_f is calculated according to the same 1D diffusion model used in [80] (eq. 22); Q_c represents the heat generated/absorbed inside the material bed by exothermic and endothermic chemical conversions. Q_c can be expressed by knowing the reactions involved in clinker sintering, besides their enthalpies and rates (see Table 7). Equations 23 to 31 represent mass balances for fuel and solid species. Saeman equation [85] provides correlation of the filling level with the operative parameters of the kiln (i.e. rotating speed, tilt angle and mass flow). Detailed expressions of the different terms appearing in eqs. 18 to 31, besides a full list of symbols, are reported in Appendix A.3.

$$\rho_g c_g A_g v_g \cdot \frac{\partial T_g}{\partial x} = Q_f + h_{gw}(T_w - T_g) + h_{gs}(T_s - T_g) \tag{18}$$

$$\rho_s c_s A_s \cdot \left(\frac{\partial T_s}{\partial t} + v_s \frac{\partial T_s}{\partial x}\right) = Q_c + h_{sw}(T_w - T_s) + h_{gs}(T_g - T_s) \tag{19}$$

$$\rho_w c_w A_{wi} \cdot \frac{\partial T_{wi}}{\partial t} = h_{gw}(T_g - T_{wi}) + h_{sw}(T_s - T_{wi}) + \frac{k_w}{r_e - r_i}(T_{we} - T_{wi}) \tag{20}$$

$$\rho_w c_w A_{we} \cdot \frac{\partial T_{we}}{\partial t} = \frac{k_w}{r_e - r_i}(T_{wi} - T_{we}) + h_{env}(T_{env} - T_{we}) \tag{21}$$

25

$$\frac{\partial C_f}{\partial x} = -\frac{R_f}{v_g} \tag{22}$$

$$\frac{\partial C_{CaCO3}}{\partial t} = -v_s \frac{\partial C_{CaCO3}}{\partial x} - R_{CaCO3} \tag{23}$$

$$\frac{\partial C_{CaO}}{\partial t} = -v_s \frac{\partial C_{CaO}}{\partial x} + \frac{M_{CaO}}{M_{CaCO3}} R_{CaCO3} - 2 \frac{M_{CaO}}{M_{C2S}} R_{C2S} - 3 \frac{M_{CaO}}{M_{C3A}} R_{C3A}$$
$$- 4 \frac{M_{CaO}}{M_{C4AF}} R_{C4AF} - \frac{M_{CaO}}{M_{C3S}} R_{C3S} \tag{24}$$

$$\frac{\partial C_{SiO2}}{\partial t} = -v_s \frac{\partial C_{SiO2}}{\partial x} - \frac{M_{SiO2}}{M_{C2S}} R_{C2S} \tag{25}$$

$$\frac{\partial C_{Al2O3}}{\partial t} = -v_s \frac{\partial C_{Al2O3}}{\partial x} - \frac{M_{Al2O3}}{M_{C4AF}} R_{C4AF} - \frac{M_{Al2O3}}{M_{C3A}} R_{C3A} \tag{26}$$

$$\frac{\partial C_{Fe2O3}}{\partial t} = -v_s \frac{\partial C_{Fe2O3}}{\partial x} - \frac{M_{Fe2O3}}{M_{C4AF}} R_{C4AF} \tag{27}$$

$$\frac{\partial C_{C2S}}{\partial t} = -v_s \frac{\partial C_{C2S}}{\partial x} + R_{C2S} - \frac{M_{C2S}}{M_{C3S}} R_{C3S} \tag{28}$$

$$\frac{\partial C_{C3A}}{\partial t} = -v_s \frac{\partial C_{C3A}}{\partial x} + R_{C3A} \tag{29}$$

$$\frac{\partial C_{C4AF}}{\partial t} = -v_s \frac{\partial C_{C4AF}}{\partial x} + R_{C4AF} \tag{30}$$

$$\frac{\partial C_{C3S}}{\partial t} = -v_s \frac{\partial C_{C3S}}{\partial x} + R_{C3S} \tag{31}$$

The mathematical system accounts for a total of 14 variables, and provides a lumped element-based description of the thermal and chemical phenomena involved in clinker sintering.
The numerical solution of the system involving eqs. from 18 to 31 is obtained through an iterative routine, which ensures a fast and robust (i.e. convergence for a wide range of input parameters) execution. Two numerical methods, specifically developed for handling steady and transient problems, have been developed. A detailed description of both is reported hereafter.

Reaction	Enthalpy (J/kg)	Pre-exp. (1/s)	Act. En. (J/mol)
$CaCO_3 \rightarrow CaO + CO_2$	1.66e6	4.55e31	7.81e5
$2CaO + SiO_2 \rightarrow C2S$	-6.03e5	4.11e5	1.93e5
$3CaO + Al_2O_3 \rightarrow C3A$	-3.7e4	8.33e6	1.94e5
$4CaO + Al_2O_3 + Fe_2O_3 \rightarrow C4AF$	-1.09e5	8.33e8	1.85e5
$C2S + CaO \rightarrow C3S$	-4.48e5	1.33e5	2.56e5

Table 7. Reactions involved in clinker sintering [80].

3.3.1 – Steady simulation

In the steady problem all the spatial derivatives in eqs. 18 to 31 are set to zero. As a consequence, eqs. 20 and 21 become algebraic equations. The numerical problem thus turns out in a Boundary Value Problem (BVP) [86], associated with a set of 12 first-order, non-linear Ordinary Differential Equations (ODEs). The following aspects contribute to make the achievement of a numerical solution tricky: a) non-linearity of the heat balance equations; b) strong coupling between the heat and mass balance equations; c)the problem is a BVP one, and its numerical solution is more complicated with respect to an Initial Value Problem (IVP) [86].

The numerical solution is obtained by dividing the initial system into two different subsystems: a) the thermal system, which accounts for the heat balances (eqs. 18 to 21) and the fuel mass balance (eq. 22); b) the chemical system, which includes the mass balance equations for all the solid species (eqs. 23 to 31). The chemical system is an IVP because all the boundary conditions (BCs) are defined at the kiln inlet (x=0). On the contrary, the thermal system represents a BVP because eq. 19 requires a BC at x=0, whilst the BCs for eqs. 18 and 22 are imposed at x=L, being L the kiln otlet. However, the thermal system can be reformulated as an IVP with all the BCs defined at x=L by using the shooting method [86] on eq. 19; its application is described hereafter.

$$\begin{cases} \dfrac{dT_s}{dx} = f(T_s, x) \\ T_s(0) = T_{s,in} \end{cases} \longrightarrow \begin{cases} \dfrac{dT_s}{dx} = f(T_s, x) \\ T_s(L) = \alpha \end{cases} \tag{32}$$

The shooting method replaces the Dirichlet BC at z=0 with a guess, the α term, at x=L. The α term is calculated as the term that minimizes the following condition:

$$\alpha = argmin_\alpha\big[abs\big(T_s(\alpha)|_{x=0} - T_{s,in}\big)\big] \tag{33}$$

27

The application of the shooting method to eq. 19 is graphically depicted in Figure 10: here it can be well appreciated the variation of the thermal solution when changing the guess on the temperature of the material at the outlet of the kiln ($T_{s,out}$).
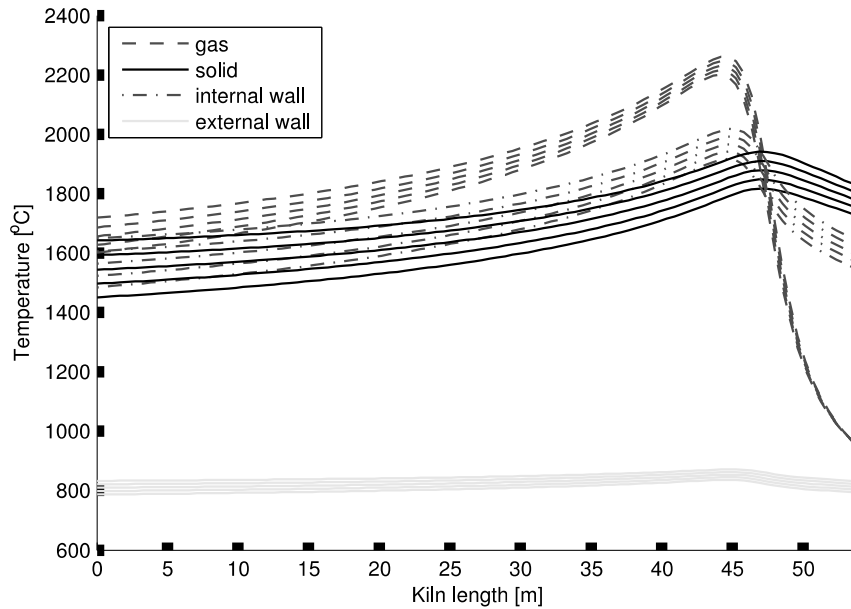

Figure 10. Application of the shooting method.

The numerical solution of the whole system (thermal plus chemical) is obtained through the following steps:

I. Q_c, T_s, T_g, T_{wi} and T_{we} are set to zero; this represents the initialization step.
II.   The thermal system is addressed at first, by assuming Q_c as a known parameter. The thermal system is therefore decoupled from the chemical one. The shooting method is applied to eq. 19, then the numerical solution is obtained with a MATLAB® solver for IVPs (ode23).
III. T_s, T_g, T_{wi}, T_{we} are updated according to the solution of the thermal problem.
IV.   The chemical system is then addressed, by assuming the thermal profiles as known parameters. The chemical system is therefore decoupled from the thermal one, and the numerical solution is obtained with a MATLAB® solver for IVPs (ode23).
V. Q_c is updated according to the chemical solution.

Steps *II* to *V* are iterated until the Root Mean Square Vector Difference (RMSVD) between solutions *n* and *n-1* is smaller than a predefined threshold (1e-3).

The steady solver has been successfully tested at different operating conditions. Correctness of the solution has been verified by comparing it with another obtained with a MATLAB® BVP solver (bvp4c), see Figure 11 for comparison (convergence of bvp4c has been possible only by providing an initial guess consisting of the solution obtained with the present

routine). Computational time for steady solution is lower than 1.5 s on a i5 Dual Core 8 Gb RAM PC.
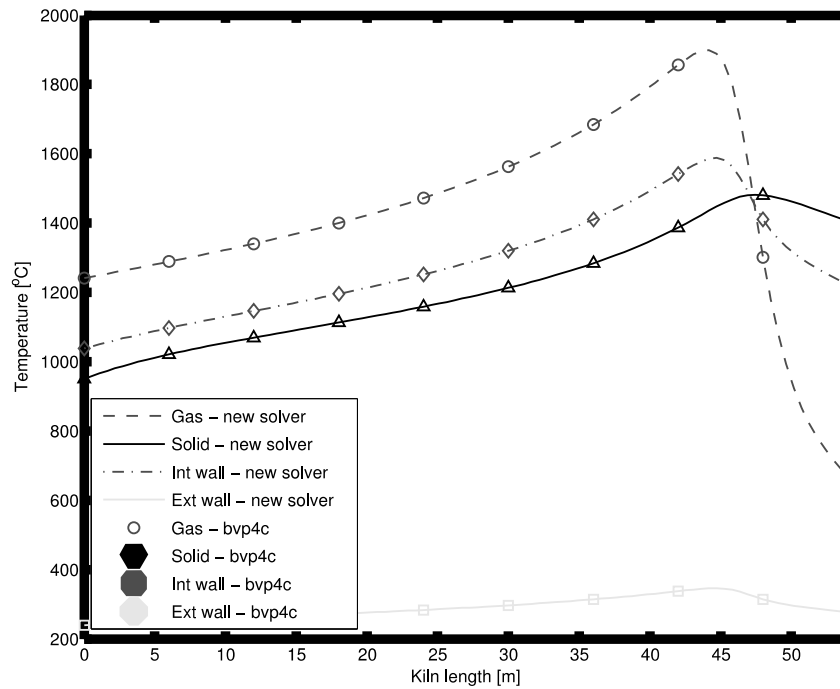

Figure 11. Temperature profiles from iterative routine (continuous line) and bvp4c (dots).

3.3.2 – Transient simulation

A Finite Difference Method (FDM) [86] for discretizing the spatial derivatives is exploited for solving the transient problem. The system obtained after the application of the FDM is a set of $14*N_I$ (being N_I the number of evaluation points) ordinary differential equations, which constitute an IVP in time domain. The initial state is obtained from the steady solver, and then a MATLAB® solver for IVPs (ode23) performs integration in time domain. Attention must be paid in order to meet the Courant-Fridrichs-Lewy (CFL) condition [87]: a maximum time step must be imposed according to N_I. Computational time is strictly related to N_I, as the latter influences both the dimension of the system and the maximum admissible time step. Indeed, when considering a discretization in one hundred lines, transient simulation over a 3600 s time period requires less then 10 s on a i5 Dual Core 8 Gb RAM PC, which can be considered a short time when compared to the typical time scales of a process deviation.

29

3.3.3 – GA-based optimization

The LEM developed does not provide a mathematical representation of the aerodynamic phenomena inside the freeboard region. Thus an analytical calculation of the gas velocity, besides convective heat exchange coefficients, is not possible. However, a comparison of LEM results with the reference CFD-FEA prediction could be effective in providing an a-posteriori estimation of the aforementioned parameters.

For this purpose, the MATLAB® GA-optimization environment has been used for driving the adjustment of these parameters. The optimization step aimed at minimizing several objective functions, by varying the input parameters reported in Table 8. The objective functions are defined for each variable y_{LEM} of the LEM, and they represent the RMSVD calculated respect to the correspondent variable of the CFD model y_{CFD}. The analytical expression is reported in eq. 34:

$$RMSVD_y = \sqrt{\frac{\sum_{i=1}^{N_2}\left(y_{i,LEM} - y_{i,CFD}\right)^2}{N_2}} \tag{34}$$

Being N_2 the number of equal spaced evaluation points along the x coordinate. The main parameters of the GA-optimization are reported in Table 9, while the projection of the final Pareto front on a two objectives-plane is shown in Figure 12.

	Min	**Max**
v_g	11 m/s	15 m/s
$Conv_{gs}$	10 W/m^{2}K	200 W/m^{2}K
$Conv_{gw}$	10 W/m^{2}K	200 W/m^{2}K

Table 8. Variation ranges for the input parameters.

Solver	MATLAB GA algorithm
Crossover function	Scattered
Mutation function	Gaussian
Population size	20

Table 9. Parameters of the GA optimization.

Among the solutions constituting the Pareto front, the solution providing the absolute minimum for the deviation between the temperature profiles of the material bed was chosen. The correspondent values for v_g, $Conv_{gw}$ and $Conv_{gs}$ are 14 m/s, 40 W/m^{2}K and 40 W/m^{2}K, respectively.

Figure 13 shows the LEM steady solution after the optimization. A comparison of the LEM solution with the reference CFD-FEA prediction is shown in Figure 14. Figure 13a shows the

temperature profiles of the material bed, the freeboard gas, the internal wall and the external wall. Figure 13b shows the fuel concentration, i.e. the fuel mass flow normalized respect to the initial mass flow at *x=L*. Figure 13c and Figure 13d show the profiles of the initial and final chemical species, respectively. A direct comparison between the LEM predictions and measurements from the real plant is reported in Table 10: an overall agreement in the order of 1 % can be noticed; mass fraction values of 55 % for C3S and 20 % for C2S for the final clinker composition are consistent with the typical fractions indicated by literature [54].
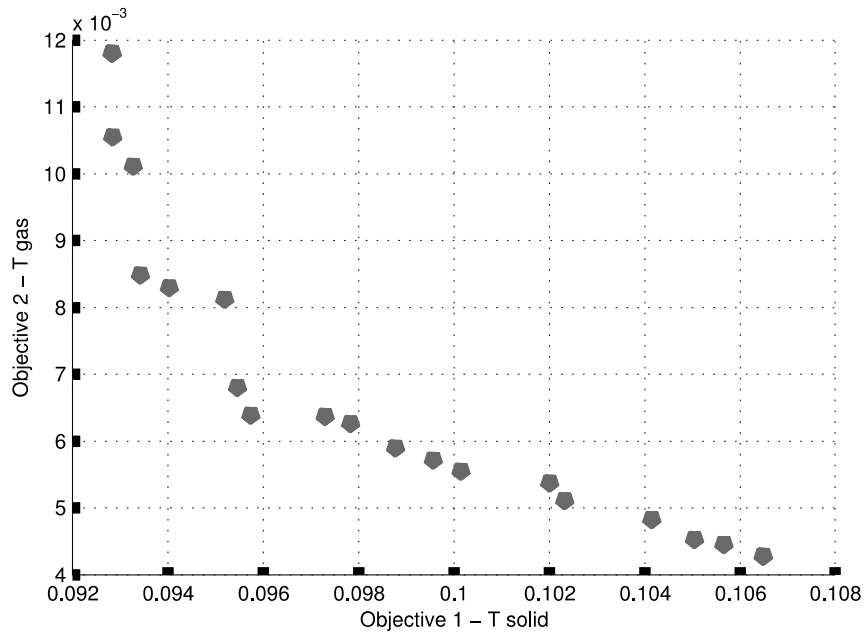
Figure 12. 2D-projection of the Pareto front.

	Measured	**Simulated**
Maximum T external shell	329 °C	333 °C
Minimum T external shell	194 °C	205 °C
Average T external shell	271 °C	275 °C
T material sintering	1450 °C	1448 °C
T material out	1300 – 1400 °C	1409 °C
T flame	1800 – 2100 °C	1900 °C

Table 10. LEM steady solution compared to measurements.

a) b)

c) d)
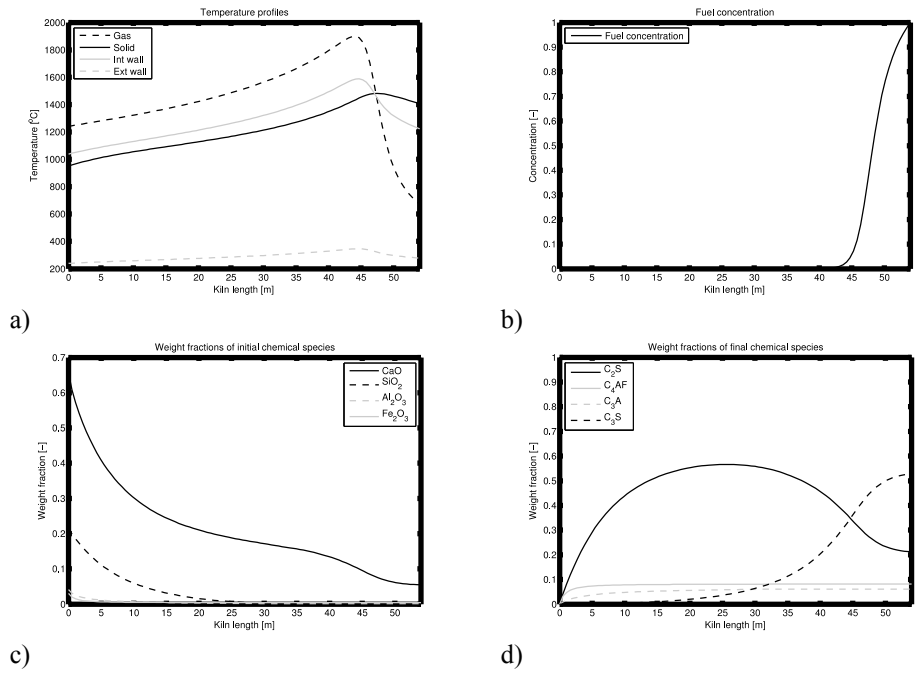
Figure 13. LEM steady solution after optimization.

The lumped element model is provided with a Graphical User Interface (GUI) for the operator. Appendix A.4 reports a "*Read me*" file for its installation and use.
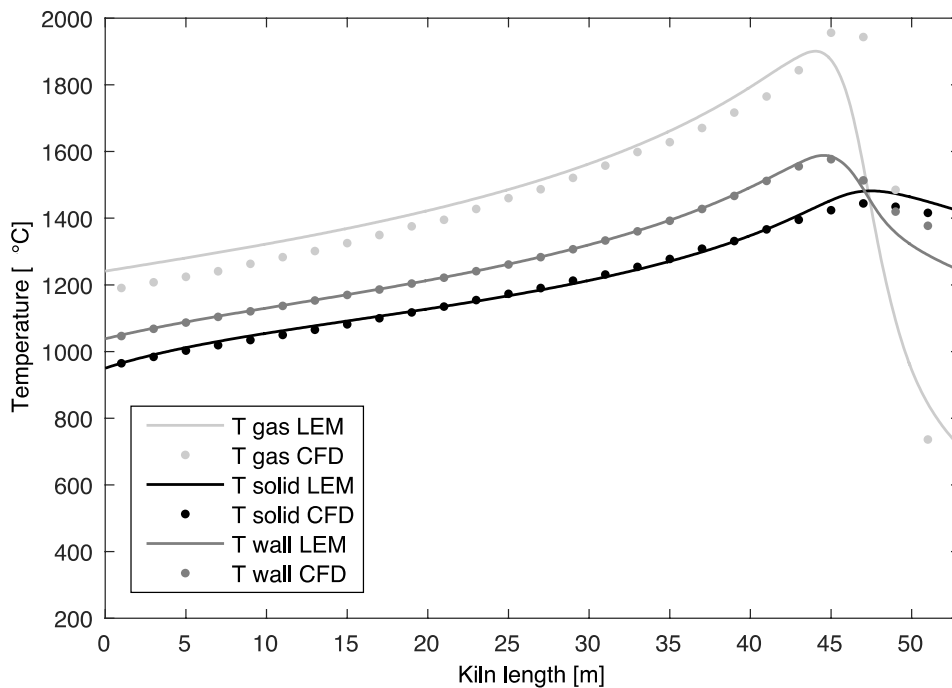
Figure 14.. Temperature profiles – comparison between LEM prediction and CFD-FEA model.

3.4 - Results

3.4.1 – CFD-FEA model

This section discusses the results of the CFD-FEA simulation. A comparison between simulated data and information retrieved from the real plant is also provided.

Figure 15 shows the *x*-direction velocity field of the freeboard region on a *xy*-cross sectional plane. The streamlines in the area near the burner are shown in Figure 16. The swirl air exhibits a strong out-of-plane velocity component impressed by the rotation of the burner, which is highly effective in increasing the rate of mixing between the carrier air and the secondary air, thus improving the efficiency of the combustion. Close to the burner, the primary and the secondary air show different magnitudes of speed. Moving towards the other end of the kiln the primary air progressively decreases its speed, and the *x*-component of the velocity field sets up to an average value of 15 m/s, which is in good agreement with field data (12-17 m/s).
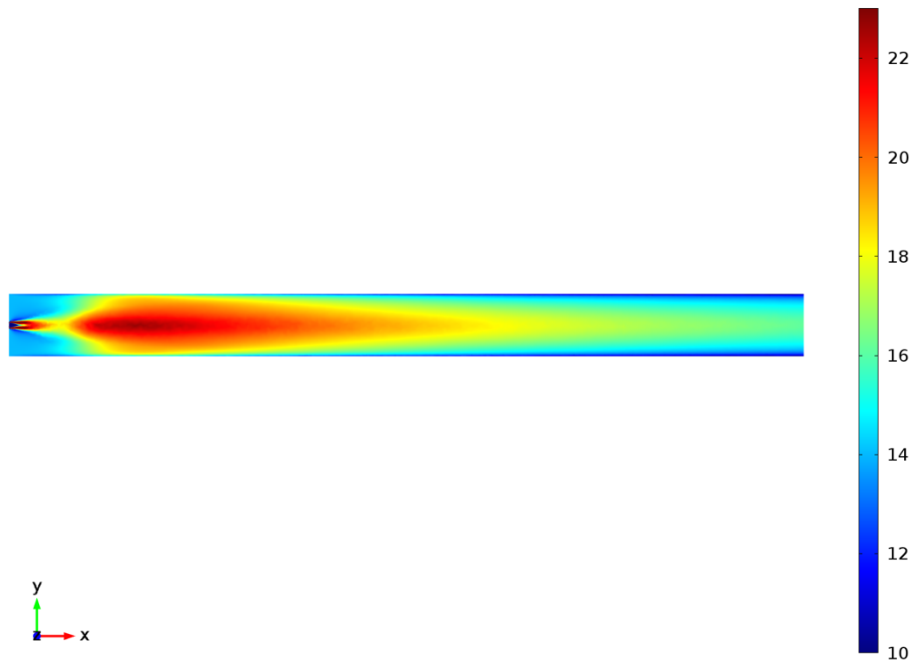
Figure 15. x-direction velocity field (m/s) – freeboard region.

Figure 17 shows the fuel concentration in the area close to the burner. The fuel enters the kiln through the carrier air, and then the gas transports it. Whilst moving inside the kiln, the temperature of the fuel is increased by heat exchange with the secondary air, until it reaches auto-ignition. The preheating of the fuel up to the auto-ignition condition is improved by the turbulent regime near the burner. Indeed, this regime enhances the heat redistribution between primary and secondary air. After auto-ignition, the fuel starts reacting with the free oxygen. The exothermic reaction increases the temperature of the gas up to 2013 °C. After that, the fuel concentration coherently goes to zero, as a consequence of its consumption during the oxidizing reaction.

Figure 18 and Figure 19 present the temperature distribution inside the freeboard region. The flame in the sintering zone of the kiln, which starts when the fuel reaches auto-ignition, is clearly visible. Temperature of the secondary air and the flow rate of the primary air influence the position of the ignition point: indeed, these aspects affect the preheating rate of the fuel when it enters the kiln. Simulation indicates a flame temperature of 2013 °C, which fits in the range of temperatures observed in the real kiln (1800-2100 °C). The high flame temperature entails strong radiation in the sintering zone, thus increasing the heating rate of the material in this part of the kiln. Moving towards the other end of the kiln, the gas exchanges heat with the material bed and the wall. Therefore, the gas temperature reduces.

34

The gas exits the kiln at a temperature of about 1200 °C, then it is moved towards the precalciner.

The temperature distribution of the material bed is shown in Figure 20. It is interesting to analyze the temperature profiles (i.e. cross-sectional average temperature vs. x-position) for the gas, the wall and the material bed (see Figure 21). The material exhibits a continuous heating when it moves along the kiln, as a consequence of the heat exchange with the gas and the wall; in particular, the rotating wall provides a fundamental heat-exchange contribution, by receiving heat from the freeboard gas and releasing it to the material bed through the contact area. The material reaches a maximum temperature of 1445 °C in the sintering zone, where the flame provides strong radiation. When moving towards the exit of the kiln, the temperature of the material decreases to 1398 °C. Again, results of the simulation are consistent with data from the real kiln (see Table 5).

Figure 22 shows the chemical profiles (i.e. mass fractions vs. x-position) of C2S, C4AF, C3A and C3S along the kiln. The mass fractions for C2S and C3S (the two major components) at the outlet are consistent with data from literature [54].
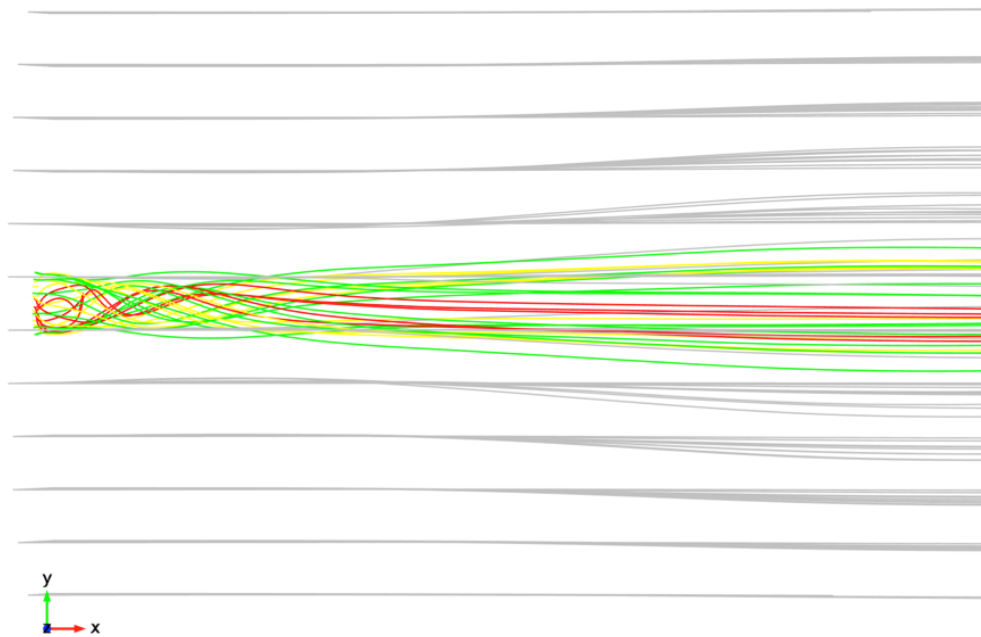
Figure 16. Streamlines – burner area.
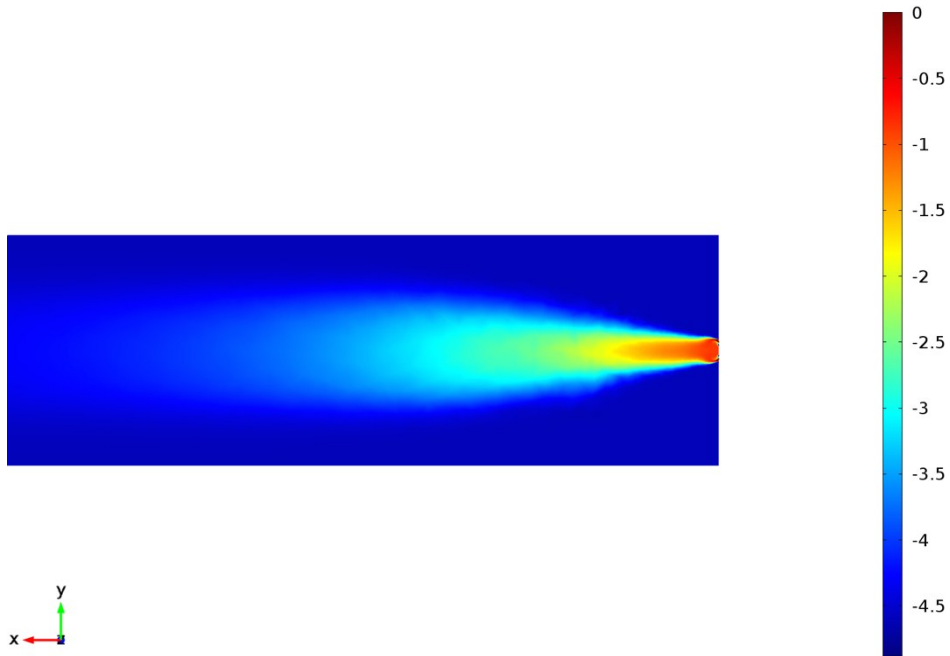
Figure 17. $\log\left(\dfrac{c_f}{c_{f\_inlet}}\right)$ – *burner area.*

Figure 18. Temperature field (K) – freeboard region.
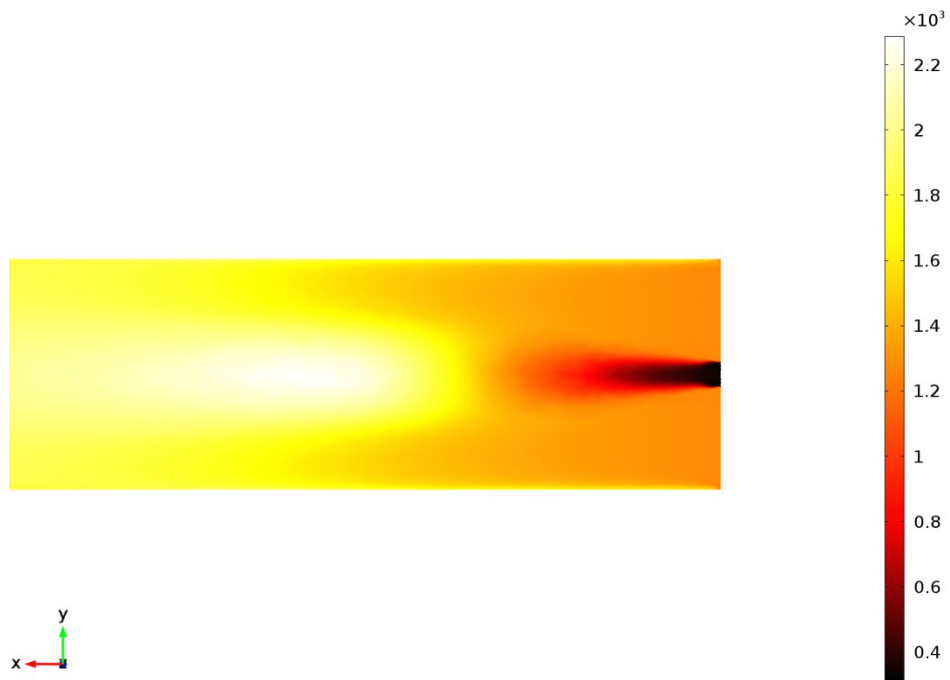
Figure 19. Temperature field (K) – burner area.
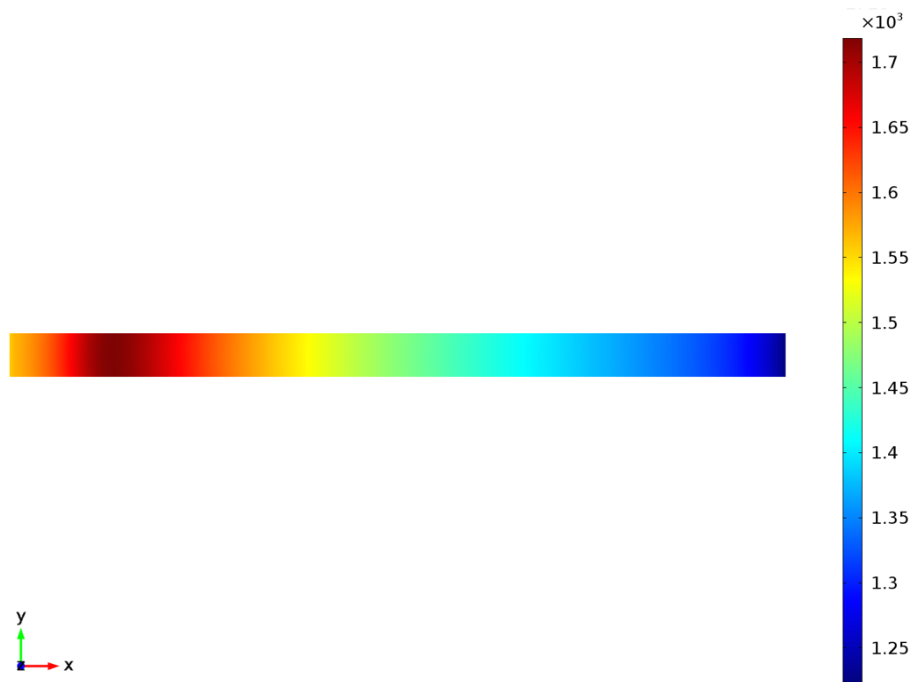
Figure 20. Temperature distribution of the solid material (K)
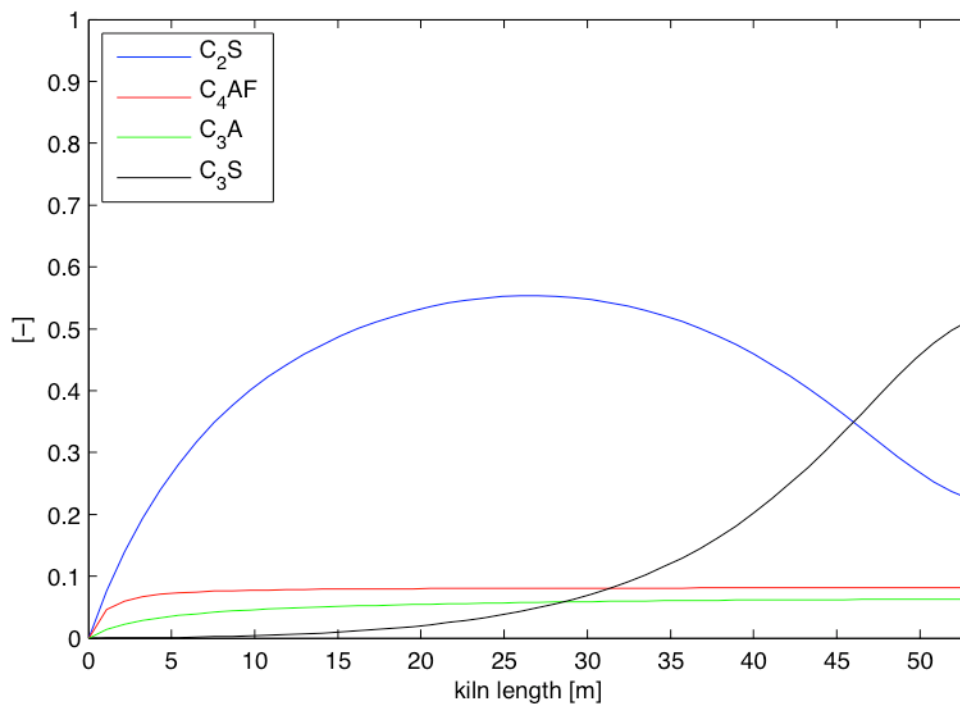
.
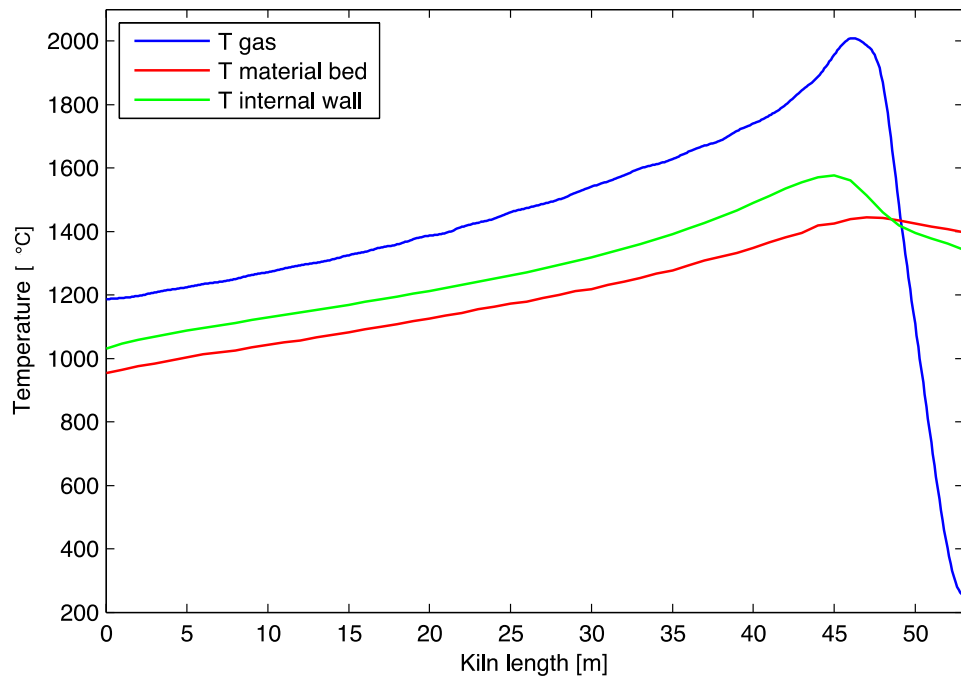
Figure 21. Temperature profiles.

Figure 22. Chemical profiles.

3.4.2 – Optimized lumped element model

Forecasts of a kiln's behavior are important in order to anticipate possible deviations from steady state operation under nominal conditions. Having a tool that is able to provide accurate predictions of the kiln's behavior in response to changes of certain operative parameters thus becomes extremely useful. For such reason the LEM performances on transient predictions were tested in several working conditions.

An example is reported in Figure 23, where the kiln response after increasing the fuel flow from 1.5 kg/s to 2.5 kg/s (the air flow has been proportionally increased also, to keep the same stoichiometric ratio) is shown on an observing period of 3600 s. Results show two effects: a) the first is a slight increase of the flame temperature, which passes from 1830 °C to 1901 °C; b) the second is a shift of the sintering zone, which moves towards the kiln inlet; it is therefore clear that the chemical reactions are anticipated. The maximum temperature of the material increases from 1370 °C to 1535 °C; as a consequence, the chemical composition of clinker shows a reduction of non-reacted CaO to almost 0 %, whilst C3S passes from 28 % to 64 % and C2S content is reduced from 40 % to 13 %. It is worth noting the trend shown by the temperature of the gas exiting the kiln as the mass flows of both air and fuel increase. Considering the nominal flow rates characterizing the simulation reported in 3.3.3 and the flow rates of the present simulation, which are across the nominal ones, it can be noted that the temperature of the exiting gases progressively increases by passing from 1152 to 1317 °C. This phenomenon indicates a reduction of the heat exchange efficiency between the

41

freeboard gas and the material bed, thus resulting in a worsening of the energy performances of the process.
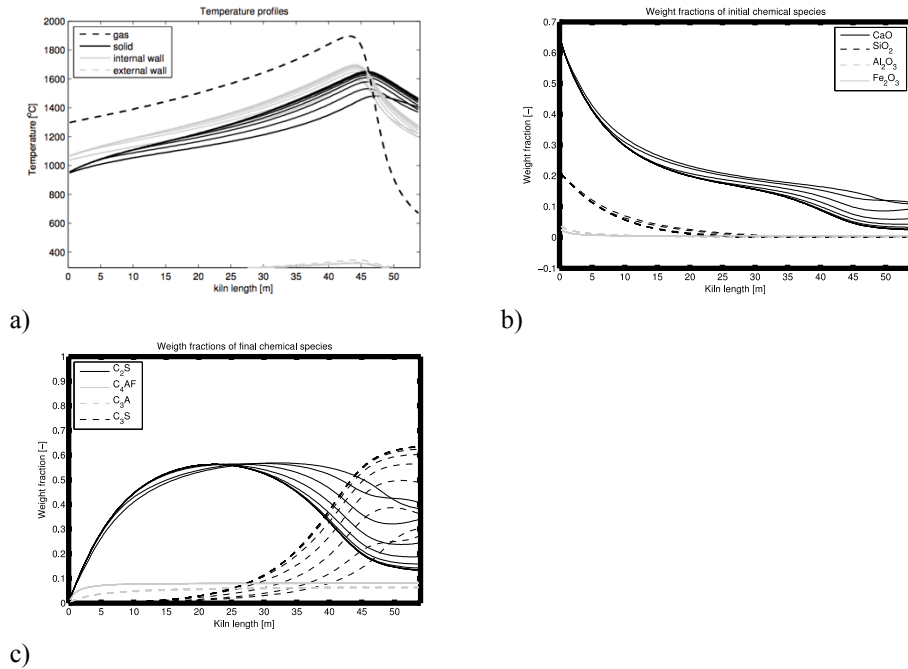

a)

b)

c)

Figure 23. Step response after increasing the fuel flow.

Figure 24 shows the kiln response after a reduction of the mass flow of raw meal (from 140 to 112 T/h), during a 3600 s simulation period. The material increases its temperature up to 1600 °C and therefore the weight fraction of C3S in clinker increases up to 69 %, whilst C2S and unreacted CaO are reduced to respectively 10 % and 0 %. Unlike the previous simulation, this time the sintering zone does not move.

The next simulation considers a more drastic reduction of mass flow respect to the previous case (from 140 to 90 T/h). Kiln response on a 3600 s period is shown in Figure 25. The maximum temperature of the material rises up to 1680 °C. As a consequence, unreacted CaO is reduced to almost 0 %, whilst final mass fractions of C2S and C3S become 8 % and 71 % respectively.

In Figure 26 the same reduction of mass flow is compensated by adjusting the rotating speed of the kiln (from 4 to 3.2 rpm) so the retention time remains unchanged (20 min); also fuel and air flows are proportionally reduced. It can be noted that the temperature profile of the material is maintained quite constant during the whole transient period, until the new steady state is reached. Therefore, also chemical profiles remain almost unchanged.

The next two simulations are steady analyses where the gas emissivity ε_g and the gas-solid convective heat exchange coefficient are changed. Figure 27 shows the effect of an increase of the convective heat exchange by a factor of ten. Increasing the convective heat exchange improves the overall efficiency of the kiln: this is clear when observing the temperature of

the exiting gases, which decreases from 1245 to 1143 °C. The maximum temperature of the material increases up to 1664 °C. Also the chemical composition of clinker changes: unreacted CaO is reduced to about 0 %, whilst the weight percentages of C3S and C2S become 69 % and 9 % respectively. Figure 28 shows results of a simulation run after reducing the gas emissivity from 0.2 to 0.05. Again, a reduction of the gas emissivity entails a worsening of the kiln efficiency, so the temperature of the exiting gases increases up to 1358 °C. The maximum temperature of the material bed decreases to 1342 °C. The weight percentages of C3S and C2S become respectively 31 % and 37 %. Changing the emissivity is more incident in the sintering zone of the kiln, where the gas temperature is much higher than in the other areas.

a)

b)

c)
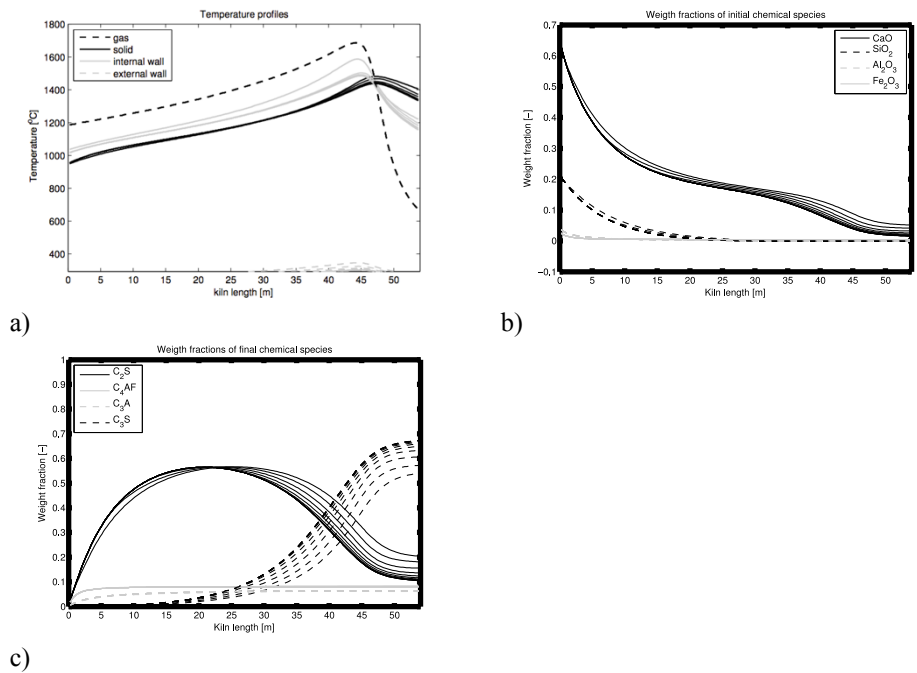
Figure 24. Step response after reducing the mass flow of raw meal to 112 T/h.
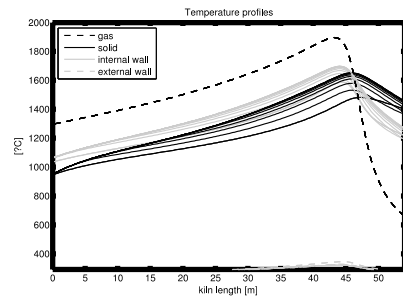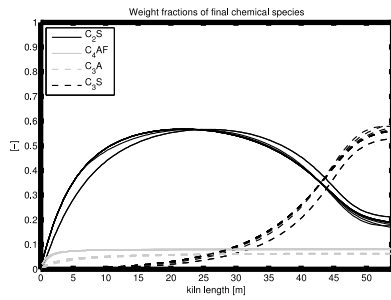
a)
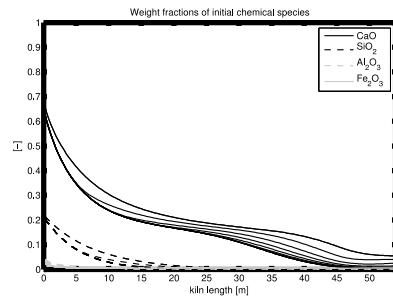
b)
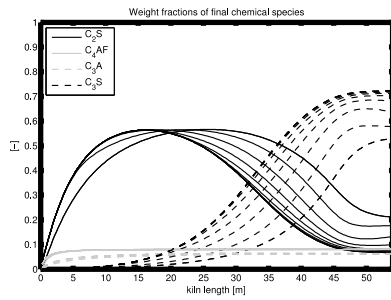
c)

Figure 25. Step response after reducing the mass flow of raw meal to 90 T/h.
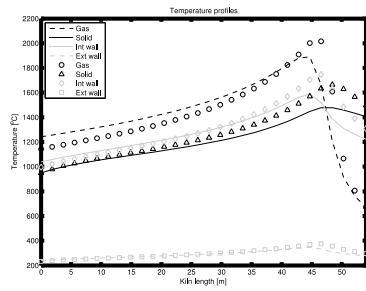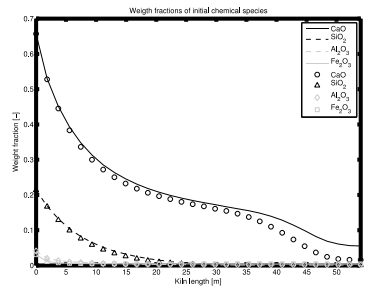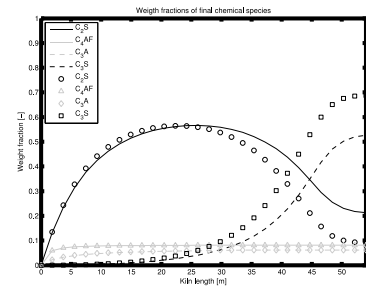
44
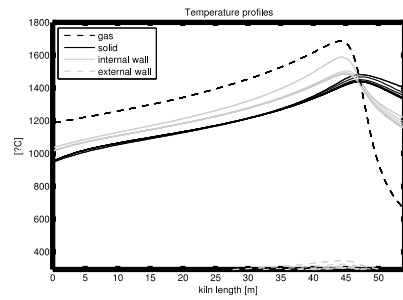
a)
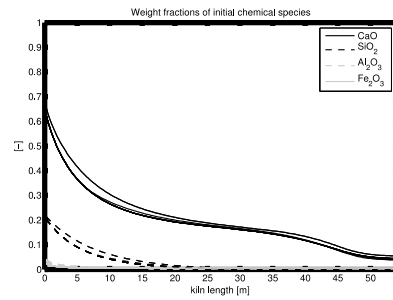
b)

c)

Figure 26. Step response after reducing the mass flow of raw meal to 90 T/h. Rot. Speed and fuel flow are adjusted
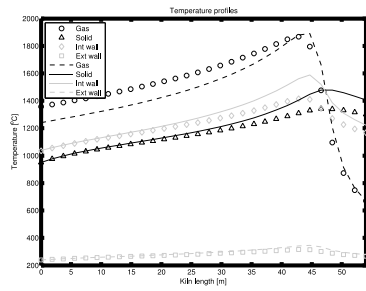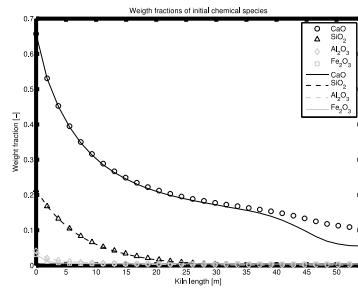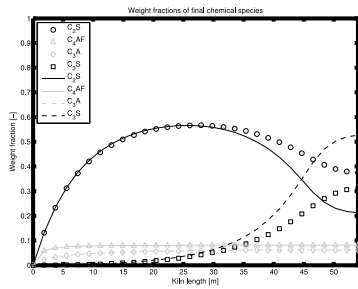
.

a)

b)

c)

Figure 27. Convective heat exchange – lines are for section 3.3.3 prediction, dots for increased value.

a)

b)

c)

Figure 28. Emissivity – lines are for section 3.3.3 prediction, dots for reduced value.

Section 4 – Estimation of the uncertainty of the soft sensor

This section addresses the problem of the estimation of uncertainty of the virtual sensor. Estimation of the accuracy is conduced according to the method discussed in section 1.4. The section is organized as follows: a) in subsection 5.1 the propagations of the input uncertainties through the lumped element model are estimated according to the guidelines reported in the GUM [53]; b) subsection 5.2 introduces the XDEM framework, i.e. a Lagrangian approach that allows for an extremely accurate representation of material in powder state; c) subsection 5.3 discusses the application of XDEM to the prediction of the thermochemical phenomena involving the material bed of the kiln considered; d) subsection 5.4 presents the XDEM results. In particular, it is pointed out the capability of XDEM for providing accurate predictions of the "*in-plane*" segregation phenomena involving both thermal and chemical variables, which are neglected in the lumped model; e) in subsection 5.5 the results are elaborated in order to get a quantitative estimation the uncertainty introduced by the lumped model.

4.1 – Propagation of the input uncertainties

The propagation of the input uncertainties was assessed following the guidelines reported in the GUM [53]. The maximum temperature of the material T_{max} was considered as the output of the instrument (indicated with y in the following in order to be consistent with the GUM notation); the choice was justified because of the great impact this variable has on the quality of the final clinker product.

A mono-variant sensitivity analysis has been performed on the different inputs of the LEM: a normal probability distribution (standard deviation set equal to 3 % of the mean value) was associated to each test variable. The sensitivity analysis identified the inputs whose uncertainty affects the most the accuracy of the output, i.e.: a) the specific heat of the material bed; b) the fuel flow; c) the enthalpy of combustion of the fuel; d) the mass flow of the material bed. The correspondent uncertainties on y (u_y) are reported in Table 11.

Input	u_y
Enthalpy of combustion	36.4 °C
Fuel flow	36.1 °C
Specific heat	21.1 °C
Mass flow	12.0 °C

Table 11. Mono-variant sensitivity analysis.

These parameters have been assumed as the variables to be considered in Monte Carlo simulations aimed at assessing the uncertainty associated to y. The adaptive procedure reported in Appendix A.1 was adopted, which considers carrying out an increasing number of Monte Carlo trials until the result of interest has stabilized in a statistical sense. Figure 29 shows the standard deviations s associated with y_{est}, u_y, y_{low} and y_{high} (respectively, the estimate of y, the associated uncertainty and the left- and right-hand endpoints of the coverage interval) whilst Monte Carlo iterations are proceeding.
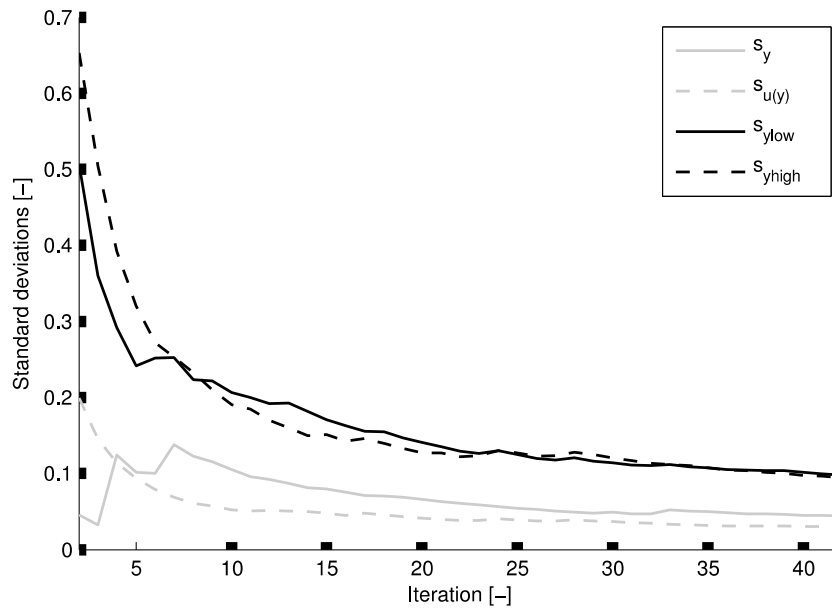

Figure 29. Standard deviations vs. iterations.

Four Monte Carlo simulations have been run using the different input distributions reported in Table 00, where the final uncertainties associated to y are also reported. Results show a linear propagation of the uncertainty through the model.

	u/μ of input parameters	u_y
MC 1	3.3 %	61.7 °C
MC 2	1.65 %	31.0 °C
MC 3	0.825 %	15.5 °C
MC 4	0.4125 %	7.8 °C

Table 12. MC simulations.

4.2 – Extended Discrete Element Method

XDEM is a numerical framework, where a DEM approach is exploited for resolving particles dynamics and heat exchanges between particles, whilst a Eulerian approach based on CFD equations is used for representing the fluid domain. One-dimensional models provide a description of the heat and mass transports inside each particle. Coupling between DEM and CFD is achieved by introducing heat and mass transfers at the fluid-particles interfaces. Besides, Darcy's law accounts for the pressure drop of the fluid while passing through the particles. Indeed, the integrated DEM-CFD environment allows for addressing numerous challenges in engineering, e.g. drug production, agriculture and food processing industries, mining, construction and agriculture machinery, metal manufacturing, energy production and system biology. XDEM has already been applied to the prediction of thermochemical phenomena involved in different industrial processes [88][89][90][91], where it is stressed the excellent agreement of the prediction of $CaCO_3$ decomposition under non-steady thermal conditions [92].

This section provides a description of the XDEM framework. The DEM approach handling the powder phase is presented at first, followed by a description of the CFD approach managing the fluid domain. The coupling of DEM with the CFD approach is discussed at last.

4.2.1 – DEM approach for the powder phase

4.2.1.1 – Particles dynamics

In XDEM the trajectory of each particle i is calculated deterministically by applying Newton's law of motion, as indicated as follows:

$$\frac{d(m_i \cdot \vec{v}_i)}{dt} = \vec{F}_i \tag{35}$$

$$\frac{d(I_i \cdot \vec{\omega}_i)}{dt} = \vec{M}_i \tag{36}$$

Where m_i, I_i, v_i and ω_i are the mass, the moment of inertia, the velocity and the angular velocity of the particle i, respectively. F_i is the resultant of the forces and M_i is the resultant of the moments of forces.

In general, a particle is subject to volume forces (electromagnetic, electrostatic, gravitational, etc.) and contact forces due to the mechanical interaction with its neighbors or boundaries. Equation 37 reports the expression of the normal component f_n of the contact force; the shear component $f\tau$ is expressed by eq. 38.

$$f_{n,ij,t} = K_n \cdot \delta_{n,ij,t}^{3/2} \tag{37}$$

$$f_{\tau,ij,t} = f_{\tau,ij,t-1} + K_\tau \cdot \left(\delta_{\tau,ij,t} - \delta_{\tau,ij,t-1} \right) \tag{38}$$

In both, eq. 37 and eq. 38, i and j are the indices of two particles in contact, δ_n and $\delta\tau$ are the normal and the tangential overlaps, respectively, t refers to the time step. K_n and $K\tau$ are calculated according to the Hertz and Coulomb models, respectively.

Equation 35 and eq. 36 are integrated in the time domain; then the positions of the particles are updated. A proper evaluation of the contact forces requires an extremely high time resolution. Therefore, also simulations over a short time period generally require an extremely high number of integration steps. The intrinsic heaviness of this kind of processing becomes more relevant as the number of particles increases. Simplifications like periodic or symmetric boundaries can be assumed for limiting the total number of particles involved in a simulation. Nevertheless, the optimization of the algorithms employed for neighbors' detection and for time integration should be a mandatory issue.

4.2.1.2 – Conductive and radiative heat exchanges between the particles

In XDEM each particle i exchanges heat with every other particle j and/or boundaries that are comprised inside the respective cutoff distances for conduction and radiation. Conductive and radiative heat exchanges are calculated according to

$$\dot{q}_{i,cond} = \sum_{j=1}^{N} \frac{1}{\frac{1}{\lambda_i} + \frac{1}{\lambda_j}} \cdot \frac{T_i - T_j}{\Delta x_{ij}} \tag{39}$$

$$\dot{q}_{i,rad} = \sum_{j=1}^{M} V_{(i \to j)} \cdot \sigma \cdot \left(T_i^4 - T_j^4 \right) \tag{40}$$

where N and M are the total number of particles comprised inside the cutoff distances for conduction and radiation, respectively; σ is the Stefan-Boltzmann constant; $V_{(i \to j)}$ is the reciprocal view factor and Δx_{ij} the distance between the particles i and j; λ is the thermal conductivity.

4.2.1.3 – Heat and mass transport inside the particles

XDEM considers a particle as composed by solid, liquid and gaseous phases. The particle is assumed in thermal equilibrium: this means the different phases have the same temperature distribution. This assumption is based on the assessment of the ratio of heat transfer by conduction to the rate of heat transfer by convection expressed by the Peclet number, as described in [93] and [94]. Heat and mass transports along the radial direction of the particle

are described by a set of one-dimensional and transient differential equations for conservation of chemical species, momentum and energy, as well as the state equations.

Equation 41 expresses the mass conservation of a solid or liquid specie i; the mass conservation of a gaseous specie is reported in eq. 42. In eq. 41 and eq. 42 $\Omega_{k,i}$ is the production or consumption rate consequent to the chemical conversion k.

$$\frac{\partial \rho_i}{\partial t} = \sum_k M_i \cdot \Omega_{k,i} \tag{41}$$

$$\frac{\partial \epsilon_p \cdot \rho_i}{\partial t} + \frac{1}{r} \frac{\partial}{\partial r} (r \cdot \rho_i \cdot u_g) = \frac{1}{r} \frac{\partial}{\partial r} \left(D_i \cdot \epsilon_p \cdot \frac{\partial \rho_i}{\partial r} \right) + \epsilon_p \cdot \sum_k M_i \cdot \Omega_{k,i} \tag{42}$$

The conservation of momentum of the gas phase is reported in eq. 43, and it is obtained by applying the Darcy's law:

$$-\frac{\partial \epsilon_p \cdot p_g}{\partial r} = \frac{\mu_g \cdot \epsilon_p}{K_p} \cdot |\vec{u}_g| \tag{43}$$

Where K_p identifies the so-called permeability coefficient, which characterizes the morphology of the porous particle.

The energy equation is based on the homogeneous model for a porous medium as described by Faghri [95] and written as reported in eq. 44, where λ_{eff} is the effective thermal conductivity, whose calculation is described in [93].

$$\frac{\partial (\rho_p \cdot c_p \cdot T_p)}{\partial t} = \frac{1}{r} \frac{\partial}{\partial r} \left(r \cdot \lambda_{eff} \cdot \frac{\partial T_p}{\partial r} \right) + \sum_k \Omega_k \cdot H_k \tag{44}$$

Finally, a prefect gas model for the gaseous phase is assumed. State equations are reported as follows, for sake of completeness:

$$p_g = \rho_g \cdot R_g \cdot T_p \tag{45}$$

$$h_g = c_g \cdot T_p \tag{46}$$

R_g is the specific gas constant, hg denotes the enthalpy.

The following boundary conditions are imposed to eq. 42 and eq. 44:

$$-\lambda_{eff} \left. \frac{\partial T_p}{\partial r} \right|_{r=0} = 0 \tag{47}$$

$$-D_i \left. \frac{\partial \rho_i}{\partial r} \right|_{r=0} = 0 \tag{48}$$

$$-\lambda_{eff} \left. \frac{\partial T_p}{\partial r} \right|_{r=R_p} = \dot{q}_{p,cond} + \dot{q}_{rad} + \alpha_p \cdot (T_p - T_f) \tag{49}$$

$$-D_i \left. \frac{\partial \rho_i}{\partial r} \right|_{r=R_p} = \beta_p \cdot (\rho_i - \rho_{f,i}) \tag{50}$$

Where R_p is the radius of the particle and α_p and β_p denote the heat and mass transfer coefficients between the particle and the CFD domain respectively. $Q_{p,cond}$ and $q_{p,rad}$ are the conductive and radiative heat exchanges with neighbors, and are calculated according to eq. 39 and eq. 40, respectively.

4.2.1.4 – Chemical conversions

The rate of a reaction Ω_k is expressed according to the molar concentrations C_i of the reactants and the rate constant K_k. The analytical expression of Ω_k is reported in eq. 51, while eq. 52 provides the temperature dependency of K_k.

$$\Omega_k = K_k \cdot \prod_i C_i \tag{51}$$

$$K_k = a \cdot exp\left(\frac{-E_a}{R_{gas} \cdot T_p}\right) \tag{52}$$

A is the pre-exponential factor, E_a is the activation energy and R_{gas} is the gas constant.

4.2.2 – CFD approach for the fluid domain

The fluid domain is solved using a model developed for flows through a porous media. A porous media is characterized by its porosity ε_b, i.e. the ratio between the void space and total volume of the media. The model provides a description of the flow where the variables are averaged on a coarser level, with respect to the sizes of the individual channels of the tortuous void space. To that purpose, a Representative Elementary Volume (REV), which respects the condition of eq. 53, is introduced.

$$L_f \ll L_{REV} \ll L \tag{53}$$

In eq. 53 L is the characteristic length of the problem, L_{REV} the linear dimension of the REV and L_f the length scale associated with void dimension. Variables of the fluid domain are averaged over the REV ($\langle\rangle$ symbol in the following equations).

Mass conservation for a specie i is reported in eq. 54, where $m_{f,i}$ is a source/sink term accounting for the mass transfer between the particles and the CFD domain.

$$\frac{\partial}{\partial t}\left(\epsilon_b \cdot \langle\rho_{f,i}\rangle\right) + \vec{\nabla} \cdot \left(\epsilon_b \cdot \langle\rho_{f,i}\rangle \cdot \langle\vec{u}_f\rangle\right) = \dot{m}_{f,i} \tag{54}$$

The conservation of momentum is based on Darcy's law, and writes:

$$\begin{aligned}
\frac{\partial}{\partial t}\left(\epsilon_b \cdot \langle\rho_f\rangle \cdot \langle\vec{u}_f\rangle\right) &+ \vec{\nabla} \cdot \left(\epsilon_b \cdot \langle\rho_f\rangle \cdot \langle\vec{u}_f \otimes \vec{u}_f\rangle\right) \\
&= \vec{\nabla} \cdot \left(\epsilon_b \cdot \langle\vec{\tau}_f\rangle\right) - \frac{\mu_f}{K_{bed}} \cdot \epsilon_f^2 \cdot \langle\vec{u}\rangle - C_{bed} \cdot \langle\rho_f\rangle \cdot \epsilon_b^3 \cdot \left|\langle\vec{u}_f\rangle\right| \\
&\quad \cdot \langle\vec{u}_f\rangle
\end{aligned} \tag{55}$$

Where K_{bed} and C_{bed} are calculated according to the characteristics of the packed bed, more details are reported in [92].

The energy conservation is reported hereafter, where q_f is a source/sink term accounting for the heat transfer between the particles and the CFD domain.

$$\begin{aligned}
\frac{\partial}{\partial t}\left(\epsilon_b \cdot \langle\rho_f\rangle \cdot \langle h_f\rangle\right) &+ \vec{\nabla} \cdot \left(\epsilon_b \cdot \langle\rho_f\rangle \cdot \langle\vec{u}_f \cdot h_f\rangle\right) \\
&= \vec{\nabla} \cdot (\vec{q}'') + \frac{\partial p_f}{\partial t} + \langle\vec{u}_f\rangle \cdot \nabla\langle p_f\rangle + \dot{q}_f
\end{aligned} \tag{56}$$

Equation 57 and eq. 58, which are valid under the perfect gas assumption, complete the mathematical model.

$$\langle p_f\rangle = \langle\rho_f\rangle \cdot R_g \cdot \langle T_f\rangle \tag{57}$$

$$\langle h_f\rangle = c_f \cdot \langle T_f\rangle \tag{58}$$

4.2.3 – DEM-CFD coupling

XDEM performs a time-domain integration of the aforementioned equations: in particular, at each time step the positions of the particles are updated using the dynamics module; subsequently, the porosity of the bed is calculated; finally, heat and mass exchanges between the CFD domain and the particles are calculated according to:

$$\dot{q}_f = \sum_{j=1}^{N} \langle \frac{A_j}{V_{REV}} \cdot \alpha \cdot (T_j - T_f) \rangle \tag{59}$$

$$\dot{m}_{f,i} = \sum_{j=1}^{N} \langle \frac{A_j}{V_{REV}} \cdot \beta_i \cdot (\rho_{j,i} - \rho_{f,i}) \rangle \tag{60}$$

Where N is the total number of particles inside the REV; A_j is the surface area of the particle j. V_{REV} is the volume of the REV, α and β_i are the heat and mass transfer coefficients between the CFD domain and the particle j. The transfer coefficients are calculated according to the Nusselt, Reynolds and Sherwood numbers of the fluid domain, as stated as follows:

$$\alpha = Nu \cdot \frac{\lambda_f}{D_p} \tag{61}$$

$$\beta_i = Sh \cdot \frac{D_i}{D_p} \tag{62}$$

Where the diameter of each particle is represented by the D_p term.
Heat and mass transfers are represented by source/sink terms in the Navier-Stokes equations, whilst for each particle they provide the boundary conditions for the one-dimensional heat and mass transport equations.

4.3 – XDEM model

The XDEM framework was exploited for a comprehensive simulation involving the particles constituting the material bed of the real kiln. During their transit through the kiln, these particles undergo thermal exchanges with both the rotating wall and the counter-current gas flow. The heat redistribution inside the material bed is deeply affected by the material powder state, in particular by the in-plane recirculation impressed by the rotating wall. Temperature of the particles drives their chemical conversion, until the final clinker is obtained. Table 7 summarizes the reactions considered in the present study with their kinetic parameters and enthalpies obtained from [80].

In order to make the problem addressable from a computation point of view, two periodic boundaries orthogonal to the axis of the kiln, spaced of 0.4 m, have been introduced. The simulation domain consists of the thin slice comprised between the two planes, and it is shown in Figure 30. A total of 4000 particles have been introduced, providing the filling level indicated. The particles movement within the yz-plane, which is impressed by the rotation of the wall, has been simulated using the dynamics module. The retention time has been ensured by assuming a particles speed of 0.045 m/s in the x direction. Adiabatic conditions have been imposed at the two periodic boundaries.
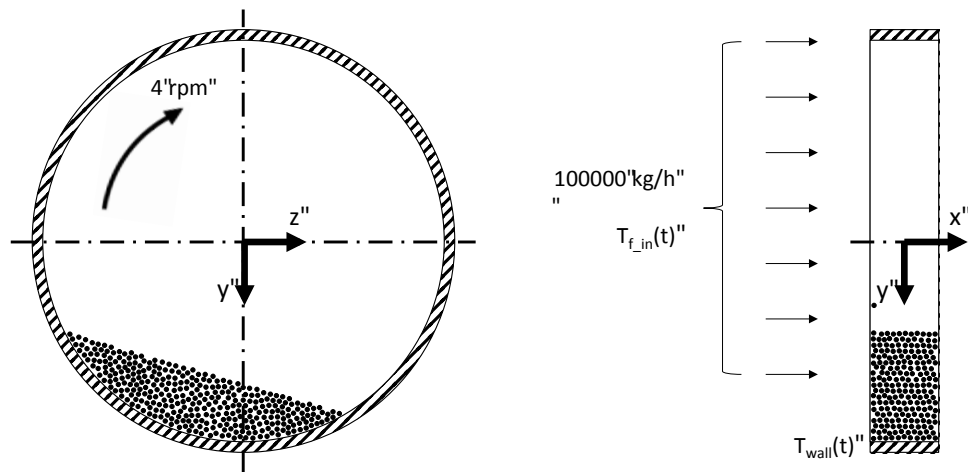
Figure 30. Simulation domain (particles are not in scale).

4.4 - Results

Figure 31 shows the velocity of each particle while the kiln is rotating, in a state of motion that can be assumed as steady. The rolling mode of the material bed is evident from the observation of Figure 31. Indeed, as typical to such kind of particles movement, two different zones can be identified: the passive region, where particles act almost as a rigid body following the rotation of the wall, with a speed that linearly decreases when moving towards the center; the active layer on the top, where particles slip over the free surface of the material bed. As a results of the velocity field, a continuous recirculation of the external particles takes place, whilst the internal particles tend to be trapped in the bulk zone of the material bed. The simulation can be compared with analytical models for a rolling mode-operated kiln, as the one discussed in [96]. When applying the model presented in [96] to the present case a thickness of the active layer of 0.16 m, and an average speed of the particles inside the active layer of 0.9 m/s are found. Results of the simulation performed using the XDEM framework (0.19 m for the thickness, 0.8 m/s for the average speed) are in good agreement with the analytical values.

CFD-DEM coupling is shown in Figure 32, which presents both the heat transfer (a) and the porosity (b) fields of the simulation domain.
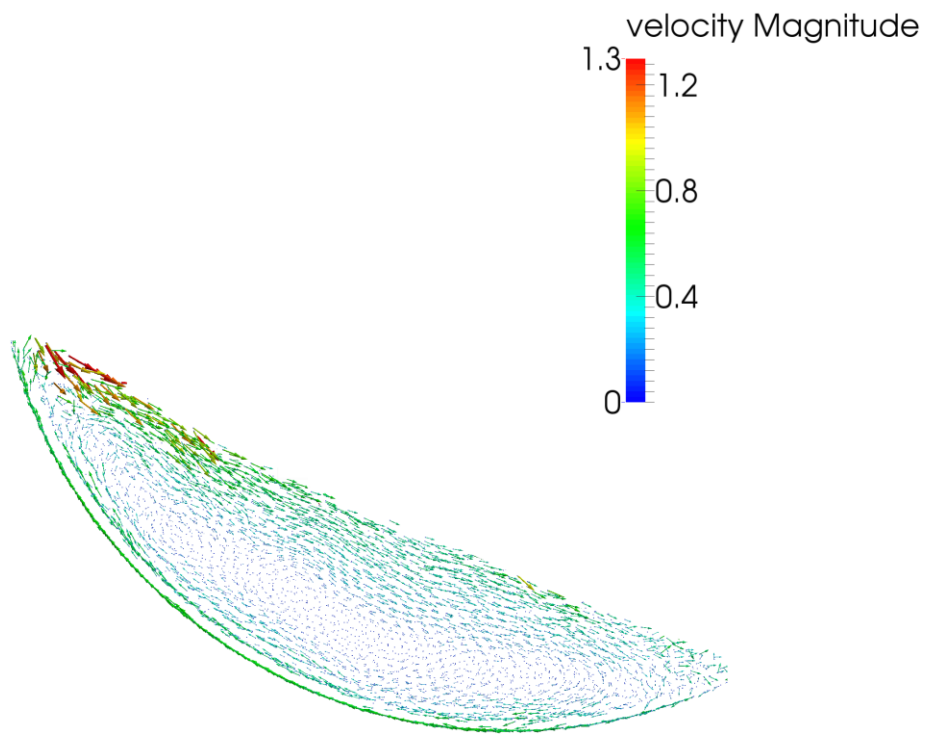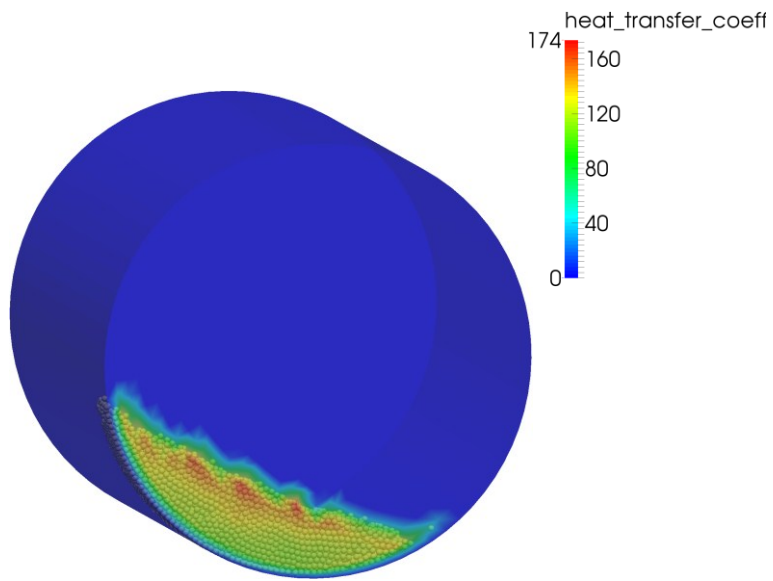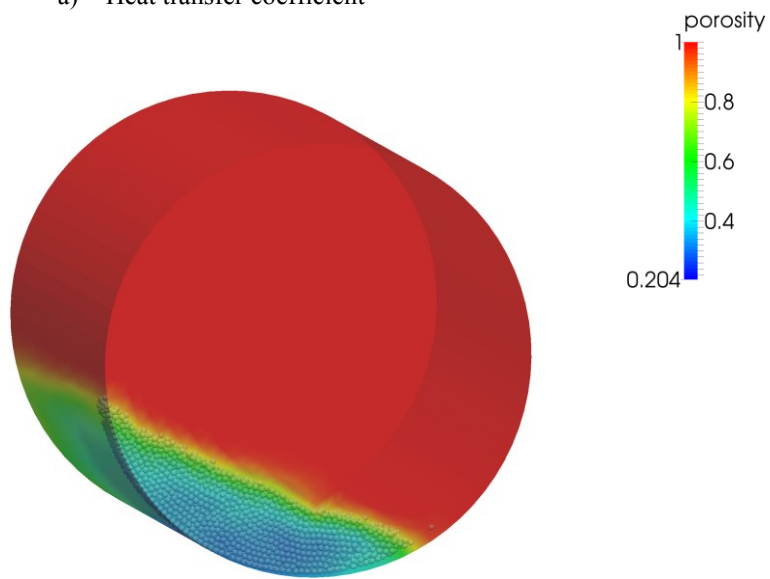
velocity Magnitude

1.3
1.2

0.8

0.4

0

Figure 31. Velocity field

.

heat_transfer_coeff
174
160
120
80
40
0

a) Heat transfer coefficient

porosity
1
0.8
0.6
0.4
0.204

b) Porosity

Figure 32. CFD-DEM coupling.

The thermochemical results of the simulation are presented in the next part of this section. Three simulation time frames, which correspond to different positions inside the kiln (Figure 33), are considered: 1 minute after the material enters the kiln; 10 minutes, which corresponds at the time instant when the material is almost at the middle length of the kiln; 20 minutes, i.e. when the material exits the kiln.
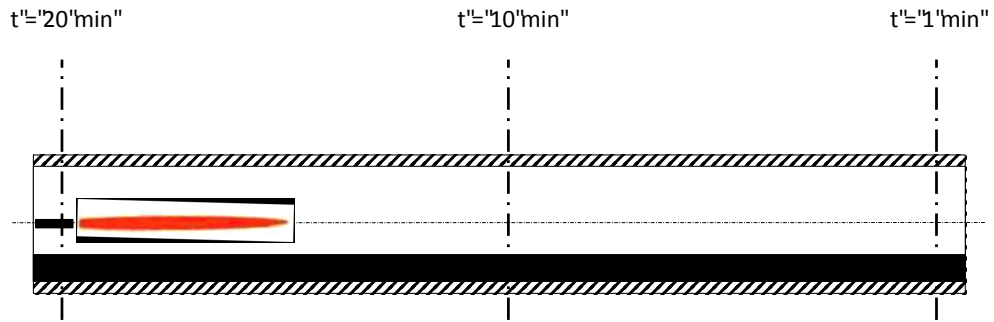
Figure 33. Positions vs. time.

Figure 34, Figure 35 and Figure 36 show the temperature distribution of the particles, on a yz analysis plane. At t=1 min the temperature is still close to the 1223 K initial value; at t=10 min the material reaches an average temperature of 1425 K; at t=20 min the average temperature is equal to 1687 K and is in good agreement with measurements from the production plant (1673 K). The effect of the velocity field is evident in the temperature distribution of the material bed. Particles on the top, which are directly exposed to the gas, show higher temperatures. The bulk particles (i.e. the particles trapped in the internal part of the material bed) are at lower temperature, because they get heat only by conduction from the outer particles.

Figure 37, Figure 38 and Figure 39 show the mass fraction of CaO on a yz analysis plane. CaO decomposition is accelerated in the outer particles, which are at higher temperature with respect to the others. Whilst at 1 minute the chemical composition is almost uniform, at 10 minutes a slight gradient inside the material bed is evident. Similarly, at 20 minutes some unreacted CaO is still present inside the bulk particles.

Figure 40 and Figure 41 show the spatial distributions at 20 minutes for C2S and C3S (i.e. the major components of the final clinker), respectively. Both species show specular distributions, with higher rates of conversion in the outer particles. Mean values (0.15 for C2S and 0.60 for C3S) are in good agreement with the typical clinker composition as reported in [54].
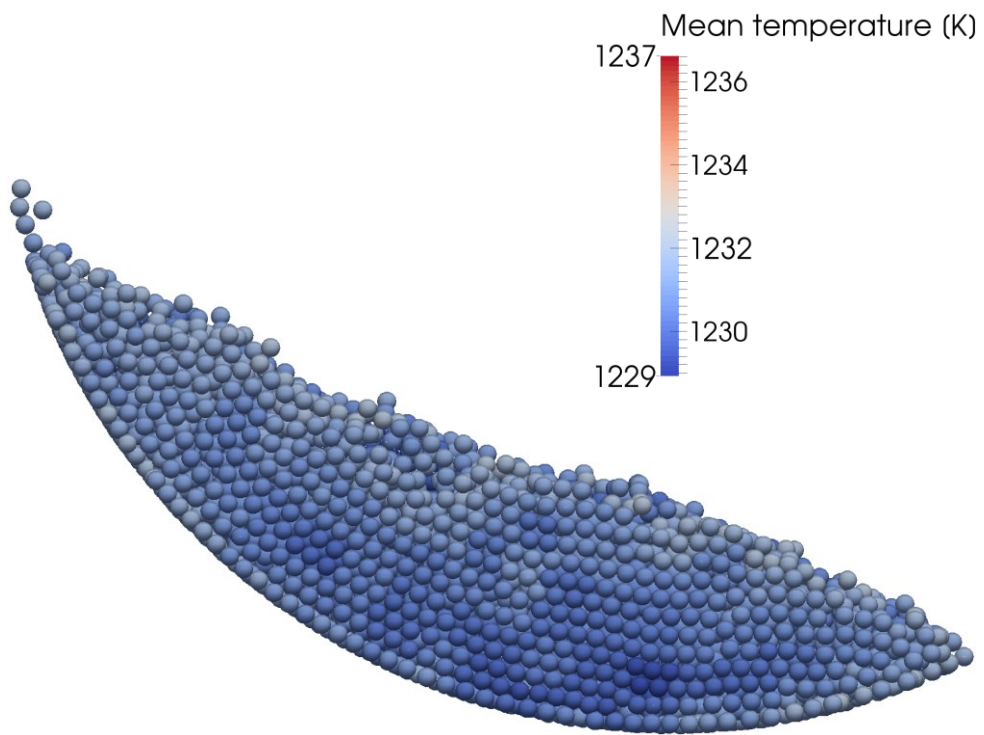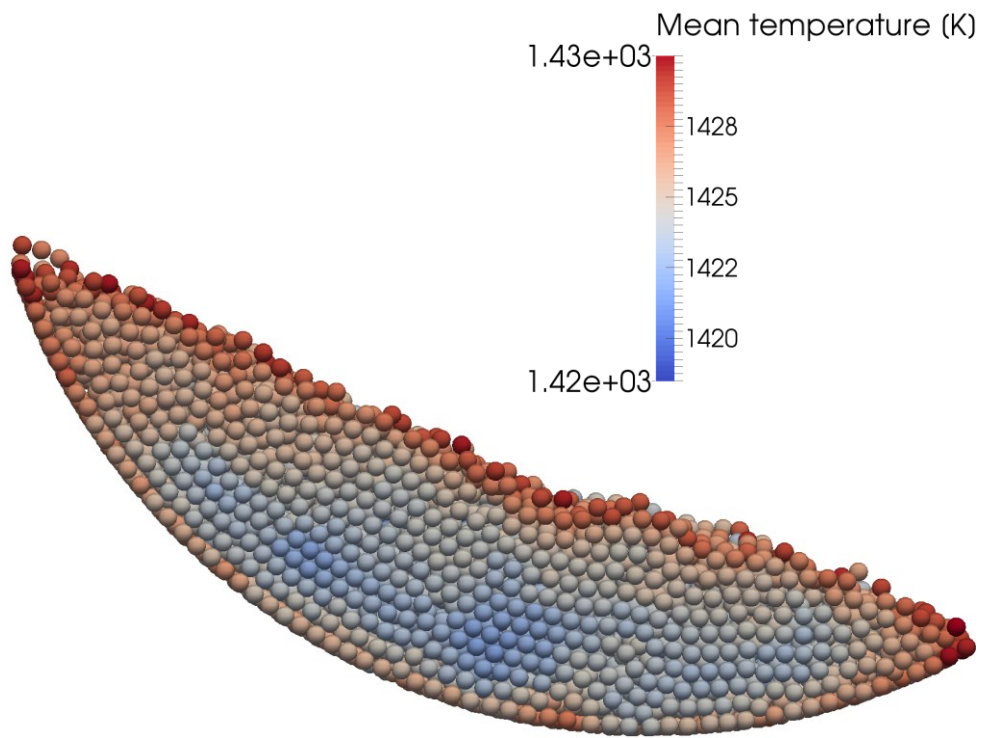
Figure 34. Temperature distribution – t=1 min.
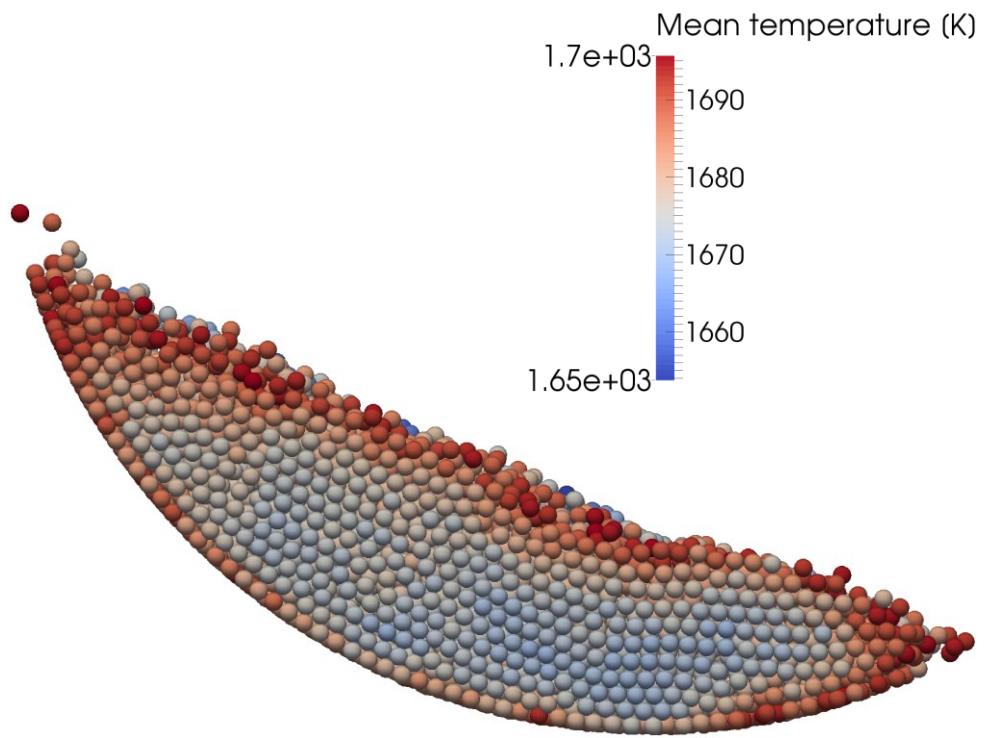
Figure 35. Temperature distribution – t=10 min.
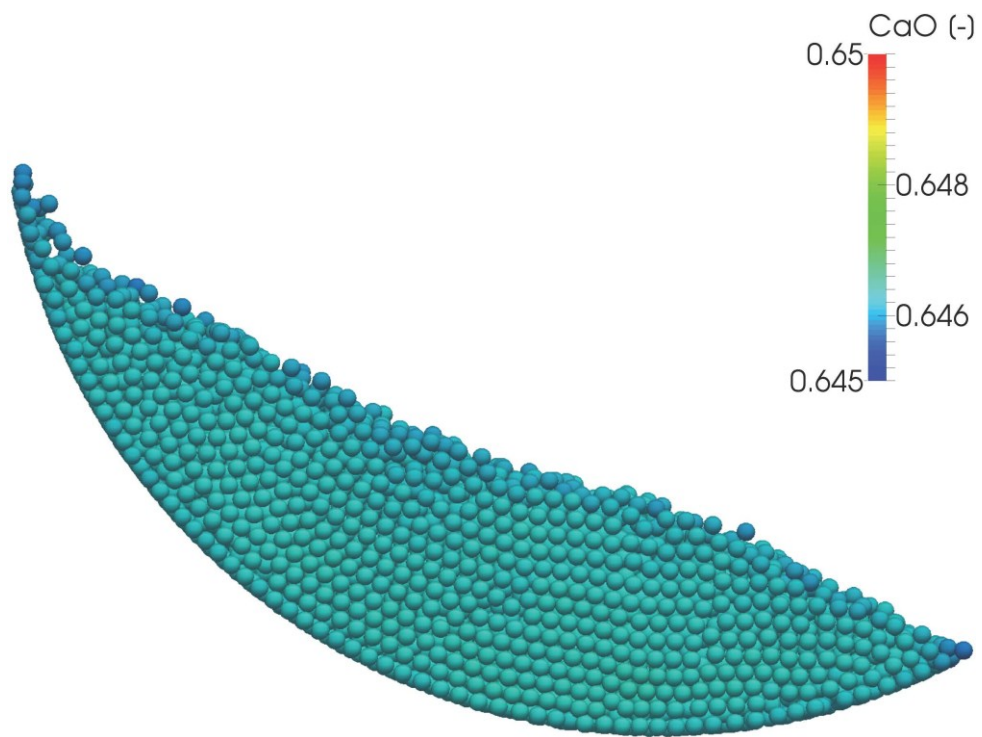
Figure 36. Temperature distribution – t=20 min.
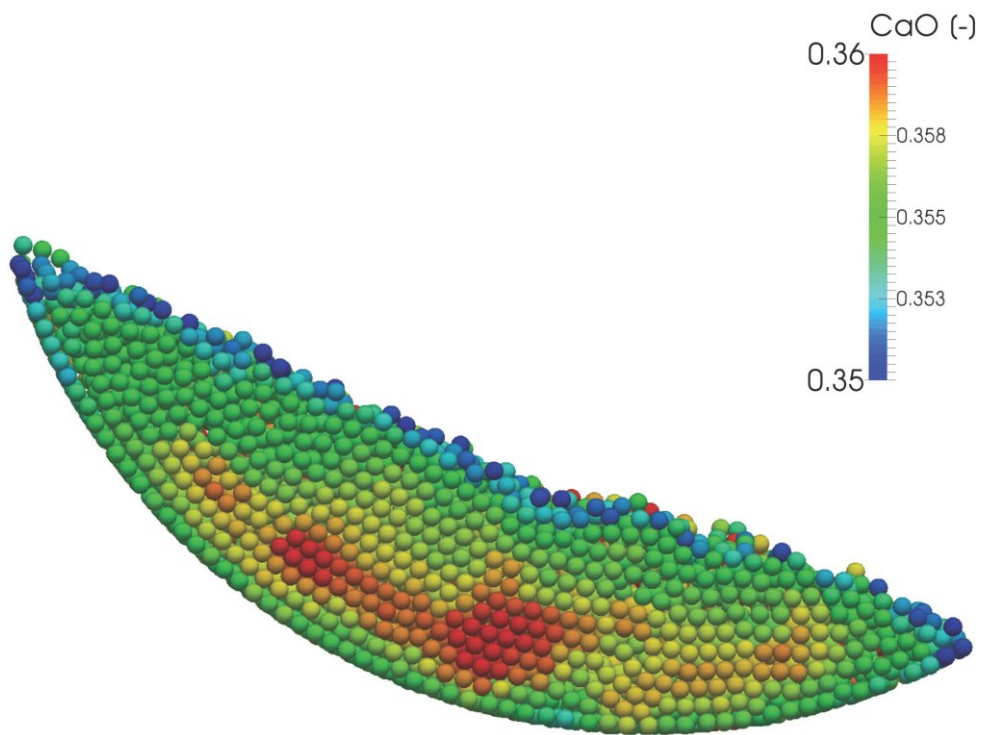
Figure 37. CaO distribution – t=1 min.

Figure 38. CaO distribution – t=10 min.

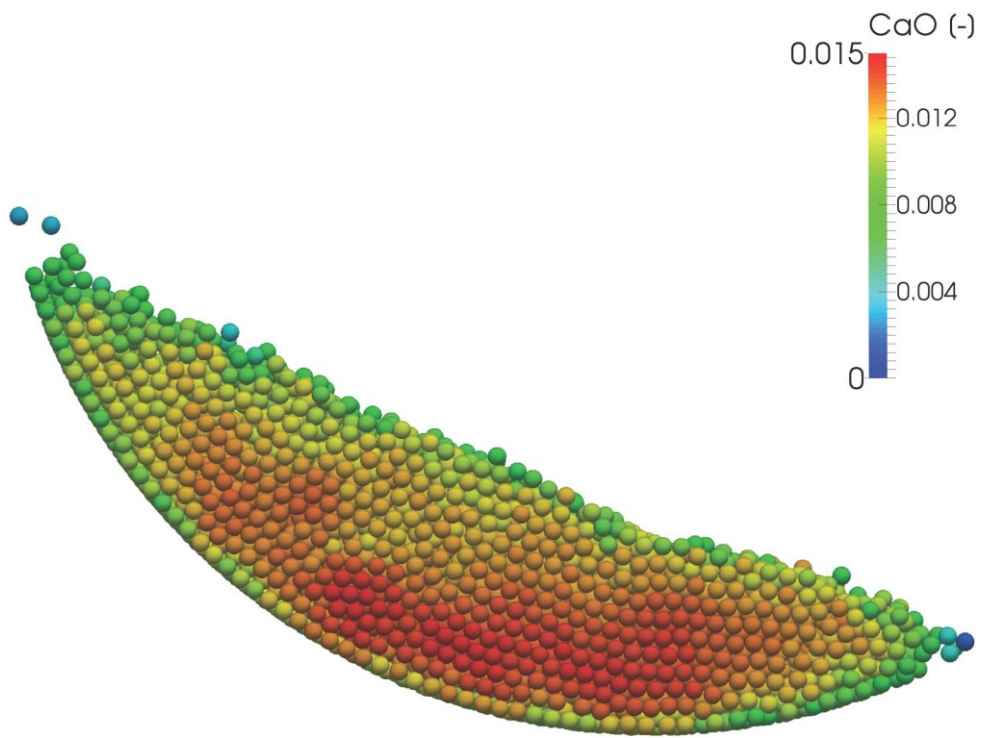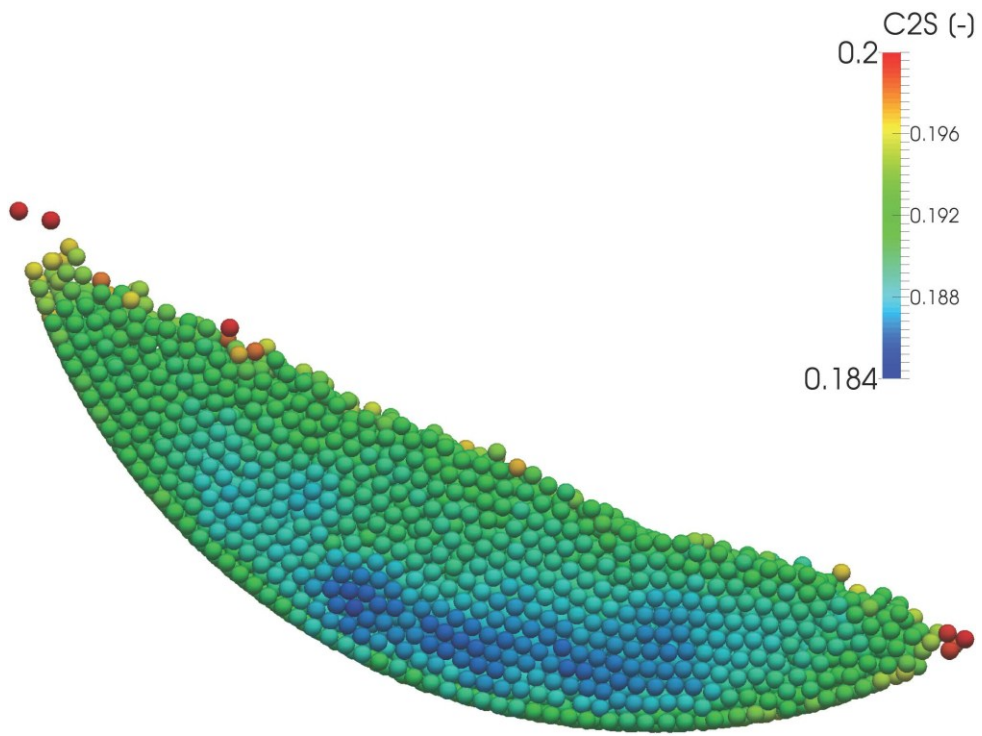*Figure 39. CaO distribution – t=20 min.*
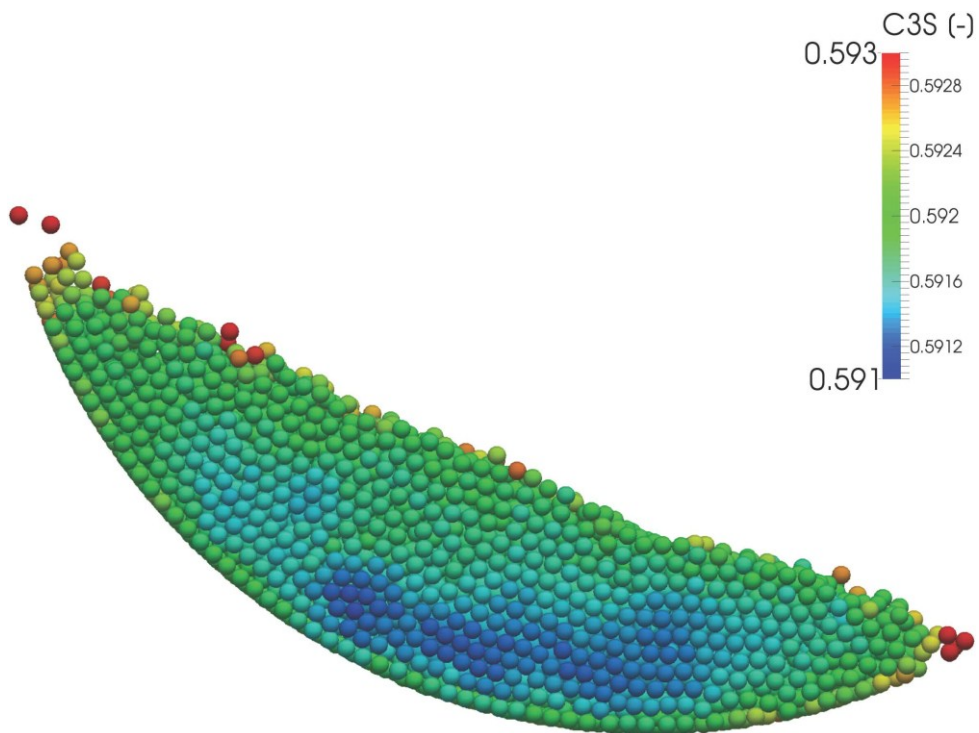
Figure 40. C2S distribution – t=20 min.

Figure 41. C3S distribution – t=20 m

4.5 – *Uncertainty introduced by the model*

Considering the XDEM results, it can be concluded that the major contribution to the uncertainty introduced by the lumped model is the missed representation of the *y-z* segregation phenomena: the LEM does not reproduce the *y-z* variance of its thermal and chemical variables. Nevertheless, this phenomenon is recognized as relevant for the quality of the finale product [97]; its quantification is fundamental, and the information should be integrated in the output of the soft sensor as a "*band of variance*".

To that scope, it is interesting to observe the probability distribution of the temperatures of the different particles in the XDEM results. Indeed, the standard deviation associated to every distribution gives an indication about the thermal homogeneity inside the material bed. The probability distributions at the three target times are presented in Figure 42. The standard deviation continuously increases from 0.96 K at 1 minute to 5.1 K at 20 minutes. In Figure 43 the trend of the standard deviation during the whole length of the retention time is integrated in the output of the soft sensor.

The lower-bound for the overall uncertainty of the soft sensor $u_{overall}$ can be calculated as the composition of the uncertainty propagated $u_{propagated}$ with the one introduced by the model u_{model}:

$$u_{overall} = \sqrt{u_{propagated}^2 + u_{model}^2} \qquad (63)$$
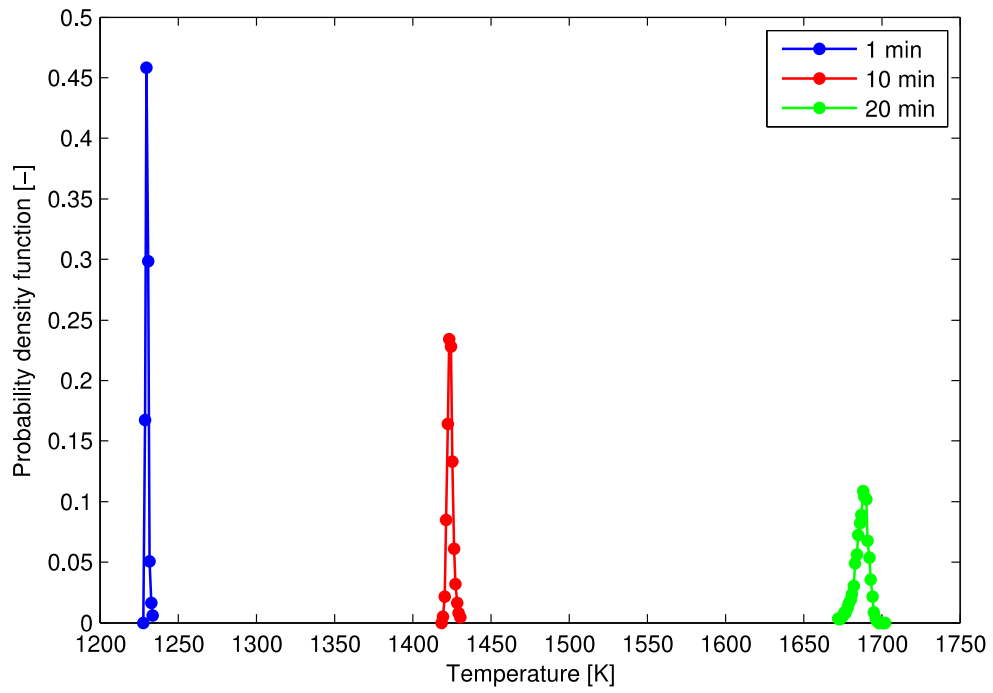

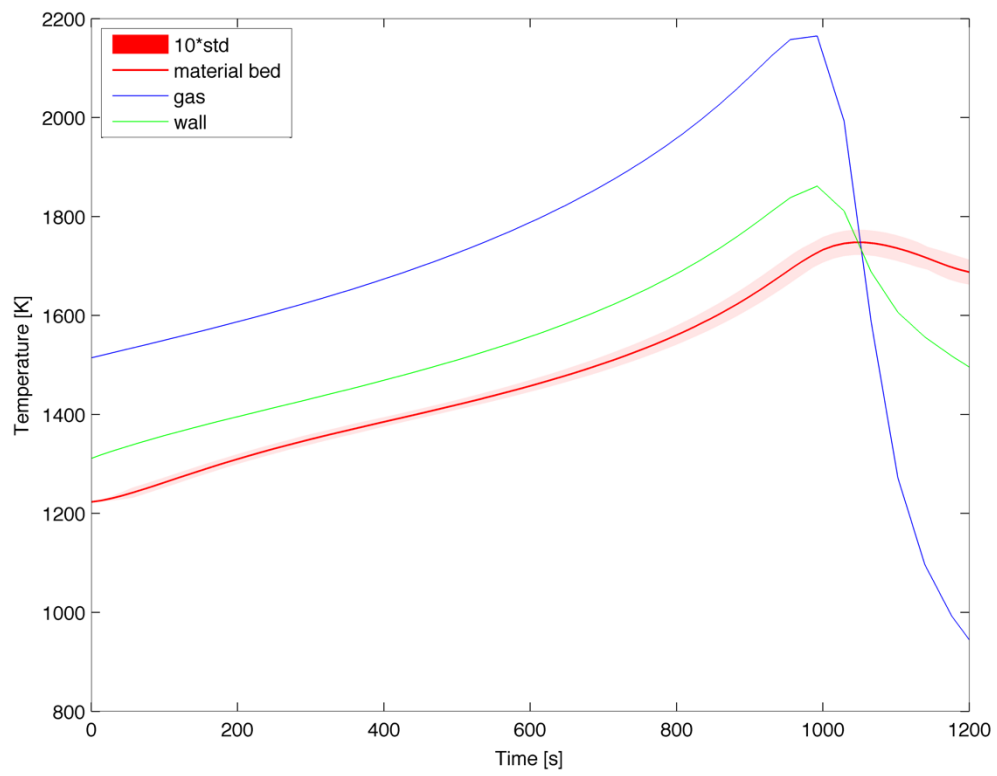*Figure 42. Probability distributions of temperature.*

Figure 43. Temperature vs. time.

Section 5 – Soft sensing for the new microwave heating stage

The new DAPhNE furnace suffers of the same critical issues of conventional kilns for what concerns process monitoring. In fact, the direct measurement of the thermal variables inside the microwave cavity is a tricky issue. Contact sensors would act as antennas if placed inside the strong electromagnetic field of the cavity. Nevertheless, an indirect estimation of thermal and chemical variables that characterize the processed material is fundamental if it is intended to operate the cavity according to optimization-oriented strategies with the constraint of respecting, or even enhancing, the quality targets of the final product.

Therefore, an indirect monitoring strategy has been developed for the new microwave-based heating stage, adopting a similar approach to the one referring to the conventional process. In the present case, the possibility of intervene in the design of the new monitoring architecture has been fully exploited for reducing the complexity of the theoretical model.

The dissertation is organized according to the following points: a) the monitoring architecture of the new DAPhNE module is described in subsection 5.1; b) the lumped element model supporting the soft sensor is introduced in subsection 5.2; c) subsection 5.3 discusses the input measurements of the soft sensor, with a particular focus over the infrared measurements for temperature monitoring; d) subsection 5.4 presents the outputs of the virtual sensor during one of the first tests of the demonstrator.

5.1 – Monitoring architecture of the new DAPhNE module

Figure 44 shows the monitoring architecture of the new DAPhNE module, which is responsible for providing a continuous assessment of different process variables. Field sensors provide 4-20 mA analog outputs, which are acquired by the PLC. On its turn, the PLC is connected via PROFINET to a field PC, which is responsible for: a) providing a Graphical User Interface (GUI); b) storing historical data into a database which is accessible by remote users. Also different stand-alone tools access the PLC, among which: a) the stand-alone tool for MW Control and Regulation, to be used for adjusting the resonant frequency of the cavity, in order to maximize the microwaves absorption and so the efficiency; b) the soft sensor for the indirect assessment of thermal and chemical variables of the material.
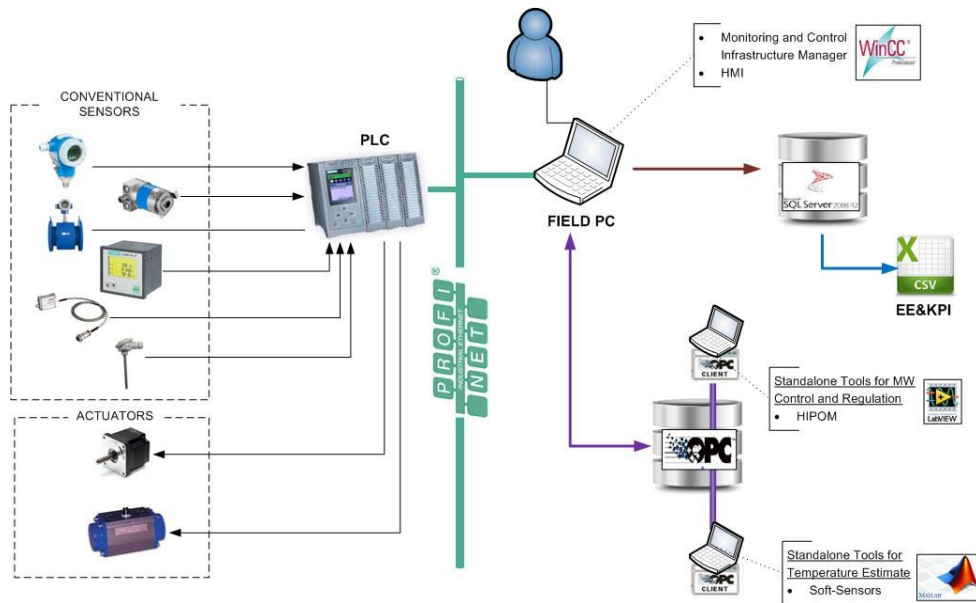
Figure 44. DAPhNE monitoring infrastructure.

5.2 – Lumped element model

Respect to the case discussed in section 3.3 the lumped model is more simplified:

1. It disappears the heat balance over the gas phase: here microwaves provide a bulk heating of the material. So no exothermic reactions inside the gas phase are involved. Moreover, the heat exchange of the material bed with the gas phase is considered as negligible, because no forced convection takes place inside the tube.
2. Temperature of the wall is not calculated from a heat balance, but it is directly measured on the external shell (subsection 4.3.3). Further, considering the small thickness of the tube, the temperature of the internal surface in direct contact with the material can be assumed as equal to that measured on the external shell.
3. Finally, the only chemical reaction considered is the $CaCO_3$ decomposition, because it is expected the material does not exceed the maximum temperature of 1000 °C. For this reason, the model includes only mass balances for $CaCO_3$ and CaO.

The mathematical system is reported in eqs. 64 – 66. Thermal conduction has been accounted on the heat equation. A full list of symbols is reported in Appendix A.5.

$$\rho_s c_s A_s \cdot \left(\frac{\partial T_s}{\partial t} + v_s \frac{\partial T_s}{\partial z} \right) = Q_c + P_A + h_{sw}(T_w - T_s) + A_s \cdot k \cdot \frac{\partial^2 T_s}{\partial z^2} \tag{64}$$

71

$$\frac{\partial C_{CaCO3}}{\partial t} = -v_s \frac{\partial C_{CaCO3}}{\partial z} - R_{CaCO3} \qquad (65)$$

$$\frac{\partial C_{CaO}}{\partial t} = -v_s \frac{\partial C_{CaO}}{\partial z} + \frac{M_{CaO}}{M_{CaCO3}} R_{CaCO3} \qquad (66)$$

P_A indicates the absorbed power; it is calculated from direct measurements made available from the field sensors (subsection 4.3). The h_{sw} coefficient has been calibrated thorough a comparison with a electromagnetic-thermal model developed by Istituto Superior Técnico (IST), on a 2.45 GHz resonant cavity. Resultant value that minimizes the difference between the two sets of predictions is 500 W/m^{2}K. Figure 45 shows the temperature profiles provided by the soft sensor and the IST model on the virtual cavity:
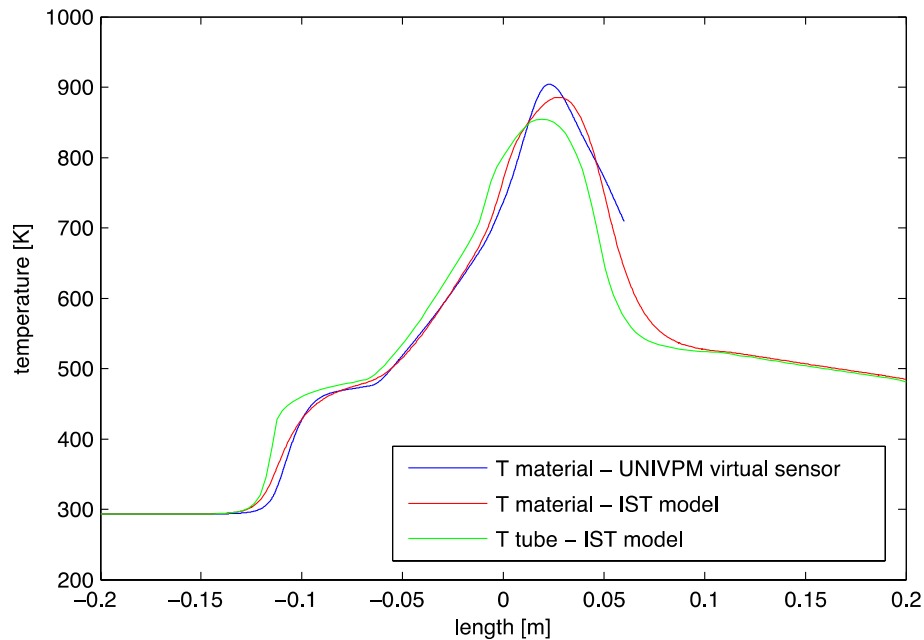
Figure 45. Calibration of the h$_{sw}$ coefficient using IST model as reference.

The soft sensor gathers real-time data from the PLC, through an OPC-server-client polling architecture. The following variables are acquired:
1. Temperature from infrared pyrometers pointing at the external surface of the tube. T_w is calculated as the average of the three measurements (subsection 4.3.3).
2. Temperature of the material at the inlet of the cavity, measured by a contact element. It constitutes the boundary condition $T_{s,in}$ for the heat balance equation.
3. Mass flow set on the feeder. It provides v_s.

72

4. Power generated P, from a power analyzer (subsection 4.3.1).
5. Power components P_a and P_b, from the HiPoM (subsection 4.3.2).

After being acquired, measurements are averaged on 60 s time period. Then the calculation routine provides a forecast of the transient behavior for the next 60 s. After that, measurements are updated. The final state constitutes the initial state for the next forecast.

The soft sensor is also equipped with a Graphical User Interface (GUI) developed to guide the operator in running a full test. The GUI consists in five main parts (see Figure 46):

1. *OPC client* section (cyan): by clicking on the "*Connect*" button the software connects to the OPC server, while pressing the "*Disconnect*" button disconnects the software from the OPC server;
2. *Test settings* section (green): the user can select if running a test on either metakaolin or clinker. Once selected the material, the user should press the "*Start test*" button in order to let OPC client-server communication and soft sensor run;
3. *Monitoring data* section (orange): the table shows time-averaged data collected from the OPC server.
4. *Plots* section (yellow): the two graphs show temperature of the material and $CaCO_3$ mass fraction along the tube.
5. *Communication* section (purple): the software gives to the user information regarding the status of the connection.
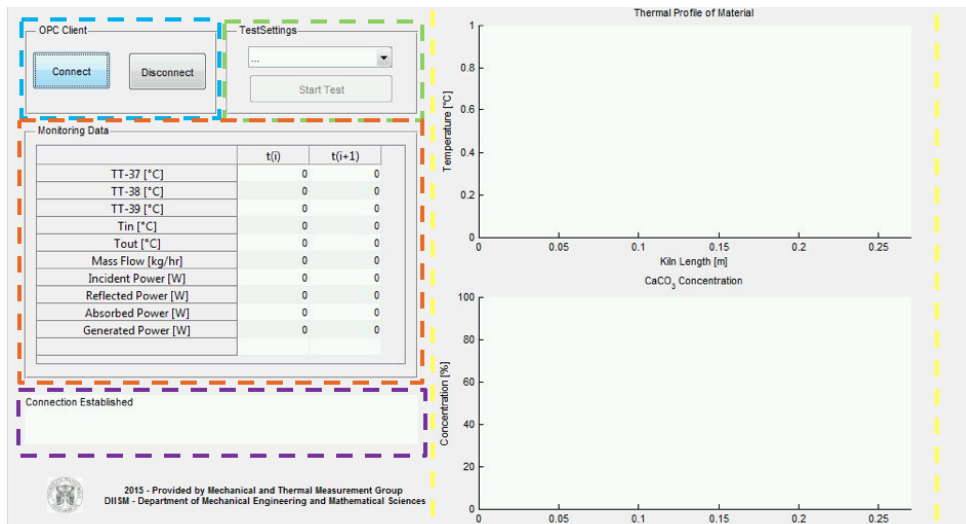

Figure 46. Graphical User Interface.

5.3 – *Input measurements*

Field sensors provide the soft sensor with direct measurements of the following variables: a) electrical absorbance, which is important also for evaluating Key Performance Indicators; b) temperature of the tube; c) absorbed and back-reflected fractions of the total incident power on the cavity: this measurement is made available by the Impedance Power Matching

73

(HiPoM) tool and it constitutes a fundamental input for the soft sensor. Each measurement will be addressed with more focus in the following subsections.

5.3.1 – Electrical absorbance

Several power analyzers provide continuous monitoring of the electrical consumptions of the microwave generator and the chiller, besides other auxiliaries. These variables are stored in a historical database. A dedicated tool accesses the database by remote, then calculates Key Performance Indicators for the process.

Electrical absorption of the microwave generator provides the instantaneous electromagnetic power sent to the cavity via the waveguide P.

5.3.2 – Absorbed and back-reflected power

The HiPoM is a tool developed by Università Politècnica de València; it provides continuous monitoring of the total incident P_t, absorbed P_a and back-reflected P_b power components (see Figure 47).
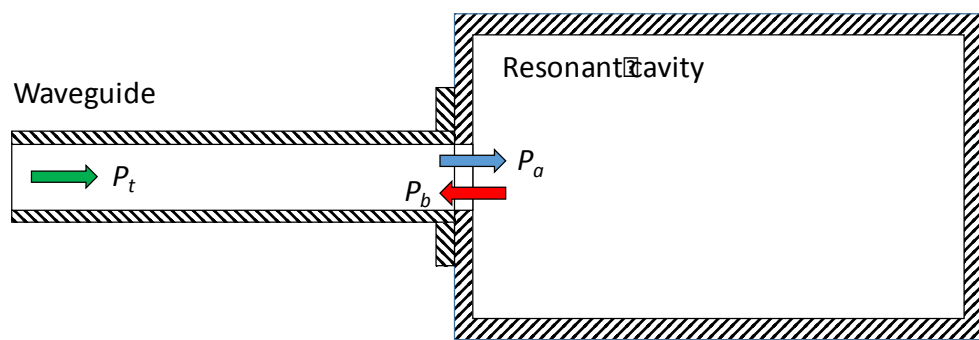
Figure 47. Incident, absorbed and back-reflected power components.

The accuracy of the device in assessing these quantities is unknown: as a consequence, readings provided for P_t, P_a and P_b may be inconsistent with the total power P indicated by the power analyzer. Nevertheless, the relative fractions of the absorbed and back-reflected powers respect to the total incident can be assumed as sufficiently accurate.

Therefore, data from HiPoM are processed together with measurements from the power analyzer. The quantities P_A and P_B are calculated according to eqs. 67 and 68, and they represent accurate estimations of the instantaneous power components absorbed and back-reflected from the cavity, respectively.

$$P_A = P \cdot \frac{P_a}{P_t} \tag{67}$$

74

$$P_B = P \cdot \frac{P_b}{P_t} \tag{68}$$

The trend of the fraction P_a/P_t during a typical operation of the cavity is reported in Figure 48:
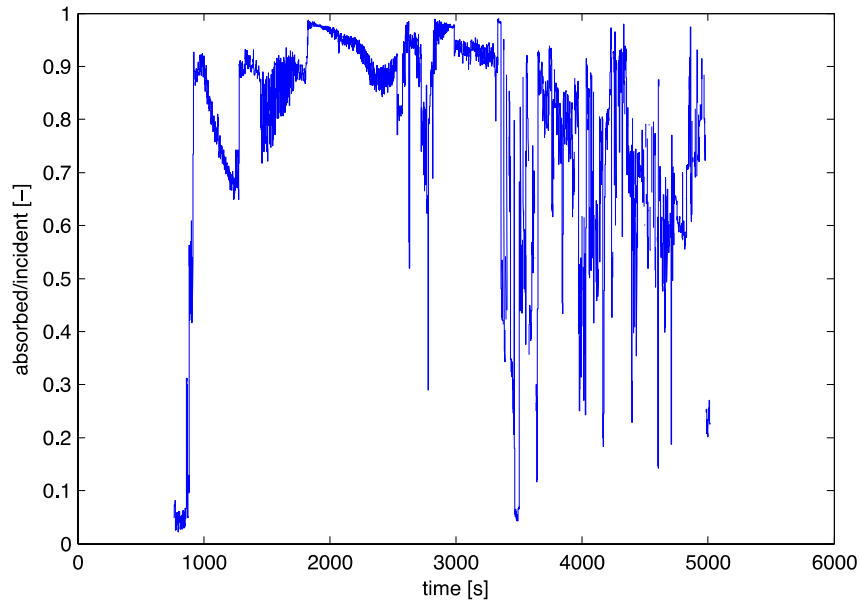

Figure 48. Absorbed to incident power ratio.

The efficiency of microwaves absorption is maintained high during the first period of operation, when a control action is undertaken. After, P_a decreases.

5.3.3 - Temperature

Thermal measurements inside the cavity are performed using three infrared pyrometers pointing at the external surface of the ceramic tube that contains the material. The measurement setup is shown in Figure 49:
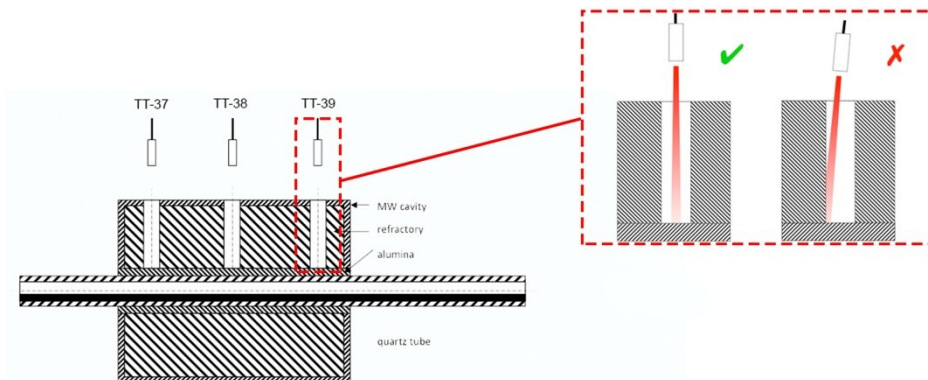
Figure 49. Measurement setup.

The optical accesses consist of three holes through the cavity wall and the insulating layer. Diameter of the holes is 10 mm: such value represents a compromise between the requirement for an optical access wide enough to avoid any interference with the measurement beam, and the necessity of preventing microwaves leakage.

Pyrometers have been selected according to the following specifications:

1. Measurement range from room temperature up to 1000 °C. The maximum temperature of the material is not expected to exceed this value.
2. Small measurement beam, for ensuring its passage through the optical accesses. No physical interference between the measurement beam and the holes in the refractory layer should happen.
3. Sensitivity spectrum matching the high-emissivity spectra of alumina (i.e. the material to be used for the container tube).

   It has been done a preliminary literature survey, in order to identify the emissivity behavior of this material. Figure 50 is an example of the data retrieved.
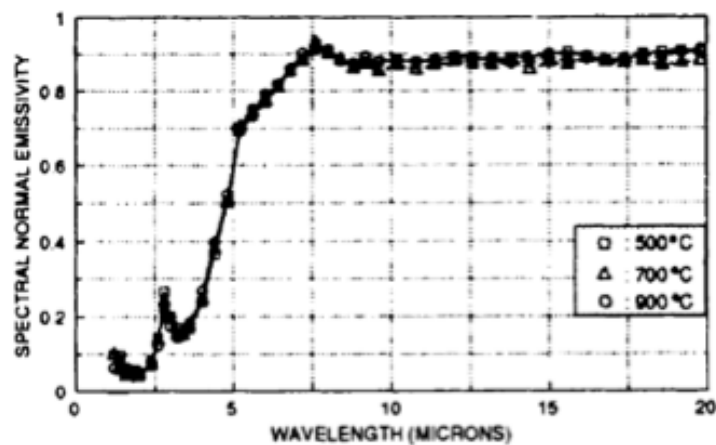

Figure 50. Alumina emissivity spectrum [98].

A high-emissivity coating (AREMCO 840-CHiE Coat-ceramic based) has been identified, for increasing the emissivity of the surface. The emissivity spectrum of this coating is shown in Figure 51.
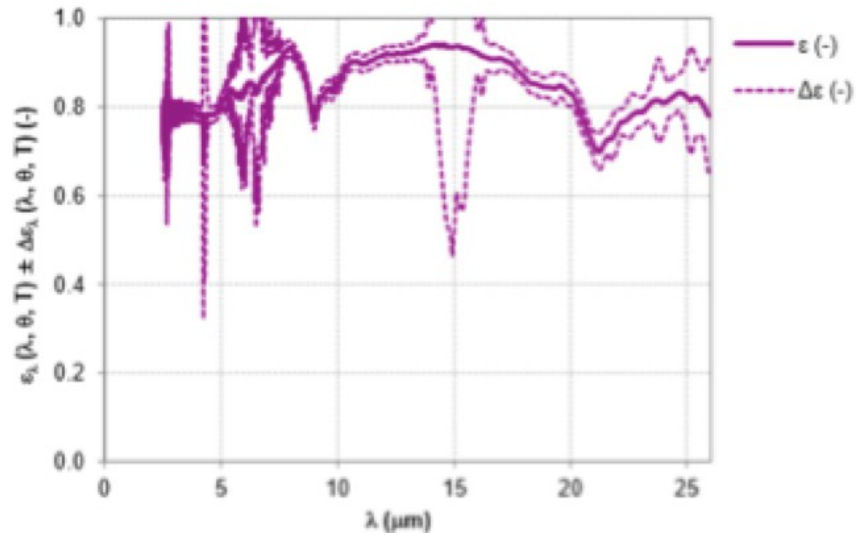

Figure 51. Coating emissivity spectrum at 300 °C.

Figure 52a and Figure 52b are referred to a high-temperature test on alumina samples, with (b) and without (a) the high-emissivity coating applied. Here measurements provided by a long-IR pyrometer (emissivity set to 1) are compared to those obtained with a contact element. As it can be noted, when the coating is applied the problems related with emissivity setting are overcame.
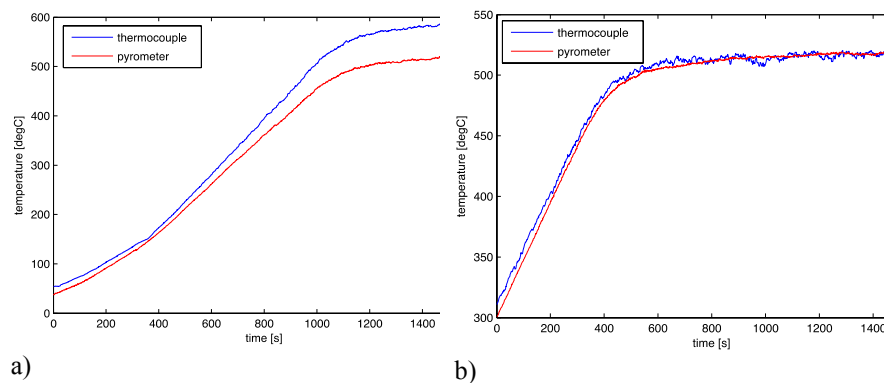

a)   b)

Figure 52. IR measurements with (b) and without (a) the high-emissivity coating.

77

A surface emissivity estimation test has been performed, in order to set the proper emissivity correction for alumina whenever the coating cannot be applied. The experimental setup is shown in Figure 53. Here the specimen is placed on a metallic support located inside a coil. The metal is inductively heated up to 1200 °C with a ramp of 1 °C/min, then maximum temperature is maintained for about 10 minutes. The alumina sample is heated by conduction from the support, and during the heating period its temperature is monitored using one contact element and one long-IR pyrometer. Temperature data recorded by the two sensors are shown in Figure 54. The temperature offset of the pyrometer respect to the thermocouple indicates an emissivity of 0.48, which is considerably different respect to the value indicated by literature [98].
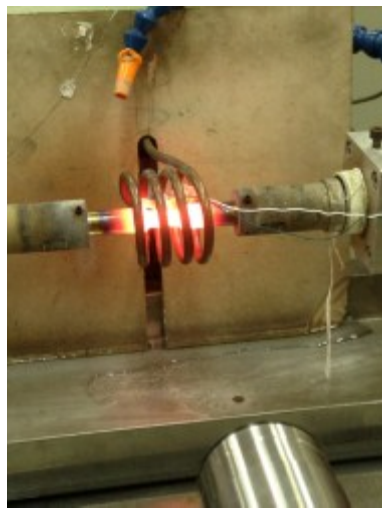

Figure 53. Experimental setup for the estimation of emissivity.

According to the previous specifications, three pyrometers Lumasense IMPAC IN 5/9 Plus have bee selected. They show the following features:
1. Measurement range from 0 up to 1500 °C.
2. A measurement spot of 4.5 mm at a distance of 280 mm.
3. A narrow sensitivity spectrum in the long-IR (8 – 9.7 μm).

Pyrometers have been installed in the demonstrator during preliminary tests. The devices are mounted on a supporting frame, outside the cavity. A laser beam helps achieving the alignment of the measurement spot with the optical access. Pyrometers are powered using a 20 V DC voltage supply; the 4-20 mA output signal is sent to the PLC. The temperature reading during operation of the cavity is shown in Figure 55. The information is acquired by the soft sensor.
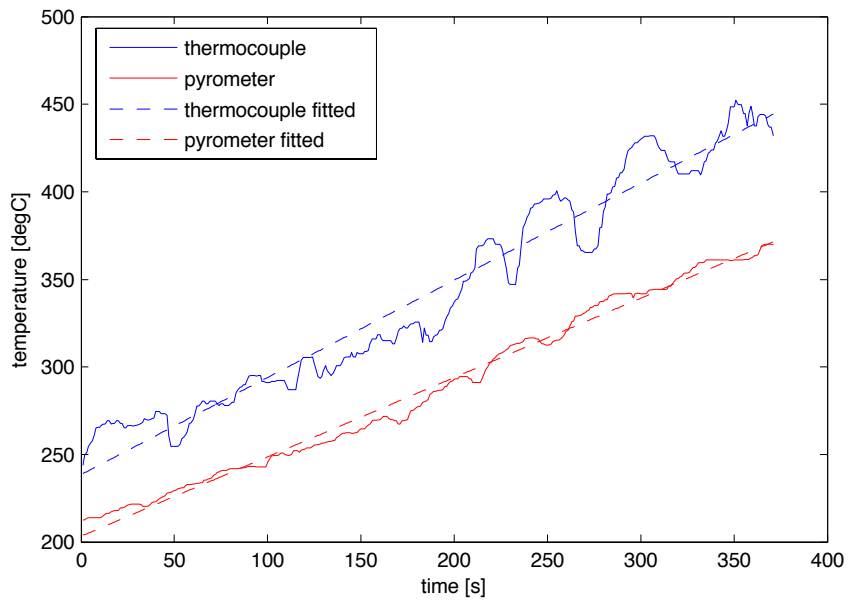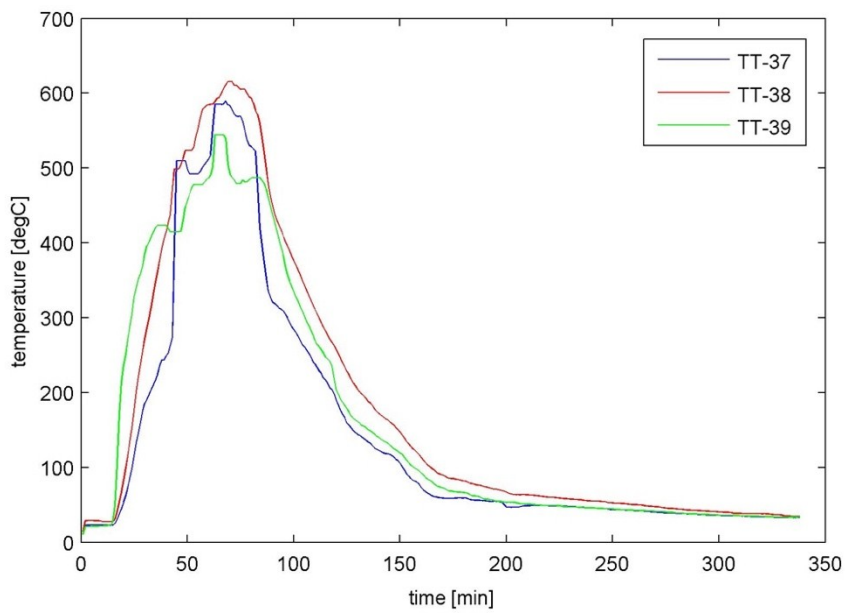
Figure 54. Measurements from pyrometer and contact sensor.

Figure 55. Temperature measurements during operation.

5.4 - Results

The soft sensor has been tested during a preliminary trial of the demonstrator, the 15th of July 2015.

Direct measurements of the maximum temperature of the material inside the cavity have been performed, in order to gather comparative data for validating the new monitoring approach. To that purpose, an IR camera has been placed outside the cavity, pointing at the exit of the tube and with optical access to the inside. Figure 56 shows a sample of the thermal sequence recorded during the test of the demonstrator. The temperature of the material is considerably higher then the rest of the tube, so the hottest spot (area of maximum temperature) can be tracked quite easily. Figure 57 reports the average on the 100 hottest pixels vs. time, which can been assumed as the maximum temperature of the material. Emissivity correction has not been introduced, since the material is in powder state and therefore high emissivity values are expected.
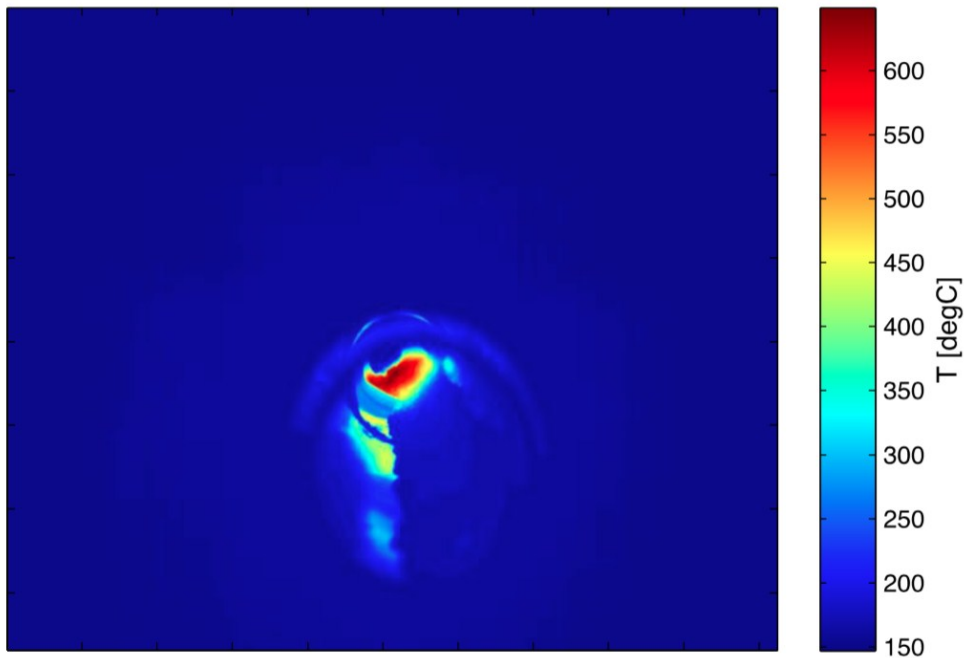

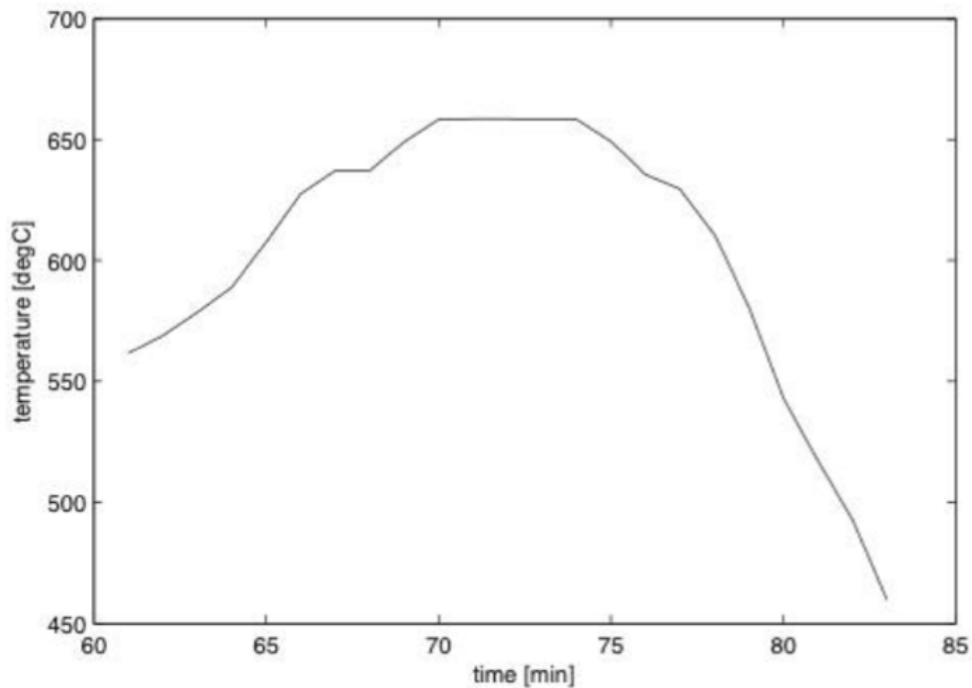*Figure 56. Thermal image from the outside of the cavity.*

Figure 57. Maximum temperature of the material vs. time.

Measurements gathered during the 67 min testing period have shown the following trends:

I. Electric power. The power analyzer has provided an overall 10 kWh consumption during the test. Energy consumption is uniformly distributed during the whole time. This entails a 9 kW incident power, from magnetron startup until shutdown. Half of the total incident power has been sent to the cavity; the other half has been dissipated on a water load.

II. HiPoM. Absorbed and back-reflected power components have shown significant oscillations during the test period.

III. Temperature of the tube. It rises as material starts heating up, then cools down after magnetron shutdown.

IV. Maximum temperature of the material. This measurement has been provided by the IR camera for a short period after magnetron shutdown. Measurements have not been performed during microwaves application because of the presence of high-temperature plasma, which could have damaged the sensor. Further, measurements have been interrupted after the temperature went below the 400 °C minimum range of the sensor.

Prediction of the soft sensor for the maximum temperature of the material during the whole test period is shown in Figure 58, together with measurements from the IR camera:
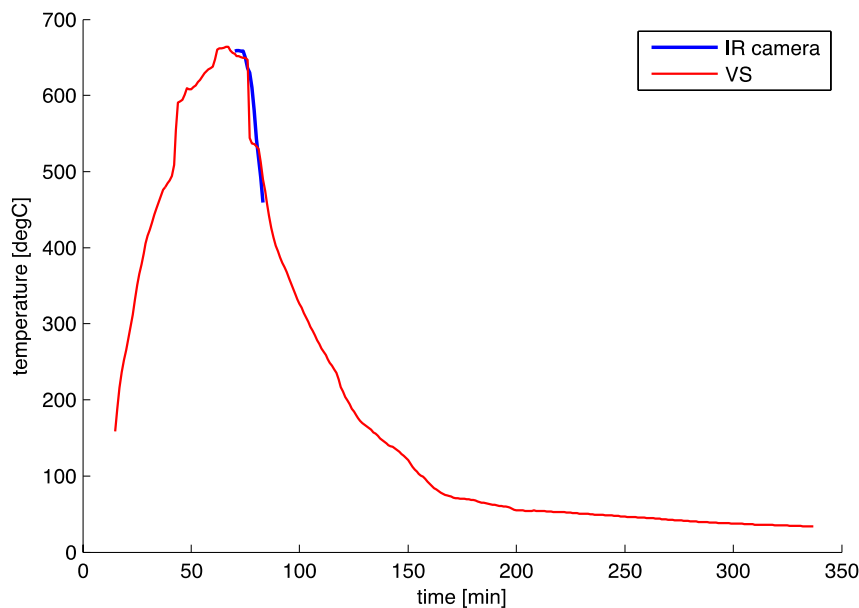
81

Figure 58. Prediction from the soft sensor and direct measurement from the IR camera for the maximum temperature of the material.

Despite high uncertainty still affecting some measurements, two conclusions can be drawn:

I. The soft sensor shows adequate accuracy. Its estimations are in good agreement with data gathered by the IR camera.

II. According to the predictions from the soft sensor and measurements from the pyrometers, the following thermal behavior of the cavity can be deduced (Figure 59): immediately after magnetron startup the electromagnetic field produces a fast bulk heating of the material (*heating1*), which rises its temperature above over 100 °C respect to the tube. Subsequently, a slower heating of the whole system (material and tube) starts (*heating2*), where the temperature of the material follows that of the tube unless a constant offset. After magnetron shutdown the heat source goes to zero, thus the temperature gap between the material and the tube is rapidly reduced (*cooling1*). During the rest part of the cooling period, temperature of the material closely follows that of the tube.

Therefore, it can be concluded that an indirect assessment of the temperature of the material can be effectively achieved from an accurate measurement of the temperature of the tube, unless a constant offset for the period when the magnetron is turned on. This offset can be estimated by knowing the instantaneous absorbed power and the heat transfer coefficient between the wall and the material bed.
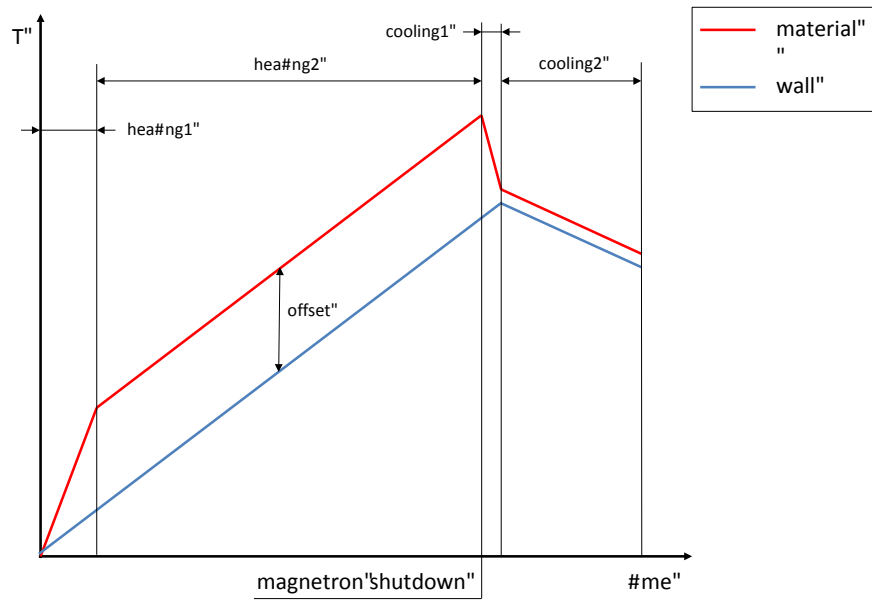
Figure 59. Thermal behavior of the cavity.

Concluding Remarks

In the present contribution an innovative monitoring approach based on soft sensing has been proposed for the process industry. An application case involving the clinker production process has been discussed.

First part of the activity has faced the development of a simulative CFD-FEA model, which provides an accurate representation of several aspects involved in the kiln operation, i.e.: the turbulent aerodynamic field in the proximity of the multi-channel burner; the gas flowing inside the kiln; fuel combustion; conductive, convective and radiative heat exchanges between the different domains; chemical conversion of the material bed. The model has been subsequently validated. The omni-comprehensive predictions have shown adequate accuracy respect to an experimental data set from the real plant. Subsequently, a second theoretical representation of the same kiln has been conduced using a simpler model based on lumped elements. Critical parameters of the lumped model have been adjusted using a multi-objective optimization strategy based on the application of genetic algorithms. Predictions from the CFD-FEA model have been used as a reference during optimization. Further activity has dealt with the development of a calculation routine, which allows for exploiting the lumped model in predictions of the kiln's behavior on a stationary state, besides forecasts of the transient response after changing one or more operative parameters. Finally, a graphical user interface has been implemented. The soft sensor has shown marked potentialities when tested in on-line applications: extremely reduced calculation times make it a more exploitable tool respect to stand-alone models. Its reliability opens the way to several applications, among which indirect monitoring of non-accessible variables and development of new control strategies.

The same monitoring approach has been proposed for a second sintering stage developed inside the EU FP7 project DAPhNE (grant agreement n° 314636) and based on a mono-modal, high-power, microwave applicator. The possibility for intervening in the preliminary design of the monitoring architecture has been fully exploited in order to achieve the complete integration of the new tool to the rest of the hardware devices. First part of the activity has been focused over the development of direct monitoring strategies, addressed at the assessment of electrical and thermal variables at field level. A second lumped model has been developed for the microwave module, accounting for the new bulk heating. The model has been connected to the control PLC through an OPC-server-client polling architecture: it gathers real-time data from the field devices and provides transient forecasts at a regular time base. The soft sensor has been validated during a preliminary test of the new module. Field measurements from an IR camera have been used for validating its estimates. The new tool has shown good accuracy; its predictions have helped the understanding of the thermal behavior of the whole system during a typical operation.

Final part of the work has faced the unpublished problem of the estimation of uncertainty of the soft sensor. To that scope, a stochastic method based on the adaptive Monte Carlo procedure prescribed by the GUM (Guide to the Expression of Uncertainty in Measurements) has been applied for esteeming the propagation of input uncertainties through the mathematical model. Finally, an innovative modeling framework has been used for

quantifying the uncertainty introduced by the simplified representation provided by the lumped model.

References

[1] P. Kadlec, B. Gabrys, S. Strandt, "Data-driven Soft Sensors in the process industry", Computers and Chemical Engineering, vol. 33, pp. 795-814, 2009.

[2] I. Mohler, N. Bolf, G. Galinec, M. Golob, "Application of Soft Sensor for Monitoring and Control of Refinery Emission".

[3] A. Casali, G. Gonzalez, F. Torres, G. Vallebuona, L. Castelli, P. Gimenez, "Particle size distribution soft-sensor for a grinding circuit", Powder Technology, vol. 99, pp. 15-21, 1998.

[4] S. Park, C. Han, "A nonlinear soft sensor based on multivariate smoothing procedure for quality estimation in distillation columns", Computers and Chemical Engineering, vol. 24, pp. 871-877, 2000.

[5] S. J. Qin, H. Yue, R. Dunia, "Self-validating inferential sensors with application to air emission monitoring", Industrial & Engineering Chemistry Research, vol. 36, pp. 1675-1685, 1997.

[6] V. R. Radhakrishnan, A. R. Mohamed, "Neural networks for the identification and control of blast furnace hot metal quality", journal of Process Control, vol. 10, pp. 509-524, 2000.

[7] D. Devogelaere, M. Rijckaert, O. G. Leon, C. G. Lemus, "Application of feed-forward neural networks for soft sensors in the sugar industry", proceedings of the VII Brazilian symposium on neural networks, 2002.

[8] L. Fortuna, S. Graziani, M. G. Xibilia, "Soft sensors for product quality monitoring in debutanizer distillation columns", Control Engineering Practice, vol. 13, pp. 499-508, 2005.

[9] S. H. Yang, B. H. Chen, X. Z. Wang, "Neural network based fault diagnosis using unmeasurable inputs", Engineering Applications of Artificial Intelligence, vol. 13, pp. 345-356, 2000.

[10] P. Kadlec, B. Gabrys, "Learnt topology gating artificial neural network", proceedings of the 2008 IEEE International joint conference on neural networks, 2008.

[11] K. Desai, Y. Badhe, S. S. Tambe, B. D. Kulkarni, "Soft sensor development for feed-batch bioreactors using support vector regression", Biochemical Engineering Journal, vol. 27, pp. 225-239, 2006.

[12] L. Wang, C. Shao, H. Wang, H. Wu, "Radial basis function neural networks-based modeling of the membrane separation process: Hydrogen recovery from refinery gases", Journal of of Natural Gas Chemistry, vol. 15, pp. 230-234, 2006.

[13] H. B. Su, L. T. Fan, J. R. Schlup, "Monitoring the process of curing of epoxy/graphite fiber composites with a recurrent neural network as a soft sensor", Engineering Applications of Artificial Intelligence, vol. 11, pp. 293-306, 1998.

[14] L. Z. Chen, S. K. Nguang, X. M. Li, X. D. Chen, "Soft sensors for on-line biomass measurements", Bioprocess and Biosystems Engineering, vol. 26, pp. 191-195, 2004.

[15] X. Chen, F. Gao, G. Chen, "A soft-sensor development for melt-flow-length measurement during injection mold filling", Materials Science & Engineering, vol. 384, pp. 245-254.

[16] Y. Yang, T. Chai, "Soft sensing based on artificial neural network", proceedings of the 1997 American control conference, 1997.

[17] R. Dunia, J. Qin, T. F. Edgar, T. J. McAvoy, "Sensor fault identification and reconstruction using principal component analysis", proceedings of the 13th triennial IFAC world congress, 1996.

[18] B. S. Dayal, J. F. MacGregor, "Recursive exponentially weighted PLS and its applications to adaptive control and prediction", Journal of Process Control, vol. 7, pp. 169-179, 1997.

[19] S. J. Qin, "Recursive PLS algorithms for adaptive data modeling", Computers and Chemical Engineering, vol. 22, pp. 503-514.

[20] E. Zamprogna, M. Barolo, D. E. Seborg, "Estimating product composition profiles in batch distillation via partial least squares regression", Control Engineering Practice, vol. 12, pp. 917-929, 2004.

[21] B. Lin, B. Recke, J. Knudsen, S. B. Jrgensen, "A systematic approach for soft sensor development", Computers and Chemical Engineering, vol. 31, pp. 419-425, 2007.

[22] P. Nomikos, J. F. MacGregor, "Multivariate SPC charts for monitoring batch processes", Technometrics, vol. 37, pp. 41-59, 1995.

[23] M. Amazouz, R. Pantea, "Use of multivariate data analysis for lumber drying process monitoring and fault detection", proceedings of the international conference on data mining, 2006.

[24] H. Zhang, B. Lennox, "Integrated condition monitoring and control of fed-batch fermentation process", Journal of Process Control, vol. 14, pp. 41-50, 2004.

[25] O. Marjanovic, B. Lennox, D. Sandoz, K. Smith, M. Crofts, "Real-time monitoring of an industrial batch process", Computers and Chemical Engineering, vol. 30, pp. 1476-1481, 2006.

[26] W. Li, H. H. Yue, S. Valle-Cervantes, S. J. Qin, "Recursive PCA for adaptive process monitoring", Journal of Process Control, vol. 10, pp. 471-486, 2000.

[27] Q. P. He, S. J. Qin, J. Wang, "A new fault diagnosis method using fault directions in fisher discriminant analysis", AIChE Journal, vol. 51, pp. 555-571, 2005.

[28] P. Kampjarvi, M. Sourander, T. Komulainen, N. Vatanski, M. Nikus, S. L. Jms-Jounela, "Fault detection and isolation of an on-line analyzer for an ethylene cracking process", Control Engineering Practice, vol. 16, pp. 1-13, 2008.

[29] R. Dunia, S. J. Qin, "Joint diagnosis of process and sensor faults using principal component analysis", Control Engineering Practice, vol. 6, pp. 457-469, 1998.

[30] R. Dunia, S. J. Qin, "Subspace approach to multidimensional identification and reconstruction", AIChE Journal, vol. 44, pp. 1813-1831, 1998.

[31] C. Lee, S. W. Choi, I. B. Lee, "Sensor fault identification based on time-lagged PCA in dynamic processes", Chemometrics and Intelligent Laboratory Systems, vol. 70, pp. 165-178, 2004.

[32] S. Wang, J. Cui, "Sensor-fault detection, diagnosis and estimation for centrifugal chiller systems using principal-component analysis method", Applied Energy, vol. 82, pp. 197-213, 2005.

[33] W. Yan, H. Shao, X. Wang, "Soft sensing modeling based on support vector machine and Bayesian model selection", Computers and Chemical Engineering, vol. 28, pp. 1489-1498, 2004.

[34] R. Feng, W. Shen, H. Shao, "A soft sensor modeling approach using support vector machines", proceedings of the 2003 American control conference, 2003.

[35] S. Merikoski, M. Laurikkala, H. Koivisto, "An adaptive neuro-fuzzy inference system as a soft sensor for viscosity in rubber mixing process", Tech. rep. WSEAS NNA-FSFS-EC, 2001.

[36] K. Warne, G. Prasad, N. Siddique, L. P. Maguire, "Development of a hybrid PCA-ANFIS measurement system for monitoring product quality in the coating industry", proceedings of the 2004 IEEE international conference on systems, man and cybernetics, 2004.

[37] J. X. Luo, H. H. Shao, "Developing soft sensors using hybrid soft computing methodology: A neurofuzzy system based on rough set theory and genetic algorithms", Soft Computing – A fusion of Foundations Methodologies and Applications, vol. 10, pp. 54-60, 2006.

[38] M. J. Arazo-Bravo, J. M. Cano-Izquierdo, E. Gmez-Snchez, M. J. Lpez-Nieto, Y. A. Dimitriadis, J. Lpez-Coronado, "Automatization of a pencilin production process with soft sensors and adaptive controller based on neuro fuzzy systems", Control Engineering Practice, vol. 12, pp. 1073-1090, 2004.

[39] J. J. Macias, P. X. Zhou, "A method for predicting quality of the crude oil distillation", proceedings of the 2006 International symposium on evolving fuzzy systems, 2006.

[40] V. Venkatasubramanian, R. Rengaswamy, K. Yin, S.N. Kavuri, "A review of process fault detection and diagnosis Part I: Quantitative model-based methods", Computers and Chemical Engineering, vol. 27, pp. 293-311, 2003.

[41] P. M. Frank, "Fault diagnosis in dynamic systems using analytical and knowledge-based redundancy – a survey and some new results", Automatica, vol. 26, pp. 459-474, 1990.

[42] R. K. Mehra, J. Peschon, "An innovations approach to fault detection and diagnosis in dynamic systems", Automatica, vol. 7, pp. 637-640, 1971.

[43] M. A. Kramer, "Malfunction diagnosis using quantitative models with non-boolean reasoning in expert systems", AIChE Journal, vol. 33, pp. 130-140, 1987.

[44] K. Fukunaga, "Introduction to statistical pattern recognition", New York: Academic press, 1972.

[45] J. Gertler, "Analytical redundancy methods in fault detection and isolation", proceedings of IFAC / IAMCS symposium on safe process, 1991.

[46] A. Jos de Assis, R. Maciel Filho, "Soft sensors development for on-line bioreactor state estimation", Computers and Chemical Engineering, vol. 24, pp. 1099-1103, 2000.

[47] S. James, R. Legge, H. Budman, "Comparative study of black-box and hybrid estimation methods in fed-batch fermentation", Journal of Process Control, vol. 12, pp. 113-121, 2002.

[48] L. A. C. Meleiro, R. M. Finho, "A self-tuning adaptive control applied to an industrial large scale ethanol production", Computers and Chemical Engineering, vol. 24, pp. 925-930, 2000.

[49] C. M. Atkinson, T. W. Long, E. L. Hanzevack, "Virtual Sensing: A Neural Network-based Intelligent Performance and Emissions Prediction System for On-Board Diagnostics and Engine Control", International Congress and Exposition, Detroit, 1998.

[50] S. De Wolf, R. L. E. Cuypers, L. C. Zullo, B. J. Vos, B. J. Bax, "Model predictive control of a slurry polymerization reactor", Computers and Chemical Engineering, vol. 20, pp. 955-961, 1996.

[51] F. J. Doyle, "Nonlinear inferential control for process applications", Journal of Process Control, vol. 8, pp. 339-353, 1998.

[52] V. Prasad, M. Schley, L. P. Russo, B. Wayne Bequette, "Product property and production rate control of styrene polymerization", Journal of Process Control vol. 12, pp. 353-372, 2002.

[53] Evaluation of measurement data – supplement 1 to the "guide to the expression of uncertainty in measurement" – propagation of distributions using a Monte Carlo method, Joint Committee for Guides in Metrology, 2008.

[54] G. Frohnsdorff, J. Rumble, SRM2686, National Institute of Standard and Technology, 2002.

[55] http://www.cement.org/market-economics/forecasts

[56] M. Schneider, M. Romer, M. Tschudin, H. Bolio, "Sustainable cement production – present and future", Cement and Concrete Research, vol. 41, pp. 642-650, 2011.

[57] M. Schneider, "Process technology for efficient and sustainable cement production", Cement and Concrete Research, vol. 78, pp. 14-23, 2015.

[58] J. Khatib, "Sustainability of Construction Materials", Woodhead Publishing, 2009.

[59] J. W. Phair, "Green chemistry for sustainable cement production and use", Green Chemistry, vol. 8, pp. 763-780, 2006.

[60] D. P. Bentz, A. S. Hansen, J. M. Guynn, "Optimization of cement and fly ash particle sizes to produce sustainable concretes", Cement and Concrete Composites, vol. 33, pp. 824-831, 2011.

[61] D. N. Huntzinger, T. D. Eatmon, "A life-cycle assessment of Portland cement manufacturing: comparing the traditional process with alternative technologies", Journal of Cleaner Production, vol. 17, pp. 668-675, 2009.

[62] F. Schorcht, I. Kourti, B. M. Scalet, S. Roudier, L. D. Sancho, "Best Available Techniques (BAT) reference document for the production of cement, lime and magnesium oxide", Joint Research Centre Instute for Prospective Technological Studies Sustainable Production and Consumption Unit European IPPC Bureau, 2013.

[63] http://ietd.iipnetwork.org/content/cement#technology-resources.

[64] T. Engin, V. Ari, "Energy auditing and recovery for dry type cement rotary kiln systems – A case study", Energy Conversion and Management, vol. 46, pp. 551-562, 2005.

[65] M. Fallahpour, A. Fetehi, B. N. Araabi, M. Azizi, "A neuro-fuzzy controller for rotary cement kilns", proceedings of the 17th World Congress The international Federation of Automatic Control, 2008.

[66] P. M. Larsen, "Industrial applications of fuzzy logic control", International Journal of Man-Machine Studies, vol. 12, pp. 3-10, 1980.

[67] X. Wang, Q. Meng, H. Yu, Z. Yuan, X. Xu, "Distributed control for cement production of vertical shaft kiln", International Journal of Information and Systems Sciences, vol. 1, pp. 264-274, 2005.

[68] Z. Yuan, Z. Liu, R. Pei, "Fuzzy control of cement raw meal production", proceedings of the International Conference on Automation and Logistics, 2008.

[69] K. C. Karki, S. V. Patankar, J. Grant, "Simulation of fluid flow, combustion and heat transfer in a coal-fired cement kiln", ASME Publications, vol. 367, pp. 103-114, 2000.

[70] T. B. Bhad, S. Sarkar, A. Kaushik, S. V. Herwadkar, "CFD modeling of a cement kiln with multi channel burner for optimization of flame profile", proceedings of the 17th International Conference on CFD in the Minerals and Process Industries, 2009.

[71] K. S. Mujumdar, V. V. Ranade, "CFD modeling of rotary cement kilns", Asia-Pacific Journal of Chemical Engineering, vol. 3, pp. 106-118, 2008.

[72] H. Mikulcic, M. Vujanovic, D. K. Fidaros, P. Priesching, I. Minic, R. Tatschl, N. Duic, G. Stefanovic, "The application of CFD modeling to support the reduction of CO2 emissions in cement industry", proceedings of the 24th International Conference on Efficiency, Cost, Optimization, Simulation and Environmental Impact of Energy, 2011.

[73] S. Wang, J. Lu, W. Li, Z. Hu, "Modeling of pulverized coal combustion in cement rotary kiln", Energy Fuels, vol. 20, pp. 2350-2356, 2006.

[74] M. Ai-chun, Z. Jie-min, O. Jian-ping, L. Wang-xing, "CFD prediction of physical field for multi-air channel pulverized coal burner in rotary kiln", Journal of Central South University of Technology, vol. 13, pp. 75-79, 2006.

[75] D. K. Fidaros, C. A. Baxevanou, C. D. Dritselis, N. S. Vlachos, "Numerical modeling of flow and transport processes in a calciner for cement production", Powder Technology, vol. 171, pp. 81-95, 2007.

[76] T. Avgeropoulos, J. P. Glekas, C. Papadopoulos, "Numerical Simulation of the Combustion Aerodynamics inside a Rotary Cement Kiln", Springer, 1993.

[77] M. Aichun, Z. Jiemin, L. Wangxing, "CFD prediction of cold airflow field for multiair channel pulverized coal burner in rotary kiln", proceedings of the IECEC, 2004.

[78] M. A. R. Valle, "Numerical modeling of granular beds in rotary kilns", PhD thesis, Deft University of Technology, 2012.

[79] A. Boateng, P. V. Barr, "A thermal model for the rotary kiln including heat transfer within the bed", International Journal of Heat and Mass transfer, vol. 39, pp. 2131-2147, 1996.

[80] H. A. Spang, "A dynamic model of a cement kiln", Automatica, vol. 8, pp. 309-323, 1972.

[81] K. S. Mujumdar, V. V. Ranade, "Simulation of rotary cement kilns using a one-dimensional model", Chemical Engineering Research and Design, vol. 84, pp. 165-177, 2006.

[82] E. Mastorakos, A. Massias, C. D. Tsakiroglou, D. A. Goussis, V. N. Burganos, A. Payatakes, "CFD predictions for cement kilns including flame modeling, heat transfer and clinker chemistry", Applied Mathematical Modeling, vol. 23, pp. 55-76, 1999.

[83] J. P. Gorog, "Heat transfer in direct-fired rotary kilns", PhD thesis, Université du Luxembourg.

[84] J. P. Gorog, "Heat transfer from flames in a rotary kiln", Metallurgical Transactions, vol. 14, pp. 411-424, 1983.

[85] L. G. Ndiaye, S. Caillat, A. Chinnayya, D. Gambier, B. Baudoin, "Application of the dynamic model of saeman to an industrial rotary kiln incinerator: numerical and experimental results", Waste Management, vol. 30, pp. 1188-1195, 2010.

[86] A. D. Polyanin, V. F. Zaitsev, "Handbook of Exact Solutions for Ordinary Differential Equations", Chapman and Hall/CRC Press, 2003.

[87] R. Courant, K. Friedrichs, H. Lewy, "On the partial differential equations of mathematical physics", IBM Journal of Research and Development, vol. 11, pp. 215-234, 1967.

[88] A. A. Donoso, B. Peters, "XDEM employed to predict reduction of tungsten oxide in a dry hydrogen atmosphere", International Journal of Refractory Metals and Hard Materials.

[89] A. A. Donoso, F. Hoffmann, B. Peters, "Extended discrete element method used for convective heat transfer predictions", International Review of Mechanical Engineering, vol. 7, pp. 328-336, 2013.

[90] B. Peters, X. Besseron, A. Estupinan, F. Hoffmann, M. Michael, A. Mahmoudi, "The extended dicrete element method (XDEM) applied to drying of a packed bed", IFRF Journal.

[91] A. H. Mahmoudi, F. Hoffmann, B. Peters, "Application of XDEM as a novel approach to predict drying of a packed bed", International Journal of Thermal Sciences, vol. 75, pp. 65-75, 2014.

[92] E. Copertaro, P. Chiariotti, A. A. E. Donoso, N. Paone, B. Peters, G. M. Revel, "A discrete-continuous approach to describe CaCO3 decarbonation in non-steady thermal conditions", Powder Technology, vol. 275, pp. 131-138, 2015.

[93] B. Peters, "Thermal conversion of solid fuels", WIT press, 2003.

[94] E. J. Kansa, H. E. Perlee, R. F. Chaiken, "Mathematical model of wood pyrolysis including internal forced convection", Combustion and Flame, vol. 29, pp. 311-324, 1977.

[95] A. Faghri, Y. Zhang, "Transport Phenomena in Multiphase Systems", Elsevier, 2006.

[96] X. Y. Liu, E. Specht, O. G. Gonzalez, P. Walzel, "Analytical solution for the rolling-mode granular motion in rotary kilns", Chemical Engineering and Processing: Process Intensification, vol. 45, pp. 515-521, 2006.

[97] A. A. Boateng, "Rotary Kilns: Transport Phenomena and Transport Processes", Elsevier, 2008.

[98] http://www.academia.edu/4812013/materials_for_nuclear_systems_in_situ_measu rements_of_spectral_emissivity_of_materials_for_very_high_temperature_reactor s.

Appendix A.1 – adaptive Monte Carlo procedure

Hereafter the adaptive Monte Carlo method. Its objective is to provide a) an estimate y of the output quantity Y, b) an associated standard uncertainty $u(y)$ and c) the endpoints y_{low} and y_{high} of a coverage interval for Y corresponding to a stipulated coverage probability such that each of these four values can be expected to meet the numerical tolerance required.

1. Set n_{dig} to an appropriate small positive integer, representing the number of significant decimal digits regarded as meaningful in the numerical value of y;

2. Set:

$$M = \mathbf{max}(J, 10^4)$$

   Where J is the smallest integer greater than or equal to $100/(1-p)$, being p the coverage probability;

3. Set $h=1$, denoting the first application of MCM in the sequence;

4. Carry out M Monte Carlo trials, using input probability distributions;

5. Use the M model values $y_1 \ldots y_M$ so obtained to calculate $y^{(h)}$, $u(y^{(h)})$, $y_{low}^{(h)}$ and $y_{high}^{(h)}$, as an estimate of Y, the associated standard uncertainty, and the left- and right-hand endpoints of a $100p$ % coverage interval, respectively, for the hth member of the sequence.

6. If $h=1$, increase h by one and return to step 4.

7. Calculate the standard deviation s_y associated with the average of the estimates $y^{(1)} \ldots y^{(h)}$ of Y, given by:

$$s_y^2 = \frac{1}{h(h-1)} \sum_{r=1}^{h} \left(y^{(r)} - y \right)^2$$

   Where:

$$y = \frac{1}{h} \sum_{r=1}^{h} y^{(r)}$$

8. Calculate the counterpart of this statistic for $u(y)$, y_{low} and y_{high};

8. Use all $h \times M$ model values available so far to form $u(y)$;

9. Calculate the numerical tolerance δ associated with $u(y)$;

10. If any of $2s_y$, $2s_{u(y)}$, $2s_{ylow}$ and $2s_{yhigh}$ exceeds δ, increase h by one and return to step 4;

11. Regard the overall computation as having stabilized, and use all the $h \times M$ model values obtained to calculate y, $u(y)$ and a $100p$ % coverage interval.

Appendix A.2 – CFD-FEA model for the conventional rotary kiln

Chemical conversions:

$$\frac{\partial C_{CaCO_3}}{\partial t} = -u_s \cdot \frac{\partial C_{CaCO_3}}{\partial z} - R_{CaCO_3} \tag{69}$$

$$\begin{aligned}\frac{\partial CaO}{\partial t} = &-u_s \cdot \frac{\partial CaO}{\partial z} + \frac{M_{CaO}}{M_{CaCO_3}} \cdot R_{CaCO_3} - 2\frac{M_{CaO}}{M_{C2S}} \cdot R_{C2S} - 3\frac{M_{CaO}}{M_{C3A}} \cdot R_{C3A} \\ &- 4\frac{M_{CaO}}{M_{C4AF}} \cdot R_{C4AF} - \frac{M_{CaO}}{M_{C3S}} \cdot R_{C3S}\end{aligned} \tag{70}$$

$$\frac{\partial C_{SiO_2}}{\partial t} = -u_s \cdot \frac{\partial C_{SiO_2}}{\partial z} - \frac{M_{SiO_2}}{M_{C2S}} \cdot R_{C2S} \tag{71}$$

$$\frac{\partial C_{Al_2O_3}}{\partial t} = -u_s \cdot \frac{\partial C_{Al_2O_3}}{\partial z} - \frac{M_{Al_2O_3}}{M_{C4AF}} \cdot R_{C4AF} - \frac{M_{Al_2O_3}}{M_{C3A}} \cdot R_{C3A} \tag{72}$$

$$\frac{\partial C_{Fe_2O_3}}{\partial t} = -u_s \cdot \frac{\partial C_{Fe_2O_3}}{\partial z} - \frac{M_{Fe_2O_3}}{M_{C4AF}} \cdot R_{C4AF} \tag{73}$$

$$\frac{\partial C_{C2S}}{\partial t} = -u_s \cdot \frac{\partial C_{C2S}}{\partial z} + R_{C2S} - \frac{M_{C2S}}{M_{C3S}} \cdot R_{C3S} \tag{74}$$

$$\frac{\partial C_{C3A}}{\partial t} = -u_s \cdot \frac{\partial C_{C3A}}{\partial z} + R_{C3A} \tag{75}$$

$$\frac{\partial C_{C4AF}}{\partial t} = -u_s \cdot \frac{\partial C_{C4AF}}{\partial z} + R_{C4AF} \tag{76}$$

$$\frac{\partial C_{C3S}}{\partial t} = -u_s \cdot \frac{\partial C_{C3S}}{\partial z} + R_{C3S} \tag{77}$$

Being:

$$R_{CaCO_3} = k_{CaCO_3} \cdot C_{CaCO_3} \qquad \text{Rate of CaCO}_3 \text{ decomposition}$$

$$R_{C2S} = k_{C2S} \cdot C_{CaO}^2 \cdot C_{SiO_2} \qquad \text{Rate of C2S formation}$$

$$R_{C4AF} = k_{C4AF} \cdot C_{CaO}^4 \cdot C_{Al_2O_3} \cdot C_{Fe_2O_3} \qquad \text{Rate of C4AF formation}$$

$$R_{C3A} = k_{C3A} \cdot C_{CaO}^3 \cdot C_{Al_2O_3} \qquad \text{Rate of C3A formation}$$

$$R_{C3S} = k_{C3S} \cdot C_{CaO} \cdot C_{C2S} \qquad \text{Rate of C3S formation}$$

$$k_{CaCO_3} = A_{CaCO_3} \cdot exp\left(\frac{-E_{CaCO_3}}{R_g \cdot T_s}\right) \qquad \text{Rate constant of CaCO}_3 \text{ decomposition}$$

$$k_{C2S} = A_{C2S} \cdot exp\left(\frac{-E_{C2S}}{R_g \cdot T_s}\right) \qquad \text{Rate constant of C2S formation}$$

$$k_{C4AF} = A_{C4AF} \cdot exp\left(\frac{-E_{C4AF}}{R_g \cdot T_s}\right) \qquad \text{Rate constant of C4AF formation}$$

$$k_{C3A} = A_{C3A} \cdot exp\left(\frac{-E_{C3A}}{R_g \cdot T_s}\right) \qquad \text{Rate constant of C3A formation}$$

$$k_{C3S} = A_{C3S} \cdot exp\left(\frac{-E_{C3S}}{R_g \cdot T_s}\right) \qquad \text{Rate constant of C3S formation}$$

Heat from chemical conversion:

$$Q_s = \frac{M}{u_s} \cdot \left(\Delta h_{CaCO_3} \cdot R_{CaCO_3} + \Delta h_{C2S} \cdot R_{C2S} + \Delta h_{C4AF} \cdot R_{C4AF} + \Delta h_{C3A} \cdot R_{C3A} + \Delta h_{C3S} \cdot R_{C3S}\right) \qquad (78)$$

Symbols:

C2S	Belite
C3A	Aluminate
C4AF	Ferrite
C3S	Alite
M	Mass flow raw meal
M_i	Molar mass of *i*-specie
C_i	Mass concentration of *i*-specie
R_i	Rate of *i*-reaction
A_i	Pre-exponential factor of *i*-reaction
E_i	Activation energy of *i*-reaction
Δh_i	Enthalpy of *i*-reaction

Appendix A.3 – LEM model for the conventional rotary kiln

Heat exchange coefficients:

$$h_{gw} = (2\pi - p) \cdot r_{int} \cdot \left[Conv_{gw} + \epsilon_g \epsilon_w \left(T_g^2 + T_{wi}^2\right)\left(T_g + T_{wi}\right)\right] \tag{79}$$

$$h_{sw} = p \cdot r_{int} \cdot \left[Conv_{sw} + \epsilon_s \epsilon_w \left(T_s^2 + T_{wi}^2\right)\left(T_s + T_{wi}\right)\right] \tag{80}$$

$$h_{env} = p \cdot r_{int} \cdot \left[Conv_{env} + \epsilon_{we}\left(T_{we}^2 + T_{env}^2\right)\left(T_{we} + T_{env}\right)\right] \tag{81}$$

Rate of combustion:

$$R_f = R_f' \cdot \frac{F_f \cdot \rho_g \cdot M_c}{F_g \cdot \rho_f} \tag{82}$$

Being:

$$R_f' = k_f \cdot d_o \cdot C_{O_2} \qquad\qquad \text{Rate of combustion of a single particle}$$

$$d_o = \frac{\dfrac{3D_O}{r_f^2 k_f}}{\dfrac{3D_O}{r_f^2 k_f} + 1} \qquad\qquad \text{Fraction of free oxygen available for reaction}$$

$$k_f = F_f \cdot exp\left(\frac{-E_f}{R_g T_g}\right) \qquad\qquad \text{Rate constant of combustion}$$

Rates of conversions:

$$R_{CaCO_3} = k_{CaCO_3} \cdot C_{CaCO_3} \tag{83}$$

$$R_{C2S} = k_{C2S} \cdot C_{CaO}^2 \cdot C_{SiO_2} \tag{84}$$

$$R_{C4AF} = k_{C4AF} \cdot C_{CaO}^4 \cdot C_{Al_2O_3} \cdot C_{Fe_2O_3} \tag{85}$$

$$R_{C3A} = k_{C3A} \cdot C_{CaO}^3 \cdot C_{Al_2O_3} \tag{86}$$

$$R_{C3S} = k_{C3S} \cdot C_{C2S} \cdot C_{CaO} \tag{87}$$

Being:

$$k_{CaCO_3} = F_{CaCO_3} \cdot exp\left(\frac{-E_{CaCO_3}}{R_g T_s}\right) \qquad \text{Rate constant of CaCO3 decomposition}$$

$$k_{C2S} = F_{C2S} \cdot exp\left(\frac{-E_{C2S}}{R_g T_s}\right) \qquad \text{Rate constant of C2S formation}$$

$$k_{C4AF} = F_{C4AF} \cdot exp\left(\frac{-E_{C4AF}}{R_g T_s}\right) \qquad \text{Rate constant of C4AF formation}$$

$$k_{C3A} = F_{C3A} \cdot exp\left(\frac{-E_{C3A}}{R_g T_s}\right) \qquad \text{Rate constant of C3A formation}$$

$$k_{C3S} = F_{C3S} \cdot exp\left(\frac{-E_{C3S}}{R_g T_s}\right) \qquad \text{Rate constant of C3S formation}$$

Heat sources:

$$Q_f = \Delta H_f \cdot R_f \cdot C_f \tag{88}$$

$$Q_c = \frac{M}{v_s} \cdot \left(\Delta h_{CaCO_3} \cdot R_{CaCO_3} + \Delta h_{C2S} \cdot R_{C2S} + \Delta h_{C4AF} \cdot R_{C4AF} + \Delta h_{C3A} \cdot R_{C3A} + \Delta h_{C3S} \cdot R_{C3S}\right) \tag{89}$$

98

Saeman equation:

$$\frac{\partial h}{\partial z} = \frac{3tan\theta \cdot M}{4\pi n\rho_s}[r^2 - (h-r)^2]^{-\frac{3}{2}} - \frac{tan\beta}{cos\theta} \tag{90}$$

Symbols:

T_g	Temperature freeboard gas
T_s	Temperature material bed
T_{wi}	Temperature internal wall
T_{we}	Temperature external wall
C_f	Fuel concentration
C_{CaCO3}	Mass fraction $CaCO_3$
C_{CaO}	Mass fraction CaO
C_{SiO2}	Mass fraction SiO_2
C_{Al2O3}	Mass fraction Al_2O_3
C_{Fe2O3}	Mass fraction Fe_2O_3
C_{C2S}	Mass fraction belite – $(CaO)_2 \cdot SiO_2$
C_{C4AF}	Mass fraction ferrite – $(CaO)_4 \cdot Al_2O_3 \cdot Fe_2O_3$
C_{C3A}	Mass fraction aluminate – $(CaO)_3 \cdot Al_2O_3$
C_{C3S}	Mass fraction alite – $(CaO)_3 \cdot SiO_2$
$A_{g,s,wi,we}$	Cross-sectional areas

$\rho_{g,s,w}$	Mass densities
$c_{g,s,w}$	Specific heat capacities
$v_{g,s}$	Velocities
F_i	Pre-exponential factors
E_i	Activation energies
Δ_{hi}	Enthalpies
$Conv_i$	Convective heat exchange coefficients
ε_i	Emissivities
M	Mass flow raw meal
R_g	Gas constant
σ	Stefan-Boltzmann constant
D_O	Diffusivity of oxygen
r_f	Radius of fuel particles
r_{int}	Kiln internal radius
r_{est}	Kiln external radius
T_{env}	Temperature environment
p	Filling angle
h	Bed depth

n	Kiln rotating speed
β	Kiln tilt angle
θ	Dynamic angle of response material

Appendix A.4 – GUI for the conventional rotary kiln

Installation

1. Get an Internet connection.
2. Extract "CementKilnSimulatorInstaller.zip"
3. Move to folder: "CementKilnSimulatorInstaller/"
4. Execute "CementKilnSimulator.exe" as Administrator.
5. Follow installation instructions.
6. When you asked, DON'T add shortcut to Desktop:
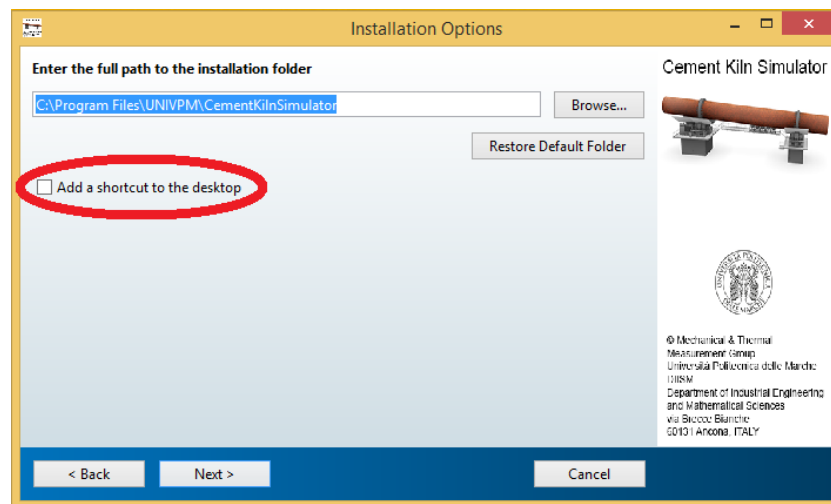
7. When installation is completed, move to installation folder e.g. "C:\Program Files\ UNIVPM\ CementKilnSimulator\"
8. Move to "application\" subfolder.
9. Create manually a shortcut to "CementKilnSimulator.exe" on Desktop.
10. Always run as Administrator from shortcut on Desktop.

Guide

1. First screen at the opening:
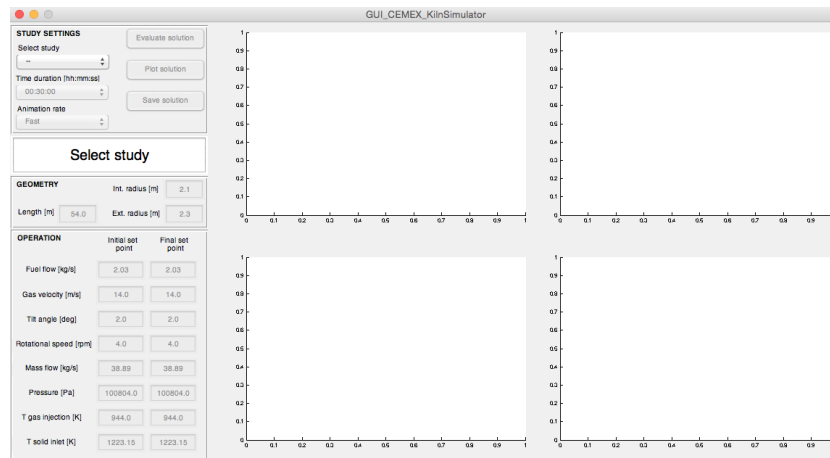
Five areas inside the GUI:

1. Study settings.
2. Prompt.
3. Inputs for geometry.
4. Inputs for operative parameters.
5. Area for plots.
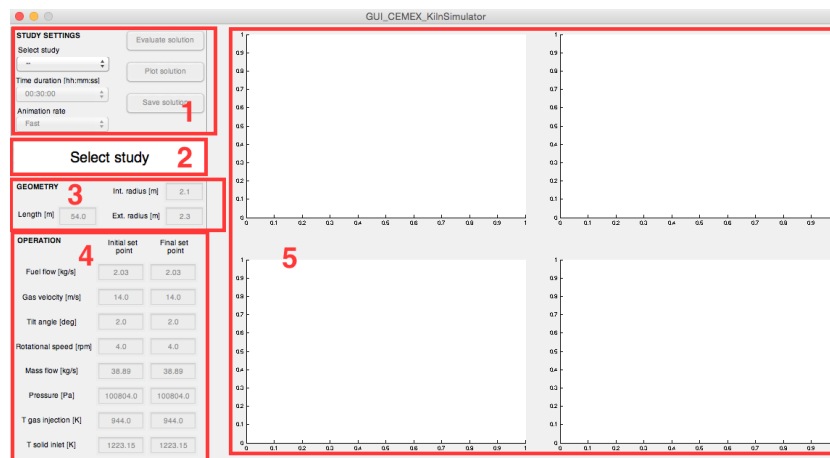
2. Choose between Stationary or Transient analysis:
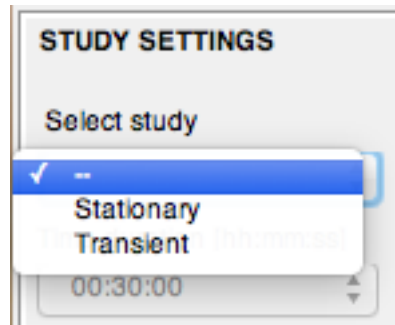
Stationary analysis calculates steady state response of the kiln for a set of operative parameters. Transient analysis calculates step response of the kiln for one or more changes of the operative parameters.

3. Stationary and Transient analysis:

Stationary analysis

User can specify kiln's length and radii. Values must be inserted in the correspondent boxes:
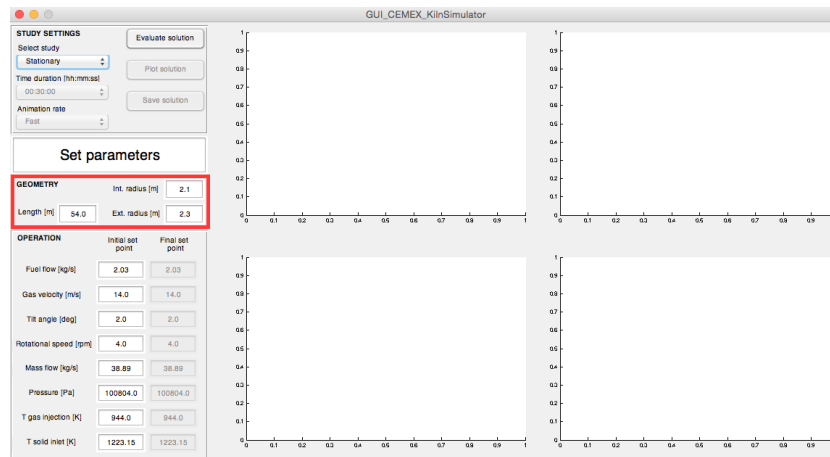
Operative parameters can be inserted in the "Initial set point" column. Every parameter must be expressed according to the units indicated in the GUI.
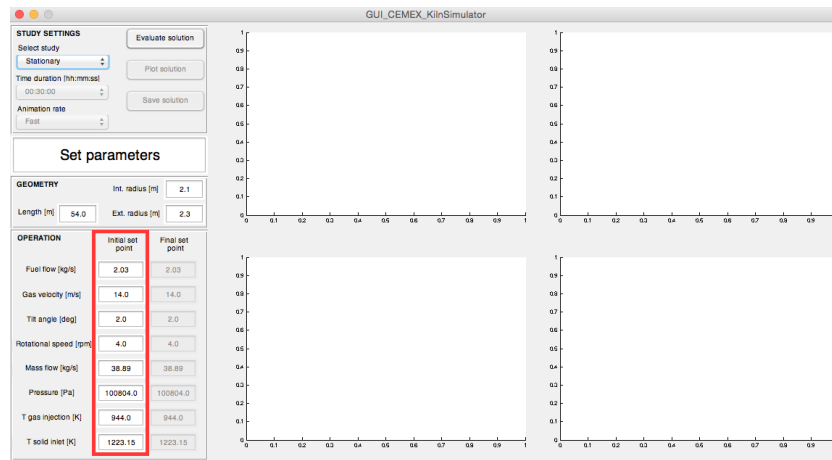
Transient analysis

Two different set points (Initial set point, Final set point) must be indicated:
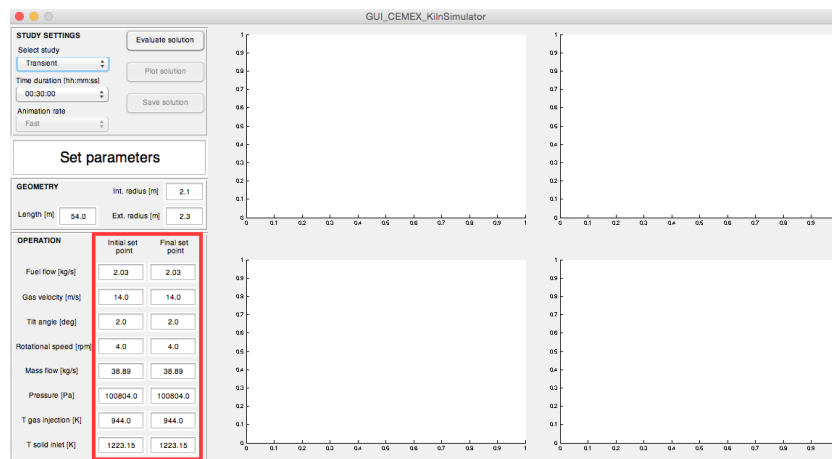
Also a "Time duration" must be choose:
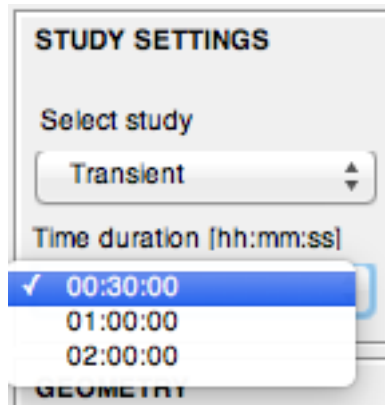
Transient analysis provides step response of the kiln between the two set points, for the specified "Time duration".

4. When simulations are completed, solutions can be plotted and/or saved:
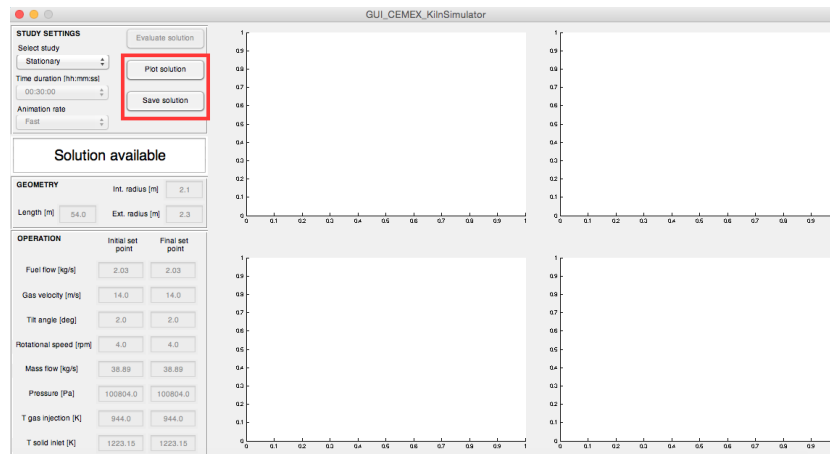
Plots represent temperature and chemical profiles along the kiln's length; for transient solution plots are animated, and they show evolution of profiles during time. Through "Animation rate" pushbutton user can specify velocity of animations:
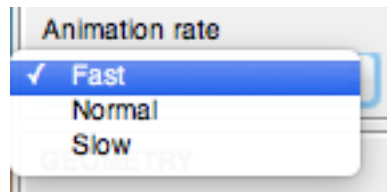
Stationary and Transient solutions are saved in .csv extension:

For Transient solution several spreadsheets are created, one for each time step of integration. More information about data format can be found inside spreadsheets.

Appendix A.5 – LEM model for the new DAPhNE module

Symbols:

T_s	Temperature material
T_w	Temperature wall
ρ_s	Mass density material
C_s	Specific heat material
A_s	Cross-sectional area material
v_s	Axial speed material
Q_C	Heat from chemical conversion
P_A	Absorbed power
h_{sw}	Heat exchange coeff. Material – wall
k	Thermal conductivity material
C_{CaCO3}	Mass fraction $CaCO_3$
C_{CaO}	Mass fraction CaO
R_{CaCO3}	Reaction rate
M_{CaCO3}	Molar mass $CaCO_3$
M_{CaO}	Molar mass CaO